A New Methodology for Sizing and Performance Predictions of a Rotary Wing Ejector

A Thesis

Presented to

The Academic Faculty

By

Alex Montfort Moodie

In Partial Fulfillment

of the Requirements for the Degree

Doctor of Philosophy

School of Aerospace Engineering

Georgia Institute of Technology

December 2008

A New Methodology for Sizing and Performance Predictions of a Rotary Wing Ejector

Approved By:

Dr. Daniel P. Schrage, Advisor
School of Aerospace Engineering
Georgia Institute of Technology

Dr. Stephen M. Ruffin
School of Aerospace Engineering
Georgia Institute of Technology

Dr. Lakshmi N. Sankar
School of Aerospace Engineering
Georgia Institute of Technology

Mark H. Waters
School of Aerospace Engineering
California Polytechnic State University

Dr. Richard J. Gaeta
Georgia Tech Research Institute
Georgia Institute of Technology

Date Approval: 10/02/2008

ACKNOWLEDGEMENTS

I would like to extend my thanks to the many individuals who have supported me through this endeavor. Dr. Daniel Schrage, my advisor, has provided me unwavering support and encouragement over the past four years. I am truly grateful for the opportunities he has given me and feel privileged to have worked under him at Georgia Tech. Special thanks to Dr. Lakshmi Sankar for bringing his considerable rotary wing aerodynamic experience to my reading committee. His generous support in lending his valuable insight towards this research and providing a much needed computational resource was invaluable. Thanks to Mark Waters for bringing extensive thermodynamic experience to my reading committee. His enthusiasm and support for this research has been inspiring. Thanks to Dr. Richard Gaeta for his continued encouragement, advice and support towards this research. Thanks to Dr. Stephen Ruffin for serving on my reading committee and providing valuable feedback for this research.

Georgia Tech has provided me with many positive experiences, contacts, and most importantly friends. I would like to thank Dr. Eric Johnson for opening this door and supporting me through my M.S. Special thanks go to Dr. Jimmy Tai for his advice, support, and encouragement through this journey. Thanks to Dr. Dimitri Mavris for graciously allowing me to use his facilities, especially access to his computer cluster. Dr. Ralph Latham provided me the high performance computing support that was critical to my research. Dr. Nicholas Alley provided sound advice and was a valuable resource for CFL3D and CFD. There is a long list of people at Georgia Tech who offered me support and friendship over the years and to mention them all would take up far too much room.

I would like to give special thanks to the former residents of Casa de Shalimar for all the good times.

My family and friends have given me their love and support through all of my endeavors. I would not be where I am without them. Mom, Paul, Dad, Libby, Dave, Tricia, Nate, and Colin…thanks.

Last but certainly not least, I would like to thank my wife, Annett, for being a constant beacon in my life, always giving encouragement, and making a home for us.

TABLE OF CONTENTS

LIST OF TABLES

LIST OF FIGURES

LIST OF SYMBOLS OR ABREVIATIONS

a	speed of sound
A	area
A_t	nozzle throat area
$\vec{B}$	body force vector
$\hat{\vec{B}}$	transformed body force vector
c	blade chord
c_p	constant pressure specific heat
c_v	constant volume specific heat
C_d, C_l, C_m	drag, lift, and moment coefficients
$C_{l\alpha}$	lift curve slope
C_P, C_T, C_W	power, thrust, and weight coefficients
cp	pressure coefficient
d	diameter
$d\vec{A}$	fluid element surface area
dD	blade element drag
dL	blade element lift
dr	blade element radial width
$d\vec{s}$	vortex filament width
$d\vec{v}$	change in induced velocity
D_{eq}	equivalent circular diameter

e	internal energy per unit mass
E	total energy per unit mass
f	friction factor
f_{me}	mixing effectiveness factor
f_P	Prandtl's tip loss exponent
F	induced velocity correction factor
$\vec{F}$	x-direction flux vector
$\vec{\hat{F}}$	ξ-direction flux vector
$\vec{\hat{F}}_v$	ξ-direction viscous flux vector
FN	nozzle net thrust
far	fuel-to-air ratio
g	gravity
$\vec{G}$	y-direction flux vector
$\vec{\hat{G}}$	η-direction flux vector
$\vec{\hat{G}}_v$	η-direction viscous flux vector
GW	vehicle gross weight
h	height
h_l	head loss
$\vec{H}$	z-direction flux vector
$\vec{\hat{H}}$	ζ-direction flux vector
$\vec{\hat{H}}_v$	ζ-direction viscous flux vector

J	transformation Jacobian
k	conduction coefficient; turbulent kinetic energy
l	length
LHV	fuel lower heating value
$\dot{m}$	mass flow rate
M	Mach number
$\vec{n}$	unit normal
N_b	number of blades
p	pressure
p_o	stagnation pressure
P	duct perimeter; mean pressure
$\Pr$	Prandtl number
$\Pr_T$	turbulent Prandtl number
$\dot{q}$	heat rate per unit mass
$\vec{Q}$	conservative flow variable vector
$\vec{\hat{Q}}$	transformed conservative flow vector
r	radial distance from center of rotation to blade element
r_d	duct bend radius
r_0	blade root cutout
$\vec{r}$	distance from vortex element to blade element
R	blade radius
R_{gas}	gas constant

Re	Reynolds number
S_{ref}	blade reference area
S_{seg}	blade segment area
t	time
T	temperature
T_o	stagnation temperature
$u, \quad v, \quad w$	Cartesian velocity components
$\vec{U}$	mean velocity vector
$U, \quad V, \quad W$	mean velocity components
$\vec{v}'$	fluctuating velocity vector
$\vec{V}$	velocity vector
$\overline{V}$	mean fluid velocity
$\vec{V}_D$	duct gas velocity
$\vec{V}_R, \quad \vec{V}_T, \quad \vec{V}_P$	radial, tangential, and perpendicular velocity vectors
α	angle of attack
$\beta_x, \quad \beta_y, \quad \beta_z$	heat flux vector components
δ_{ij}	Kronecker delta
ε	turbulent dissipation
ϕ	inflow angle
Φ	equivalence ratio
γ	ratio of specific heats

Γ	vortex filament strength
λ	inflow; coefficient of bulk viscosity
μ	coefficient of viscosity
μ_T	coefficient of turbulent viscosity
θ	pitch angle
θ_T	mean temperature
θ_T'	fluctuating temperature
ρ	air density
σ	rotor solidity; normal stress (xx, yy, zz subscripts)
τ	viscous stress tensor; shear stress (xy, yz, xz,… subscripts)
ω	turbulent vorticity magnitude
Ω	rotational speed; vorticity tensor
$\xi, \quad \eta, \quad \zeta$	chord-wise, span-wise, and normal body-fitted coordinates
ψ	azimuth angle
∞	free stream; ambient

SUMMARY

The application of an ejector nozzle integrated with a reaction drive rotor configuration for a vertical takeoff and landing rotorcraft is considered in this research. The ejector nozzle is a device that imparts energy from a high speed airflow source to a lower speed secondary airflow inside a duct. The overall nozzle exhaust mass flow rate is increased through fluid entrainment, while the exhaust gas velocity is simultaneously decreased. The exhaust gas velocity is strongly correlated to the jet noise produced by the nozzle, making the ejector a good candidate for propulsion system noise reduction. Ejector nozzles are mechanically simple in that there are no moving parts. However, coupled fluid dynamic processes are involved, complicating analysis and design.

Geometric definitions of the ejector nozzle are determined through a reduced fidelity, multi-disciplinary, representation of the rotary wing ejector. The resulting rotary wing ejector geometric sizing procedure relates standard vehicle and rotor design parameters to the ejector. Additionally, a rotary wing ejector performance procedure is developed to compare this rotor configuration to a conventional rotor. Performance characteristics and aerodynamic effects of the rotor and ejector nozzle are analytically studied. Ejector nozzle performance, in terms of exit velocities, is compared to the primary reaction drive nozzle; giving an indication of the potential for noise reduction.

Computational fluid dynamics are paramount in predicting the aerodynamic effects of the ejector nozzle located at the rotor blade tip. Two-dimensional, steady-state, Reynolds-averaged Navier-Stokes (RANS) models are implemented for sectional lift and drag predictions required for the rotor aerodynamic model associated with both the rotary wing ejector sizing and performance procedures. A three-dimensional, unsteady, RANS

simulation of the rotary wing ejector is performed to study the aerodynamic interactions between the ejector nozzle and rotor. Overall performance comparisons are made between the two- and three-dimensional models of the rotary wing ejector, and a similar conventional rotor.

CHAPTER 1

INTRODUCTION

Since the inception of the first practical rotorcraft in the early 20th century, there have been many variations explored to fulfill evolving requirements. The parallel development of turbine engines has proven invaluable to the evolution of rotorcraft. The increase in power supplied from the engine to the rotor while maintaining a high power to weight ratio has led to rotorcraft configurations that were previously impractical. While the pure helicopter has proven to be a versatile machine in many respects, it still has limitations. The most notable limitation is the maximum forward airspeed due to compressibility effects and retreating blade stall resulting in high blade and control loads and high vibration [Prouty, 1986; Leishman, 2000]. One solution to expand the main rotor limits is to compound the helicopter with a wing and auxiliary propulsion. The rotor can then be off-loaded and slowed, thus increasing the forward airspeed capabilities. Slowing the main rotor of a conventional transmission driven helicopter requires multiple gear stages within the transmission, thereby increasing the vehicle empty weight. A reaction drive rotor forgoes this problem by producing the required rotor torque with thrusters located at the blade tip. The rotor speed may be controlled either by varying the thrust generated by the tip thrusters or by allowing the rotor to autorotate.

The reaction drive helicopter has roots dating back to the first century A.D., when Hero of Alexandria constructed the first steam powered globe [Nichols, 1970]. This same concept has been built upon in the development of a helicopter rotor system where the torque to rotate the rotor blades is derived from a thrust source at the blade tip. There are two major types of reaction drive systems, the pure tip jet drive, where the engine is mounted at the blade tip, and the pressure jet drive, where the engine is fixed to the fuselage and the tip jet thrusters are a part of the propulsion exhaust [Stepan, 1958]. There have been many flight tested rotorcraft that have been powered by these systems starting with Friedrich von Doblhoff's WN-342 in 1945 [Nichols, 1970]. Although there have been many successful examples of this type of rotorcraft, there are currently none in production. One of the main drawbacks of the reaction drive rotor is the noise generated by the blade tip thruster due to the high gas velocities required to generate thrust. A proposed solution for this issue is the addition of an ejector nozzle to the reaction drive nozzle [Porter and Squyers, 1979].

An ejector nozzle is a fluid pump where a high-speed gas flow entrains a secondary flow into a mixing duct. The energy from the high-speed flow is transferred to the lower speed secondary flow. These devices are simplistic in the sense that there are no moving parts required. However, they involve coupled fluid dynamic processes that complicate analysis and design.

Ejector nozzles can be found for a wide variety of applications, spanning medical, industrial, and aerospace. There are three basic types of ejector nozzles: Jet pumps, blow-in door ejectors, and thrust augmenting ejectors. Jet pumps are used in many industrial processes, such as: refrigeration, evaporator-condenser heat exchangers, vacuum pumping, gas-vapor recovery, and transport of solids. The blow-in door ejector nozzle has been primarily employed on aircraft gas turbine engines as a noise reduction device. The thrust augmenting ejector has been exclusively developed for aerospace propulsion systems, primarily to increase the static thrust for vertical takeoff and landing (VTOL) and short takeoff and landing (STOL) applications.

The focus of this research is a reaction drive rotor with an integrated ejector nozzle. This description is quite cumbersome, and therefore the term "rotary wing ejector" is adopted as the descriptor with the intent of improving the readability of the document. The basic premise of applying this device to a reaction drive rotor is to increase the mass flow rate and decrease the exit velocity while maintaining the nozzle thrust. Therefore, the focus of this study is on the aerodynamic interactions between the reaction drive rotor and the ejector nozzle with the intent of establishing a basis for continued research towards predicting the noise generated by the rotary wing ejector system.

1.1 Motivation

A reaction drive, compound rotorcraft has been brought forward as a possible configuration to meet the performance requirements for the combat search and rescue (CSAR) mission. In addition to speed, range, and payload requirements, the acoustic signature of the vehicle is desired to be at least equivalent to a similarly sized helicopter. Historically, the noise generated by reaction drive rotorcraft has been dominated by the blade tip thruster exhaust. This characteristic has made them unattractive VTOL concepts, especially when operating in densely populated areas.

In order to estimate the noise generated by the blade tip thruster of the reaction drive rotor, the nozzle geometry and flow conditions are required. This mandates the development of a coupled thermodynamic engine cycle analysis and rotor aerodynamic analysis [Tai, 1998]. The ejector nozzle complicates this coupled analysis with more intricate geometry and fluid dynamic interactions. The motivation for this research is to develop an analytical method that predicts the aerodynamic characteristics of the rotary wing ejector operating in a hovering flight condition. The performance implications of this concept during hover are of interest. Additionally, the effect of the rotor on the ejector nozzle performance is also desired as it may affect the acoustic signature. While this study does not specifically address the acoustic effects of this ejector nozzle arrangement, the analytical methods developed in this research provide a foundation for further study, including an acoustic analysis of the rotary wing ejector.

1.1.1 Reaction Drive Compound Rotorcraft

A reaction drive rotorcraft is a class of VTOL aircraft that uses thrust generated at the blade tip to provide the torque required for powered flight. Compressed air is ducted from a compressor, powered by a piston or turbine engine, to the tip of the rotor blade, turned 90° and expanded through a nozzle to produce thrust. The compressed air source may be a shaft driven compressor, the fan discharge from a turbofan engine, or the exhaust efflux from a turbojet engine. The choice of how the air is supplied to the rotor is dependant on many factors, ranging from the vehicle mission to the type of material used to construct the rotor blades.

The reaction drive rotor system has several unique advantages when compared with conventional shaft driven rotors. There is no torque imparted on the airframe from the rotor and thus, no anti-torque device is required. This results in a reduction of the mechanical complexity and weight of the drive system. Further advantages can be achieved when the reaction drive rotor is incorporated on a compound rotorcraft. Examples of compound reaction drive rotorcraft are the McDonnell XV-1, shown in Figure 1, and the Fairey Rotodyne, shown in Figure 2. Dual use of the propulsion system to power the rotor in hover and produce the thrust in cruise is another advantage to this VTOL configuration. Additionally, in forward flight the rotor can autorotate at a slower RPM, allowing for higher cruise speeds. This was the case for both the McDonnell XV-1 and the Fairey Rotodyne.

Figure 1: McDonnell XV-1 Convertiplane

Figure 2: Fairey Rotodyne

Typically the reaction drive rotor system requires a larger hub than a conventional shaft driven rotor with increased complexity to accommodate the gas flow. The size of the hub depends on the cross sectional area required for the gas flow path. The gas flow path cross sectional area is subsequently linked to the pressure and flow speed of the gas, which are critical design variables. The increased size of the hub may result in drag penalties at the higher airspeeds, compared to a conventional hub. The solidity of the rotor will also have a direct impact on the operation of the reaction drive. In order to minimize pressure losses through the ducting, the velocity of the gas must be low. The consequence of low gas velocity is a larger duct area for the given mass flow rate. Since the gas is ducted through the blade, the chord has to accommodate both the blade structure and the duct; thereby driving the rotor solidity. The hovering Figure of Merit will begin to decrease as the solidity is increased due to the blade profile drag. Therefore, when the rotor is sized on a similar scale to a conventional shaft driven rotor, there is little volume available for the ducting in the rotor blades. The McDonnell XV-1 and the Fairey Rotodyne included a combustion chamber at the tip of each blade in an effort to maintain reasonable rotor solidity. Thermal energy is added to the airflow by burning fuel, thus reducing the mass flow requirements through the rotor blade. Using a combustion chamber at the blade tip loosens the coupling between the rotor and engine, allowing for more flexibility in the design.

Reaction drive rotors do not require anti-torque devices for power rotor flight conditions. However, additional means are required to achieve yaw control in hover and low speed flight when a vertical stabilizer is ineffective. When two engines are present, differential thrust or thrust vectoring may provide the necessary yaw control. If only one engine is available, additional yaw thrusters are required; thereby increasing the complexity of the vehicle system. The McDonnell XV-1 (Figure 1) had two yaw thrusters located at the trailing end of the tail booms. The Fairey Rotodyne had two turboprop engines, allowing each propeller to be feathered separately to produce differential thrust.

The thrust produced at the reaction drive nozzle is a function of the gas mass flow rate, the temperature of the gas, and the pressure ratio across the nozzle. Constraining the mass flow rate leads to the need for an increase in the nozzle pressure ratio or the inclusion of a tip combustion chamber to generate the thrust required by the reaction drive nozzle. The result is high velocity gas exhausting from the reaction drive nozzle. Since the sound power per unit volume is approximately proportional to the gas velocity to the eighth power [Lighthill, 1952], large gas velocities are very undesirable from an acoustic standpoint. The modification of the reaction drive nozzle to include an ejector nozzle has the potential to reduce the acoustic signature of the reaction drive rotor system by entraining free stream air with high speed exhaust gas, resulting in an increase in mass flow rate and a decrease in exhaust gas velocity for a given nozzle thrust.

1.2 Objective

The objective of this research is to determine the aerodynamic effects on an ejector nozzle integrated with a reaction drive rotor in a hovering flight condition. Therefore, to meet this objective the scope of this research will cover the following four areas:

1. The development of an analytical method to determine ejector geometry and predict flow conditions for a given sizing condition.

2. The development of an analytical method to predict performance characteristics for the sized rotary wing ejector over a range of hovering rotor thrust conditions.
3. The development of an ejector nozzle thrust balancing procedure to match the nozzle thrust required to the nozzle thrust available for a three-dimensional model of the rotary wing ejector.
4. Study the three-dimensional aerodynamic effects caused by the presence of the ejector nozzle on the rotor performance in hover.

The unique application of an ejector nozzle integrated with a reaction drive rotor has not been studied to date, and the basic aerodynamic ramifications are not well understood. Therefore, the focus of this research concerns only the aerodynamic interactions between the reaction drive rotor and the ejector nozzle. Furthermore, the test case for this proposed research is a rigid hovering rotor, thereby neglecting any dynamic and aeroelastic effects the ejector nozzle imparts on the rotor blade.

CHAPTER 2

LITERATURE REVIEW

Reaction drive rotors and ejector nozzles have been widely studied independently over the last half century. To date there is not one production rotorcraft employing a reaction drive rotor, primarily due to their lower efficiency and higher noise signature compared to a shaft driven rotor. Many of the technical challenges faced by these rotorcraft concepts were overcome through a variety of prototype development programs, the most successful being the Fairey Rotodyne, shown in Figure 2. Ejector nozzles developed for flight vehicles have followed a similar path, leading to their integration with propulsion systems and several prototype V/STOL technology demonstrators.

2.1 Reaction Drive Rotors

There have been several configurations of reaction drive rotors investigated to date. Each configuration is defined by the way in which thrust is produced at the blade tip. Aspirated reaction drive rotors constitute the majority of this type of rotorcraft prototype developed to date. The energy used to generate the thrust at the blade tip is typically derived from a gas turbine or piston driven compressor. The consequence is a coupling between the engine and rotor; where the ducting and nozzle within the rotor can be considered an additional turbine. Therefore, the background survey concerning reaction drive rotors for this research is focused on the coupling between the engine-rotor thermodynamics and rotor aerodynamics. Additionally, the noise generated by the tip thruster exhaust is investigated as it is a central issue for this rotor configuration.

Early analytical studies showed a direct coupling between the engine and rotor of a reaction drive rotor configuration. The thrust produced by the blade tip thruster, in terms of the mass flow rate and gas velocity, was used to relate to the rotor performance. This was achieved through the effects of the thruster jet exhaust on the rotor aerodynamics [Fiorini, 1961; Evans and McCloud, 1965]. The power available calculation for a reaction drive rotor requires knowledge of the flow conditions beginning at the engine extraction point. Next, the flow conditions, including duct losses, between the engine and rotor hub are calculated. Then, the flow conditions through the blade, including duct losses and centrifugal pumping effects are determined. Finally the tip thruster nozzle flow conditions are calculated, resulting in the thrust produced by the nozzle. The nozzle thrust multiplied by the blade radius and rotor rotational speed gives the power available [Bachmann, 1970]. For reaction drive rotors that derive the gas directly from a turbine engine, a cycle analysis must be included to balance the power available with the power required [Crossley and Rutherford, 1995; Tai, 1998].

A major drawback to reaction drive rotors compared to conventional helicopter rotors, other than lower overall efficiency [Nichols, 1970], is the noise generated by the high speed gas exhausting from the blade tip nozzle. There is limited acoustic data available for prototype reaction drive vehicles. Take off acoustic data for the Hughes XV-9A Hot Cycle and Fairey Rotodyne is compared with the Sikorsky S-61 in Figure 3 [Harned *et al*., 1967]. The reaction drive rotor concepts generate significantly more noise over the same distance, considering their gross weight. The Hughes XV-9A generates approximately the same noise as the Sikorsky S-61, but is nearly half the gross weight.

The Fairey Rotodyne generates significantly more noise, especially considering the additional distance to the microphone.

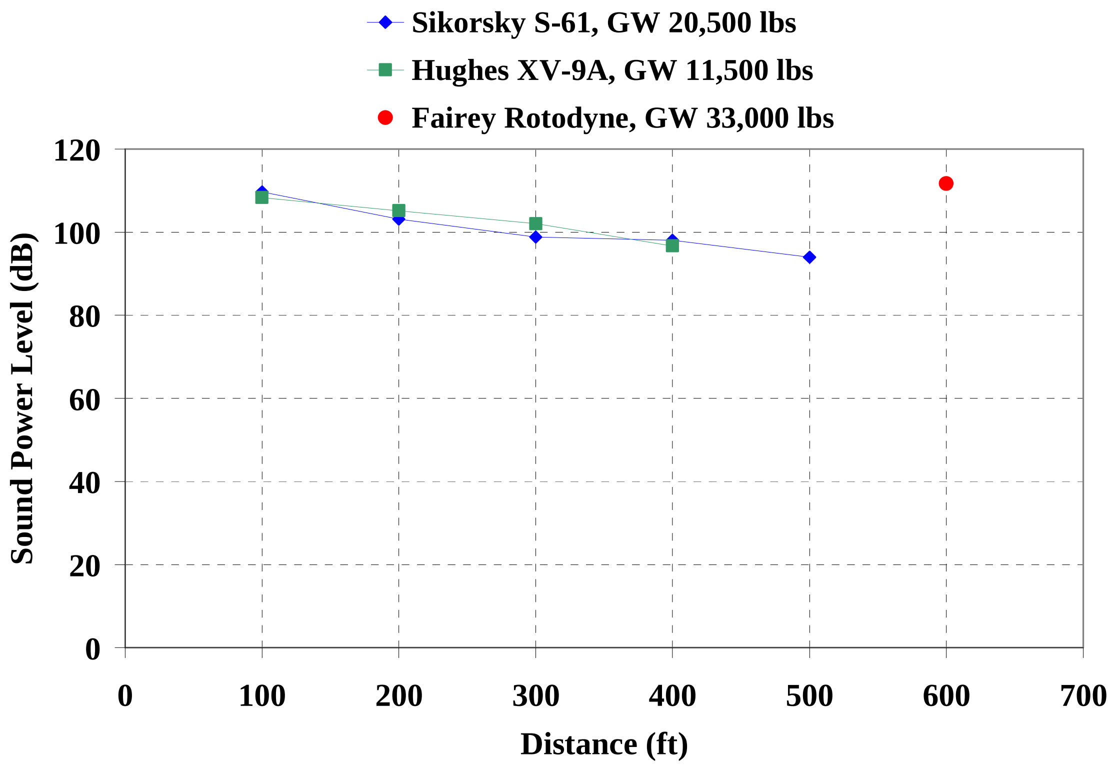

Figure 3: Rotorcraft Noise Comparison

2.2 Ejector Theory

The ejector has many applications ranging across industrial, medical, and aerospace. The result is thousands of publications on theoretical, analytical, and experimental investigations that concern everything from the fundamental fluid mechanisms to prototype flight vehicles. The focus of this research is concerned with an aeronautical application of an ejector in low altitude, subsonic-transonic flow regimes. Therefore, the literature review will only consider air-to-air ejectors applied to flight vehicles.

One of the first publications of an ejector nozzle for thrust augmentation of a aircraft propulsion system was by von Karman (1930). This theoretical investigation laid the ground work for the many different applications of the air-to-air ejector in aeronautical research. In 1979, Porter and Squyers compiled over 1,600 references of theoretical, analytical, and experimental works with ejectors up until their present day. This review of the state of ejector technology was followed by Sun and Eames (1995). Their review focused on the variety of ejector applications in industrial processes, with a note on thrust augmenting ejector nozzles for V/STOL aircraft research. Subsequent publications can be found up to the present for a variety of ejector applications.

The ejector is a fluid dynamic device that requires no moving parts. However, the fluid mechanisms involved are quite complicated. The ejector may be separated into four flow elements and three geometric components: the primary and secondary flows, mixing regime, and ejector exhaust mixed flow. The primary flow is typically supersonic and derived from a compressed air source, such as a turbine engine. The secondary flow can either be static, subsonic, sonic, or supersonic; depending on the application. This flow is ducted from the surroundings into the ejector and interacts with the primary flow at the beginning of the mixing regime. The primary and secondary flows are then mixed either unaided by the turbulent shear layer or forced by a flow mixing device. The mixed flow is finally exhausted from the ejector to the surroundings.

The three geometric components of the ejector consist of a primary nozzle, secondary inlets, and ejector shroud. The primary nozzle may either be a convergent or convergent-divergent nozzle configuration depending on the intended application. The secondary inlets may be either diffusers or nozzles; depending on the desired flow velocity at the beginning of the mixing regime. The ejector shroud may have any shape required by the designer. For aircraft applications where the ejector is protruding into the free stream, streamlining the outside portion of the shroud is typically done to reduce drag. The internal shape of the shroud, its flow path area, and its length are dependant on the primary and secondary flow conditions [De Chant, 1998]. This dependency increases the difficulty in the design of an ejector nozzle for a given application. A basic ejector schematic of an ejector is shown in Figure 4.

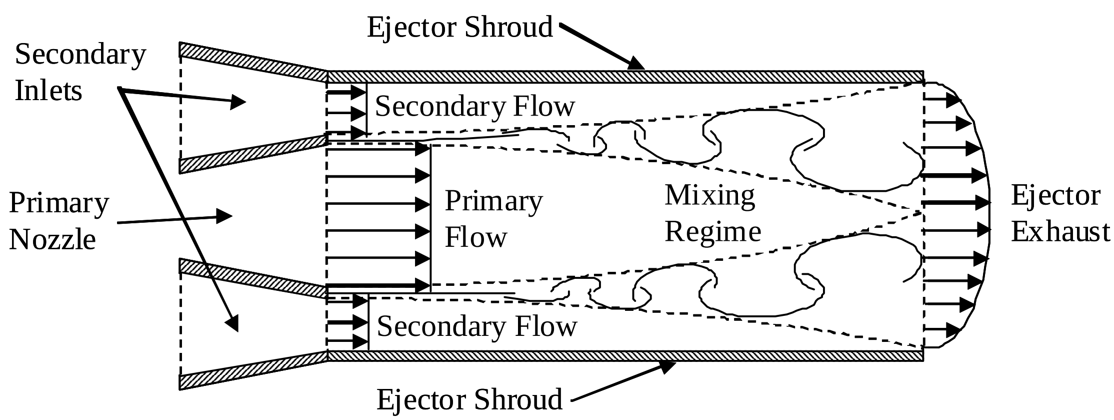

Figure 4: Ejector System Schematic

Mixing of the two air streams is a key mechanism in the operation of an ejector. The shear layer that develops between the primary and secondary flows has been studied extensively. The most notable works relevant to the ejector problem are in the area of turbulent shear layers. Early studies on shear layer characteristics found that as the speed of the secondary flow increases, the periodicity of the turbulent shear layer reduces and then vanishes when the secondary stream is supersonic [Pai, 1952]. Experimental and analytical studies of the turbulent shear layer showed that compressibility effects on the growth of the turbulent shear layer cannot be neglected [Bogdanoff, 1982; Papamoschou and Roshko, 1988; Elliot and Semimy, 1990; Goebel and Dutton, 1991]. These studies were expanded to rectangular free and coaxial supersonic jets, showing an increase in the growth rate of the shear layer compared to a circular free jet [Gutmark *et al*., 1991]. The experimental studies outline the complexity of the fluid mechanisms that dominate the mixing of two co-flowing air streams; especially when one or both are supersonic. A simplified view of turbulent mixing can be taken as the convection by the mean velocity field and large-scaled turbulent motions, and gradient-type turbulent diffusion by small-scale turbulent motions [Patterson, 1984].

The fluid mechanics of the ejector nozzle have been studied analytically, numerically, and experimentally. Some of these studies include full scale prototype aircraft employing ejectors as a part of the propulsion system for thrust augmentation or noise suppression, lift augmentation, and exhaust infrared suppression.

2.2.1 Analytical Studies

Early analytical studies of the ejector were based on one-dimensional (1D) control volume theory. These models were typically empirically corrected based on experimental data [De Chant, 1998]. Some early examples of 1D control volume studies assumed the flow is fully mixed at the control volume exit. Overall ejector performance, such as thrust, mean velocity, pressure, and temperature, can be determined using this approach [Keenan *et al*., 1950; Fabri and Paulon, 1958; Addy *et al*., 1981; Emanuel, 1976; Quinn, 1973; Dutton and Carroll, 1986; Presz and Gousy, 1986; Presz and Blinn, 1987; Alperin and Wu, 1983a and 1983b; Arbel *et al*., 2003]. This type of model is well suited for early design stages when the details of the fluid mechanics are less important than a simple model that can be used during design optimization [Kremar *et al*., 2003]. The two primary disadvantages when using this method are the use of the fully mixed flow assumption and neglecting the shroud geometry. This method does not take into account the compressibility effect on the shear layer growth, the length of the mixing duct required for full mixing, and the shape of the ejector shroud. Therefore, the model will not perform consistently across all variations of ejector designs.

An interesting approach to the ejector problem using a vortex lattice method was implemented to account for the external flow surrounding an ejector wing. This method is able to capture the geometric effects, primarily the length and position of the shroud, on ejector performance [Bevilaqua, 1978 and 1984; Woolard, 1975; Alperin and Wu, 1981]. These are the first analytical models that include the flow field in which the ejector operates. The following analogy is made based on these studies [Bevilaqua 1978]:

"*The ejector shroud is considered to be "flying" in the secondary velocity field induced by the entrainment of the primary jet, so that the augmenting thrust is viewed as being analogous to the lift on an airfoil.*"

While this method takes into consideration the operating flow field, the turbulent mixing process is modeled as particle collisions. Therefore, this type of model is incapable of capturing compressibility effects without empirical data. In addition, by assuming the particle collision analogy for the mixing process, the thickness of the primary jet is neglected and the stream-wise jet velocity decay must be empirically predicted. Therefore, the mixing of the primary and secondary flows is not impacted by the presence of vortices representing the ejector shrouds. While this novel approach may be useful in predicting the overall performance of an ejector, numerical methods are required to achieve more realistic models of the turbulent mixing process inside the ejector.

2.2.2 Numerical Studies

Early numerical models employed two-dimensional (2D) inviscid or boundary layer formulations. Many of these studies associated with technology development programs and were accompanied by an experiment for model validation. These methods are able to predict the length of the mixing section, but require the primary air flow to be supersonic. This analysis method is considered to be a higher fidelity model of the ejector fluid mechanics than that of the 1D control volume or vortex lattice methods. The compressibility effects are adequately captured and the specified shroud geometry can be modeled [Chow and Addy, 1964; Gilbert and Hill, 1973; Hickman *et al*., 1970 and 1972; Maroti *et al*., 1976; Hedges and Hill, 1974; DeJoode and Patankar, 1978; Yang *et al*., 1985; Clark, 1995; Papamoschou, 1996; Han and Peddieson, 2002]. The focus of these studies was on the flow inside the ejector, and any external flow characteristics were neglected. Many of these early numerical formulations accompanied laboratory experiments and the results showed good correlation.

A unique study implementing numerical and analytical perturbation solutions computed for the Navier-Stokes equations was performed for a mixer/ejector nozzle. This provided a model of intermediate complexity between the control volume method and the inviscid/boundary layer methods. This method relied on a priori knowledge of the flow structure inside the shroud based on uniform inlet conditions [De Chant, 1998].

This information may be difficult to obtain for some configurations; however, it may be a good compromise in model fidelity for aircraft engine applications.

In the last two and a half decades, ejector models have been primarily developed using the computational fluid dynamics (CFD) in the form of the Navier-Stokes relations. Two-dimensional CFD models developed over this time typically only consider the internal flow field of the ejector, with the primary focus on either reducing engine noise or exhaust temperature, depending on the aircraft mission [McFarlan *et al*., 1990; Barber and Anderson, 1991 and 1992; DeBonis, 1992; Elliott *et al*., 1992; Dong and Mankbadi, 1999]. The effects on the ejector performance and efficiency have been shown to be dependant on the shock train formed within the mixing duct [Desevaux and Lanzetta, 2004]. Two-dimensional CFD formulations of ejector flows have shown good agreement with the accompanying experimental data in terms of predicting the internal flow structure, and pressure, temperature, and velocity distributions.

Three-dimensional (3D) CFD studies considering the internal flow of ejectors were performed by numerous investigators for a range of applications. Three-dimensional CFD modeling has been used to analyze engine mixer/ejector nozzle configurations for noise reduction with the primary goal to develop a design tool that integrated the CFD analysis to CAD and manufacturing. However, poor correlation of the CFD results to experimental data at the time hindered progress for this approach [Kuhne *et al*., 1994].

An ejector system used for nacelle ventilation on the BA-609 Tiltrotor Aircraft was designed primarily using CFD models. In addition to the modeling, an experiment was conducted to test four of the design configurations in order to validate the model [Loka *et al*., 2000]. A study of a thrust augmentation mixer/ejector for commercial aircraft engines was performed by Presz *et al*, 2002, provided a static thrust gain and sideline noise reduction. In this study, a control volume analysis was used to generate the ideal mixer/ejector performance, and a 3D CFD model was then developed and compared to the ideal case over a range of airspeeds. The CFD results predicted much higher thrust gains compared to the control volume model at higher airspeeds. Scaled experimental tests were performed in order to validate the modeling. These tests showed good correlation between the control volume model and CFD at the lower airspeeds, but poor correlation with the CFD modeling at the higher airspeeds. The study went further to include static engine thrust tests with and without the mixer/ejector and flight testing of the mixer/ejector installed on a Gulfstream GII, shown in Figure 5. Both the full scale static thrust test and the flight test showed excellent agreement with the CFD model results [Presz *et al*., 2002].

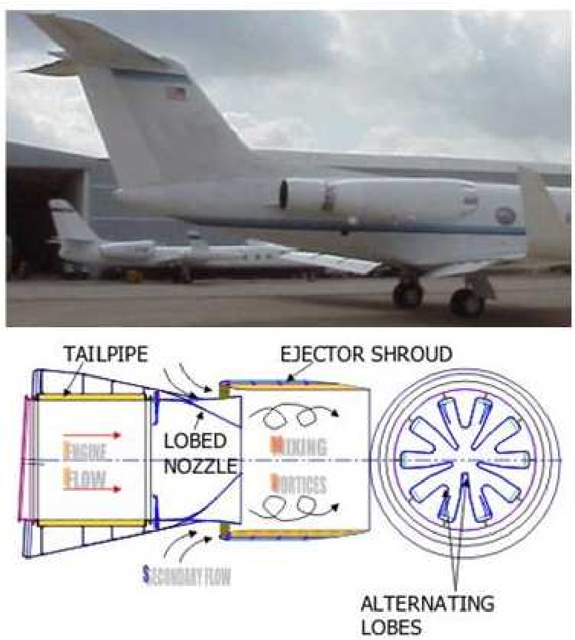

Figure 5: Propulsion System Noise Suppression Mixer/Ejector

A large effort in the implementation of mixer/ejector nozzles has been undertaken for the high speed civil transport program (HSCT). Studies performed under the HSCT program focused on the rapid mixing of the primary and secondary flows with forced mixing nozzles. The CFD modeling of these mixer/ejector nozzles prescribed two counter rotating vortex pairs along the exit contour of a lobed mixing nozzle in order to simulate mixing enhancement tabs. The result of these studies showed only a small increase in the overall mixing of the two air streams when vortex-generating tabs were used in conjunction with a lobed mixing nozzle [DalBello and Steffen, 2002; Yoder *et al*., 2005]. The impact of the sidewall of a lobed mixer nozzle has been studied, resulting in the validation of the half-chute symmetry assumption for the central regions of the lobed mixer nozzle. However, this assumption gave poor correlation of a computational model to experimental data at the sidewall regions [Yoder *et al*., 2005].

A variety of turbulence models have been applied to numerical studies of ejector flows. Early works analyzing ejector flow with CFD used the Baldwin-Lomax algebraic model [McFarlan and McMurry, 1990]. The k-Epsilon turbulence model has been widely used for both 2D and 3D ejector flows [DeBonis, 1992; Kuhne *et al*., 1994; Presz *et al*., 2002; Dalbello and Steffen, 2002; Desevaux and Lanzetta, 2004; Yoder *et al*., 2005; Gullia *et al*., 2006; Masud and Javed, 2007; Yoder *et al*., 2005]. Large eddy simulation (LES) has been successfully applied to ejector flows, most notably when including a lobed, forced mixing, primary nozzle [Dong and Mankbadi, 1999]. The k-Omega turbulence model applied to a 3D CFD model showed good agreement for predicting the internal ejector flow field for a rectangular primary nozzle [Loka *et al*., 2000]. Menter's k-Omega shear stress transport (SST) turbulence model applied to a circular primary nozzle of an ejector showed better overall agreement with experimental results compared with several other models [Balasubramanyam *et al*., 2005].

The majority of the numerical studies were related to propulsion systems, and therefore, the assumption that the secondary flow inlet conditions are uniform is justified. This assumption may not be valid for predicting ejector performance when the device is located on the trailing edge of a wing, as in the example of the ejector wing concept [Bevilaqua, 1978].

2.2.3 Experimental Studies

Early experiments with ejectors performed in the mid 20th century were conducted primarily to show correlation with the analytical 1D control volume models used at the time. During this time there was great interest in ejector technology applied to aircraft propulsion [Keenan *et al*., 1950; Fabri and Paulon, 1958]. The primary rational for using the control volume method was to provide a model that can be used parametrically or in an optimization procedure [Dutton *et al*., 1982]. Experimentation was then used to make comparisons against the model, resulting in empirical correction factors to provide the necessary accuracy for ejector design.

Later experimentation was performed in order to validate numerical techniques for solving the 2D inviscid or boundary layer formulations. This approach provided good agreement between the model and experimental data for the ejector problem [Hickman *et al*., 1970 and 1972; Gilbert and Hill, 1973; Hedges and Hill, 1974; and Maroti, 1976]. These experimental works were performed in a laboratory setting and only concerned the study of the internal fluid mechanics of the high and low speed flow interactions.

Wind tunnel investigations of an ejector blown lift/cruise flap have produced a 30% increase in thrust at static conditions over a traditional nozzle. However, the thrust augmentation fell of rapidly as the free stream speed increased, resulting in a thrust penalty at cruise speeds. It was determined that the flow was not fully mixed at the exit of the ejector and this may decrease the performance at higher speeds [Clark, 1973]. There has been a significant experimental effort to employ mixer/ejector nozzles on turbofan engines to reduce noise. Experimental investigations of the flow within model turbofan forced-mixer nozzles have been performed in order to obtain velocity and thermodynamic state properties. The data obtained were used to further develop computational models of forced-mixer nozzles [Paterson, 1984]. These experimental works have shown the effect of the stream-wise vorticity generated by the lobed mixer nozzle on the mixing of the engine core flow and bypass fan flow [Presz and Gousy, 1986; Skebe *et al*., 1998]. The result of this experimental effort is a set of benchmark data that could be used to aid CFD modeling of this complex flow field [Tillman *et al*. 1988]. Further investigation of mixing enhancement as a possible technique of increasing the growth rate of the shear layer between two co-flowing gas streams using vortex generators to introduce stream-wise vorticity directly into the shear layer. This technique was successful at increasing the shear layer growth rate [Dolling *et al*., 1992; Fernando and Menon, 1993].

Experimental studies in the shear layer growth mechanism between two co-flowing gas streams have been shown to be paramount in the understanding of the fluid mechanics of ejectors. The effect of compressibility reducing the growth of the shear layer was uncovered during these experiments [Gutmark *et al*., 1991]. Other notable studies were performed where the ejector pumping characteristics were shown to be dependant on the shape of the shroud [Luffy and Hamed, 1992]. In addition, the rectangular mixer/ejector nozzles were shown to have similar characteristics to the circular mixer/ejector nozzles previously studied [Tillman *et al*., 1988; Charyulu *et al*., 1998]. A more recent study showed that multi-stage mixer/ejector systems are able to further increase diffusion rate and thrust augmentation [Presz and Werle, 2002].

There were several experimental studies performed that included the flow field the ejector is operating within. One study employed an ejector nozzle embedded in a wing section and was tested in a wind tunnel. The results showed that when the ejector was operating, the stagnation point move aft along the lower surface, thereby increasing the effective angle of attack [Catalano *et al*., 1982]. This test shows the need for the inclusion of the operating flow field when modeling this type of ejector/wing configuration. Another wind tunnel test on a STOVL fighter aircraft concept showed that thrust augmenting ejector systems were viable for this application [Poppen *et al*., 1991; Smith *et al*., 1992; Naumowicz and Smith, 1992].

2.2.4 Ejector Aeroacoustics

The motivation for many applications of the air-to-air ejector is the reduction of noise generated by a high speed exhaust flow. The sound power of a jet of air into a quiescent atmosphere was shown to be approximately proportional to the jet velocity to the eighth power [Lighthill, 1952]. Thus, by entraining lower velocity airflow, the exit gas velocity of the ejector is reduced through fluid mixing either by the turbulent shear layer growth or forced mixing. The result is an overall lower sound power level compared to the original jet source. Lighthill's analogy has been applied to an ejector nozzle, which include both theoretical and experimental development. The experimental results showed additional noise sources, including shock noise, propagating past the efflux of the ejector [Middleton, 1970]. Much of the development of the mixer/ejector nozzle for the purpose of noise reduction has been undertaken during the various supersonic transport (SST) programs. The development of the supersonic transport propulsion system showed early on that noise was a critical issue for the success of this program. The rule of thumb used to determine the success of a noise suppression concept is whether better than 1 decibel in perceived noise level (PNdB) per 1% thrust loss is achieved [Smith *et al*, 1988]. Test results showed the ejector shroud primarily reduced the high frequency noise sources and it was recognized that applying an acoustic treatment to the shroud walls would further reduce the ejector internal mixing noise. Convergent-divergent mixer nozzles showed lower noise levels compared the convergent type and increasing the secondary ejector area without increasing the ejector length resulted in higher noise levels [Krejsa *et al*, 1990]. Further experimental studies, some including CFD modeling, were performed to determine the noise of the mixer ejector nozzle. However, the CFD models were only used to predict the ejector flow properties, not the noise. The flow properties were then used in semi-empirical acoustic prediction models to determine the noise generated by the ejector [Lord *et al*., 1990]. Another approach taken was to consider a range of engine designs, including baseline noise levels, to determine the appropriate noise suppression method to achieve optimum configurations based on semi-quantitative analysis. Acoustically treated two-dimensional mixer ejectors concept showed the most success out of the configurations that were examined, shown in Figure 6 [Thayer *et al*, 2004]. The main design tradeoffs with this mixer ejector configuration are a reduction in takeoff thrust coefficient, increased complexity, weight, and cost associated with the ejector doors and required acoustic treatment against the increased weight and drag penalty with a larger size engine to achieve the same noise levels without the mixer ejector nozzle [Stone *et al*, 2000]. The noise sources shown to have the most influential contributions are the jet noise, mixing noise, and shock noise. A semi-empirical computational methodology for two-dimensional mixer ejector nozzle systems for the HSCT based on principal aerodynamic and geometric variables was developed to predict noise levels [Stone *et al*, 2003].

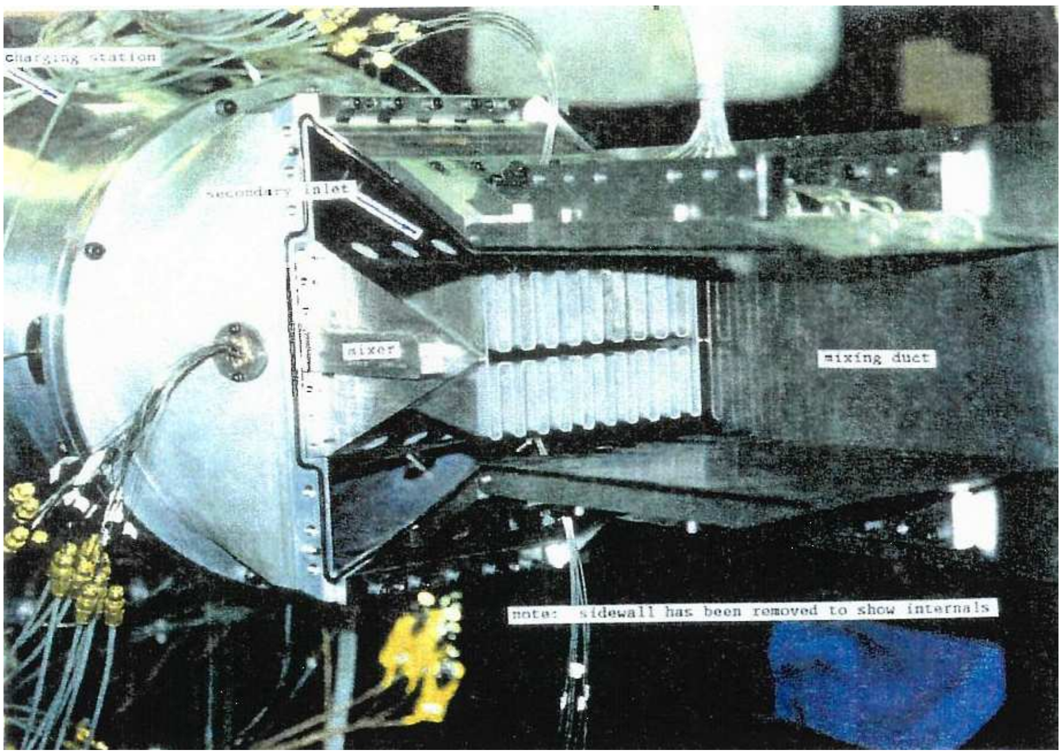

Figure 6: HSCT Two Dimensional Mixer Ejector Nozzle

2.2.5 Aircraft Applications

Many aircraft concepts have been explored that have used ejector systems for thrust augmentation, however, very few have been employed on prototype aircraft. The aircraft prototypes using thrust augmenting ejectors include the Lockheed Hummingbird XV-4A, DeHavilland Buffalo XC-8A, Rockwell International XFV-12A, and Ball-Bartoe JW-1 Augmenter Wing.

The XV-4A, a research aircraft, shown in Figure 7, was developed to test the feasibility of the ejector for VTOL. This aircraft had limited success, only achieving a thrust augmentation ratio of 1.3. The low thrust augmentation ratio along with exhaust re-ingestion and suck down effect due to the ground vortex generated by the high speed exhaust plume resulted in marginal vertical lift capability. The program was canceled because this concept was not competitive with other VTOL aircraft at the time [Porter and Squyers, 1979].

Figure 7: Lockheed XV-4A Hummingbird Hover Test

NASA, working with the Canadian Department of Industry, Trade, and Commerce (DITC), DeHavilland, and Boeing, modified a C-8A Buffalo for STOL capability using an ejector-flap augmenter wing system, shown in Figure 8. This aircraft was the first successful STOL transport demonstrator. The flight envelope was sufficiently explored, resulting in an extended flight test program primarily focused on handling qualities and noise abatement [Porter and Squyers, 1979].

Figure 8: NASA/DITC XC-8A STOL Research Aircraft

The Ball-Bartoe Jet Wing aircraft, pictured in Figure 9, was developed by Ball-Bartoe, in partnership with the University of Tennessee under the Naval Air Systems Command. This aircraft demonstrated a minimum control speed of 35 knots with an estimated static thrust augmentation of 1.17. Since this aircraft is privately owned, there is very little published information [Porter and Squyers, 1979].

Figure 9: Ball-Bartoe JW-1 STOL Research Aircraft

In recent years, the ejector has been primarily employed as an engine noise or exhaust infrared suppression device for propulsion systems. Figure 5 is an example of a noise suppressor installed on a business jet [Presz and Werle, 2002]. The infrared suppression system on the RAH-66 Comanche, shown in Figure 10, used ejector technology to cool the engine exhaust [Presz and Werle, 2002].

Figure 10: RAH-66 Comanche Mixer/Ejector Exhaust Infrared Suppressor System

2.3 Conclusion

The aspirated reaction drive rotor has been shown to be a coupled system, requiring multi-disciplinary analysis. Due to the length of the duct inside the rotor blade, the effects of centrifugal pumping on the internal flow cannot be neglected. When considering a turbojet or turbofan engine, the reaction drive is considered an additional turbine and requires a coupled, multi-disciplinary procedure for analysis. The limited acoustic data available confirms that reaction drive rotor configurations are noisier than conventional rotorcraft.

The ejector has been extensively studied over the last half century. This has lead to a diversity of applications where the ejector is an integral system component. In regards to aerospace applications, the mixer/ejector nozzle has been primarily associated with the propulsion system. The benefits of adding this component to an aircraft's propulsion system are typically thrust augmentation, noise suppression, or exhaust infrared suppression. The majority of the analytical and numerical work towards calculating ejector performance has been limited to analyzing the internal fluid mechanics. While this may be a valid approach for many applications, there are some cases where the model predictions and test results do not correlate. This is especially true for aircraft with ejector augmented jet wings. As a result, the complete internal and external flow field must be modeled to capture the physics of the problem. Aside from the mention of the ejector nozzle having a potential application to a reaction drive rotor by Porter and Squyers (1979), no published information could be found that studied the application of an ejector nozzle to a reaction drive rotor configuration. This is a unique application of an ejector nozzle and the basic aerodynamic characteristics are not well understood. Therefore, the focus of this study is on the aerodynamic interactions between the reaction drive rotor and the ejector nozzle with the intent of establishing a basis for continued research towards predicting the noise generated by the rotary wing ejector system.

CHAPTER 3

MATHMATICAL AND NUMERICAL FORMULATION

The analytical assessment of the rotary wing ejector considered for this study may be accomplished through several different approaches. The analytical method presented contains a lower fidelity vortex wake formulation to predict rotor aerodynamics in hover. A one-dimensional thermodynamic control volume approach is implemented to predict both the reaction drive and ejector nozzle flow properties. Two-dimensional computational fluid dynamic simulations are used to estimate the aerodynamic loads at the blade tip region, where the tip jet ejector nozzle is located. Finally, a three-dimensional computational fluid dynamic model of the rotor and tip jet ejector nozzle is developed to predict the rotor and ejector aerodynamic characteristics.

3.1 Rotor Aerodynamics

There are many different approaches to predicting the performance of a helicopter rotor presently available to the engineer. The different methods range across classical actuator disks, blade element including uniform inflow, non-uniform inflow, dynamic inflow, and vortex wake methods, hybrid CFD-vortex wake methods, and CFD. Selecting the approach has a direct effect on computational time and solution accuracy. This tradeoff must be carefully considered for the application at hand. For example, the prediction of the download characteristics on a tilt-rotor aircraft with flaps and leading edge slats would require the use of a higher fidelity CFD approach. On the opposite end of the spectrum, trading rotor configurations (single, tandem, coaxial, or side-by-side) during a conceptual design requires a simple, low fidelity approach, such as an actuator disk, that can rapidly provide solutions. The nature of the problem examined in this research almost dictates the use of CFD exclusively. However, lacking guidance for the basic characteristics of this rotor configuration, a geometric sizing procedure must preclude any CFD rotor modeling approaches. With this in mind, a simple rotor aerodynamic model has been developed for the purpose of sizing the rotary wing ejector.

A blade element, prescribed vortex wake model based on Landgrebe's work is implemented for this study [Landgrebe, 1971 and 1972]. A general schematic of the wake generated by a rotor in hover is presented in Figure 11 [Stepniewski and Keys, 1984].

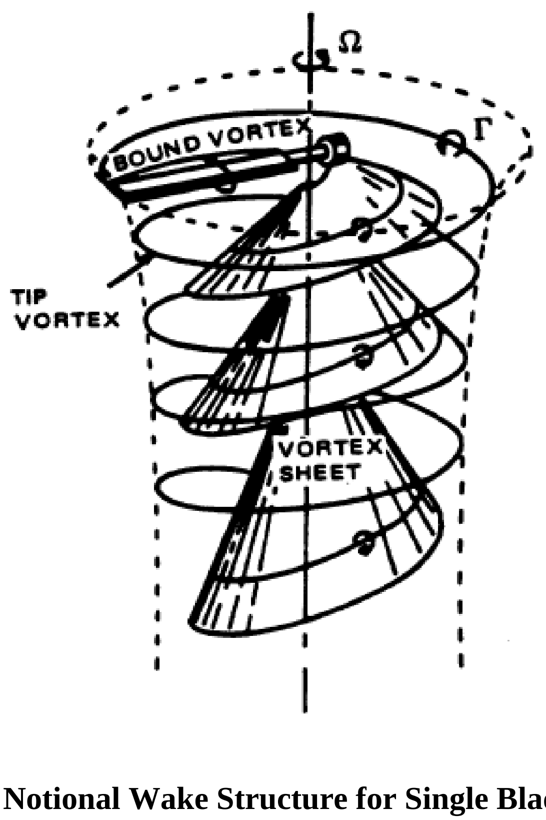

Figure 11: Notional Wake Structure for Single Blade in Hover

The wake geometry is a function of the rotor geometry, including twist and taper, and thrust. The radial induced velocity distribution, or inflow, is determined by applying the Biot-Savart law.

$$\textbf{(1)} \quad d\vec{v} = \frac{\Gamma\left(d\vec{s} \times \vec{r}\right)}{4\pi\left|r\right|^{3}}$$

The term $\vec{r}$ is the distance from the point at which the change in induced velocity, $d\vec{v}$, is calculated to the vortex filament, and $d\vec{s}$ is the length of the vortex filament with strength Γ. This relationship is shown in Figure 12.

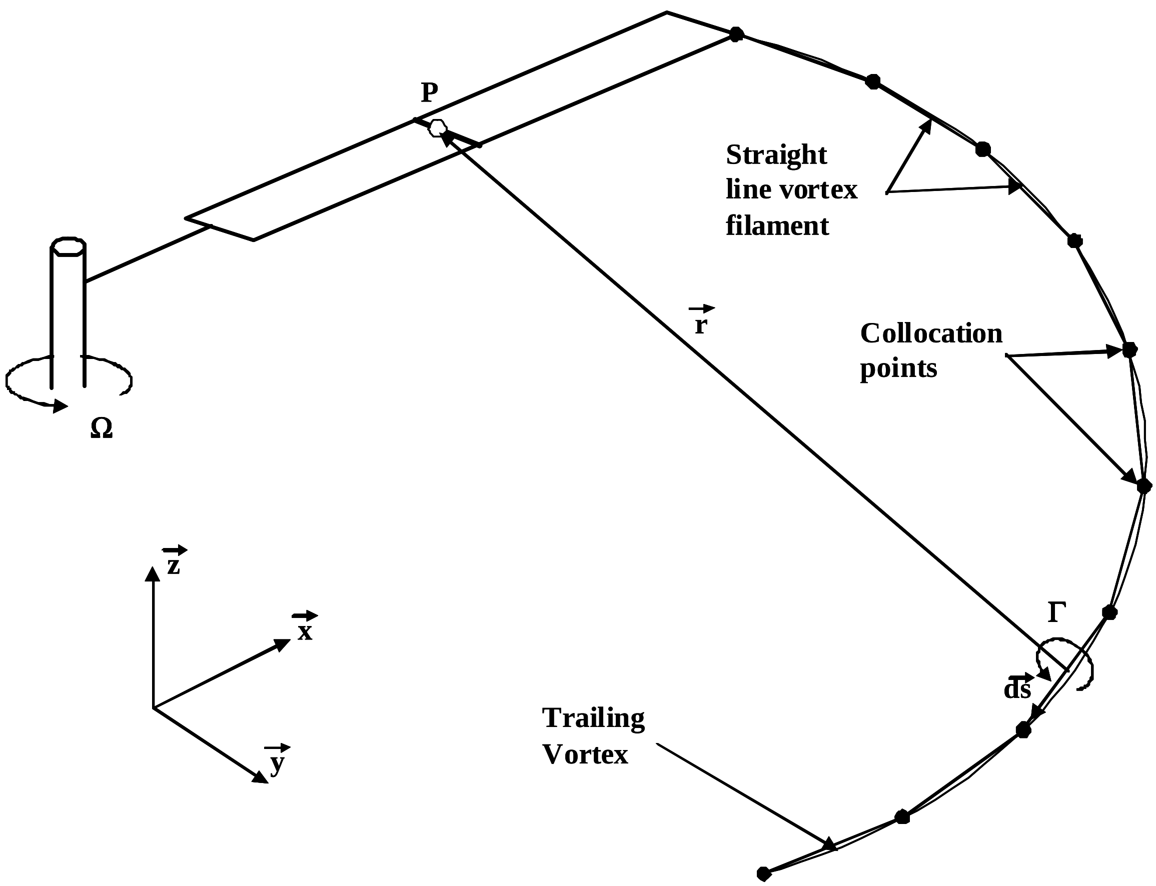

Figure 12: Trailing Vortex Discretization Method

The orientation of a blade element for a hovering rotor is presented in Figure 13. The vertical velocity component, $\vec{V}_P$, is the sum of the contributions of all of the vortex filaments in the wake acting on the blade element. The wake geometry is separated into the tip vortex and trailing vortex sheet. The tip vortex geometry is defined by the following two equations.

$$\textbf{(2)} \quad \frac{z_{tip}}{R} = \begin{cases} -0.25(C_T/\sigma + 0.001\theta_{tw})\psi_w, & 0 \le \psi_w \le 2\pi/N_b \\ (z_{tip}/R)_{\psi_w = 2\pi/N_b} - (1 + 0.01\theta_{tw})\sqrt{C_T}(\varphi_w - 2\pi/N_b), & \psi_w \ge 2\pi/N_b \end{cases}$$

$$\textbf{(3)} \quad y_{tip}/R = A + (1 - A)e^{(-(0.145 + 27C_T)\psi_w)}$$

Where y_{tip} and z_{tip} are the lateral and vertical displacements of the vortex filament. The trailing vortex sheet geometry varies linearly as a function of the radial distance from the inner end definition to the outer end definition. The inner end of the trailing vortex sheet geometry is defined by the following equation.

$$\textbf{(4)} \quad \left.\frac{z_{tip}}{R}\right|_{r=0} = \begin{cases} 0, & 0 \le \psi_w \le 2\pi/N_b \\ \theta_{tw}/128(0.45\theta_{tw} + 18)\sqrt{C_T/2}(\theta_{tw} - \pi/2), & \psi_w \ge 2\pi/N_b \end{cases}$$

The outer end of the trailing vortex sheet geometry is given by the relation below.

$$\textbf{(5)} \quad \left.\frac{z_{tip}}{R}\right|_{r=1} = \begin{cases} -2.2\sqrt{C_T/2}\psi_w, & 0 \le \psi_w \le 2\pi/N_b \\ -2.2\sqrt{C_T/2}(2\pi/N_b) - 2.7\sqrt{C_T/2}(\psi_w - 2\pi/N_b), & \psi_w \ge 2\pi/N_b \end{cases}$$

The trailing vortex sheet is discretized into trailing vortices at each blade element along the radial length of the blade. The trailing vortices and the tip vortex are then split into vortex filaments, where the Biot-Savart law is applied to a point, P, on the rotor blade as shown in Figure 12.

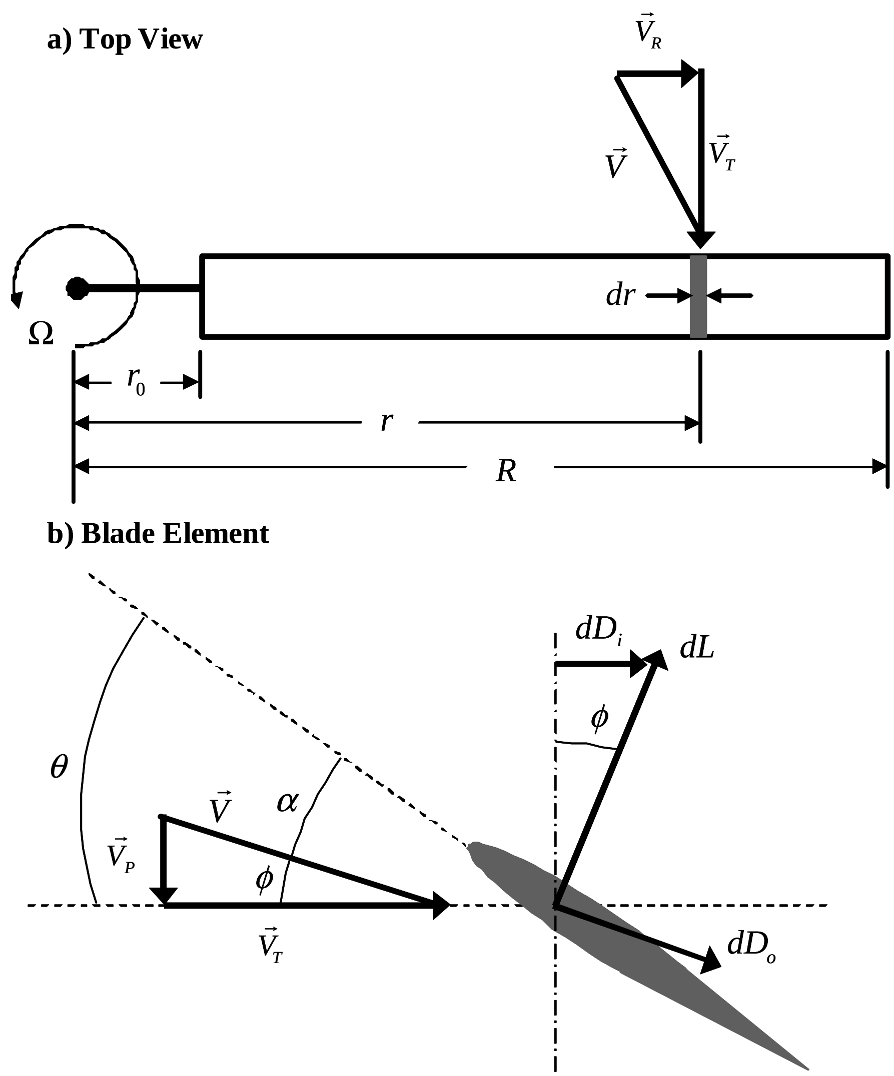

Figure 13: Blade Element Orientation

The nondimensional thrust and power for the rotor are given by the following relationships.

(6) $$C_T = \sum_{r=r_0}^{R} \frac{\sigma}{2}\left(r^2 + \lambda^2\right)\left(C_l \cos(\phi) - C_d \sin(\phi)\right)dr$$

(7) $$C_P = \sum_{r=r_0}^{R} \frac{\sigma}{2}\left(r^2 + \lambda^2\right)\left(C_l \sin(\phi) + C_d \cos(\phi)\right)rdr$$

Where λ represents the rotor inflow. The nondimensional thrust C_T calculated in Eq. (6) is compared to the nondimensional vehicle gross weight, C_W, in order to determine the rotor trim state in hover.

$$\textbf{(8)} \quad C_W = \frac{GW}{\rho A(\Omega R)^2}$$

A trim procedure adjusts the collective blade pitch angle to drive the difference between the nondimensional weight and thrust to zero; thereby trimming the rotor.

Gas flow of high velocity and temperature is ejected from the tip region of a reaction drive rotor into the surrounding flow field. Previous research by Spence (1956), Ives and Melnik (1974), and Dippold (2003) with jet-flapped wings and jet-wings have shown that a wing with jet exhausting from the trailing edge alters the pressure distribution and the associated lift and drag characteristics. With this evidence, computational fluid dynamics appears to be the minimum level of modeling fidelity to compute the required air loads need for this rotor problem. Additionally, to achieve a trimmed flight condition for a reaction drive rotor, the jet thrust available and the jet thrust required must be equal to produce a given amount of rotor thrust. This additional degree of freedom in the trim procedure requires a thermodynamic analysis to determine the jet flow conditions at the nozzle and dictates the use of computational fluid dynamics to predict the air loads with the inclusion of any effects the jet flow may have.

3.2 Reaction Drive Rotor Thermodynamics

The reaction drive rotor is analogous to a turbine, where compressed gas is expanded to produce work. In this case, compressed gas travels up a fixed duct, transitioning to a rotating duct, then turned 90° into a rotating duct within the blade. The gas travels to the end of the rotating duct, turns 90° again, and is expanded through a nozzle to produce thrust. In addition, a combustion chamber located upstream of the nozzle is included in this research. The thermal energy added to the air flow allows for a reduced mass flow rate for a constant nozzle thrust. This results in a smaller duct within the blade and lower rotor solidity. The basic operation of a reaction drive rotor is presented in Figure 14.

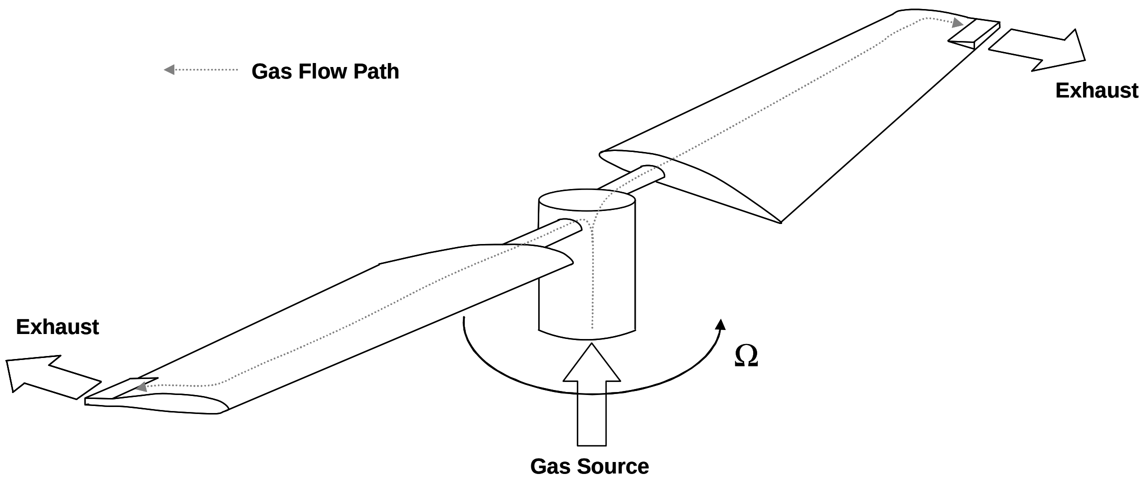

Figure 14: Reaction Drive Rotor Schematic

The reaction drive rotor configuration considered in this research is subdivided into several components: rotor-head supply duct, blade duct, combustion chamber, and converging-diverging nozzle. Continuity, momentum, and energy are applied to control volumes around each component. Assuming the flow through the system is steady, continuity in integral form is given below.

$$\textbf{(9)} \quad \int_{CS} \rho \vec{V} \cdot d\vec{A} = 0$$

Neglecting body forces, the momentum relation for a steady flow is defined by the following relation.

$$\textbf{(10)} \quad 0 = \int_{CS} \left[\left(\rho \vec{V} \cdot d\vec{A} \right) \vec{V} - p d\vec{A} \right]$$

Applying the First Law of Thermodynamics to a control volume, assuming steady flow, with no work added, and neglecting gravity, results in the relation given below.

(11) $$\dot{q} = \int_{CS} \left[\rho \left(e + \frac{V^2}{2} \right) + p \right] \vec{V} \cdot d\vec{A}$$

The rotor-head supply duct provides the flow path from the gas source to the rotor hub. There may be varying cross sectional areas and shapes, baffles, turns, and other geometric features dictated by the layout of the engines, airframe, and rotor. Relationships for the frictional losses for these types of duct configurations applied to reaction drive rotors have been investigated by Henry (1953), Hall (1995), and Tai (1998). Equations (9) and (11) are applied to a duct section, shown in Figure 15, assuming a constant cross section duct that with adiabatic, incompressible, and fully developed laminar flow.

(12) $$\left(e_2 - e_1\right) = \frac{p_2 - p_1}{\rho}$$

The terms on the left hand side of equation (12) represents the irreversible conversion of energy from mechanical energy to thermal energy, or head loss. The pressure difference between station 1 and station 2 for laminar flow is defined by the following relationship.

(13) $$p_2 - p_1 = 32 \frac{l}{d} \frac{\mu \overline{V}}{d}$$

Equation (13) is substituted into equation (12), resulting in the head loss relation.

(14) $$h_l = \frac{64}{\mathrm{Re}} \frac{l}{d} \frac{\overline{V}^2}{2}$$

The head loss for turbulent flow is empirically based, resulting in the following definition [Fox and McDonald, 1998].

(15) $h_l = f\,\dfrac{l}{d}\dfrac{\overline{V}^2}{2}$

For turbulent flows, the friction factor, *f*, can be found in the work by Moody (1944). An empirical correction to equations (14) and (15) applied to the bend duct section relate l/d to r_d/d, presented in Figure 15b [Fox and McDonald, 1998].

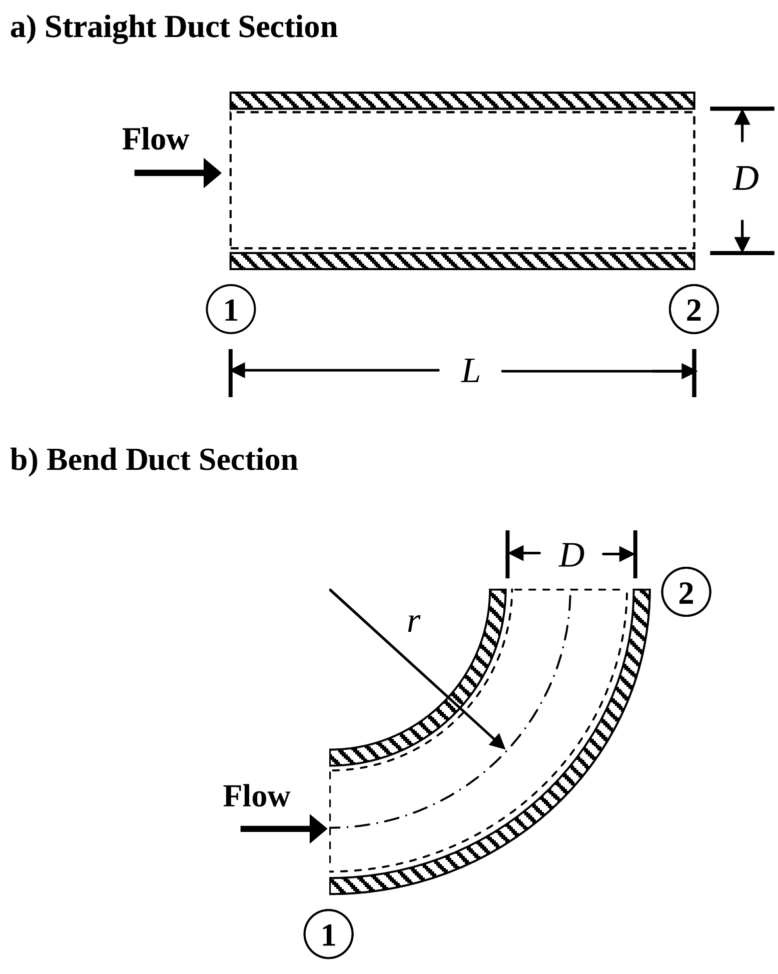

Figure 15: Straight and Bend Duct Section Schematics

Temperature and pressure as functions of Mach number at the entrance and exit are determined by assuming the flow is an ideal gas, isentropic, and constant-specific-heat; resulting in the following two relationships.

(16) $$\frac{T_o}{T} = 1 + \left(\frac{\gamma - 1}{2}\right) M^2$$

(17) $$\frac{p_o}{p} = \left[1 + \left(\frac{\gamma - 1}{2}\right) M^2\right]^{\gamma/(\gamma-1)}$$

The mass flow rate of the air through the duct is related to the flow area for an isentropic ideal gas with constant-specific-heat through the relationship below.

(18) $$\dot{m} = AMp_o \sqrt{\frac{\gamma}{R_{gas} T_o}} \Bigg/ \left(1 + \left(\frac{\gamma - 1}{2}\right) M^2\right)^{(\gamma+1)/[2(\gamma-1)]}$$

The rotating duct within the rotor blade delivers air from the rotor hub to the blade tip. The head loss for rotating duct, shown in Figure 16, is computed using equations (14) and (15). Equation (11) can be applied to the control volume in a rotating reference frame, given the following relationship.

(19) $$\dot{q} = \int_{CS} \left[\rho \left(e + \frac{V^2 + (\Omega r)^2}{2} \right) + p \right] \vec{V} \cdot d\vec{A}$$

The term, $(\Omega r)^2 / 2$, is the kinetic energy added to the fluid due to the rotation; which is typically referred to as centrifugal pumping. Applying equation (9) and (19) to the control volume in Figure 16 assuming adiabatic, incompressible, and fully developed flow results in the following relation.

(20) $$0 = \frac{\Omega^2 \left(r_2^2 - r_1^2\right)}{2} + \frac{p_2 - p_1}{\rho} - h_l$$

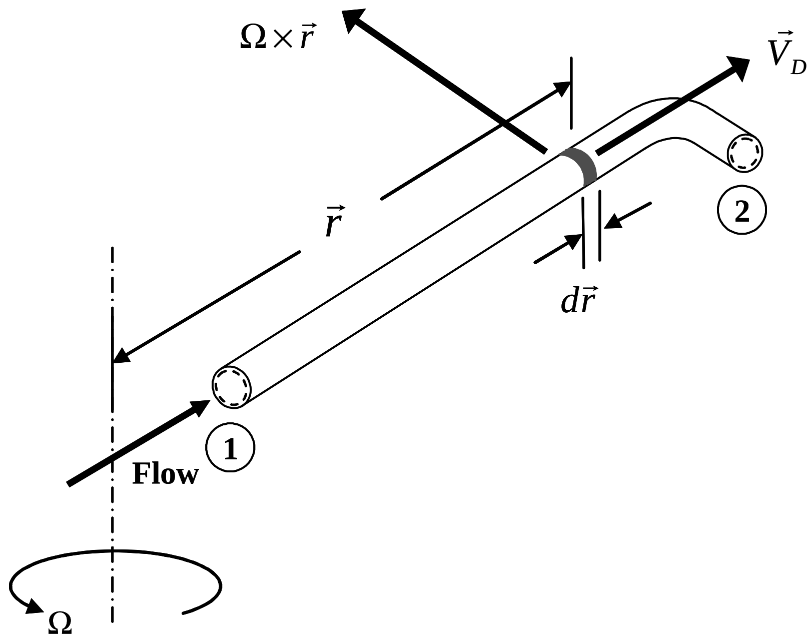

Figure 16: Rotating Duct Schematic

The combustion chamber adds thermal energy to the air flow by mixing and combusting fuel. This is analogous to an afterburner on a turbine engine and is the source for the name "tip jet" that may be referred to when discussing reaction drive rotor configurations. Equations (9) and (11) applied to the control volume in Figure 17 for an ideal gas with constant specific heat results in the following relation.

(21) $\dot{m}_{fuel} LHV = \dot{m}_{air} c_p \left(T_2 - T_1\right)$

The fuel-to-air ratio is defined as the fuel flow rate divided by the air flow rate.

(22) $far = \dfrac{\dot{m}_{fuel}}{\dot{m}_{air}}$

The ratio of fuel-to-air ratio to stoichiometric fuel-to-air ratio, or equivalence ratio is defined by the following relationship.

(23) $\Phi = \dfrac{far}{far_{st}}$

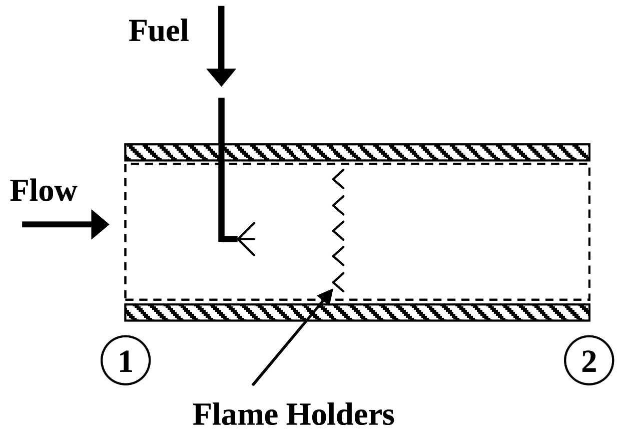

Figure 17: Combustion Chamber Schematic

The final component to the reaction drive system is a converging-diverging nozzle where the hot gas is expanded into the atmosphere, converting thermal energy into kinetic energy; thereby producing thrust. Equation (11) applied to the control volume in Figure 18 for an ideal gas with constant specific heat results in the following relation.

(24) $$0 = \left(\rho\left(e + \frac{V^2}{2}\right) + p\right)_2 - \left(\rho\left(e + \frac{V^2}{2}\right) + p\right)_1$$

Equation (24) is rewritten using the definition of flow work and enthalpy provided by Cengel and Boles (1998).

(25) $$h_2 - h_1 = \frac{V_1^2 - V_2^2}{2}$$

The nozzle throat area, assuming sonic conditions, is defined below.

(26) $$A_t = \frac{\dot{m}}{p_o}\sqrt{\frac{R_{gas}T_o}{\gamma}}\left(\frac{\gamma+1}{2}\right)^{(\gamma+1)/[2(\gamma-1)]}$$

The nozzle exit area is then given by the following relationship.

(27) $$A_2 = \frac{A_t}{M_2}\left(\left(\frac{2}{\gamma+1}\right)\left(1 + \frac{\gamma-1}{2}M_2^2\right)\right)^{(\gamma+1)/[2(\gamma-1)]}$$

The thrust of the rotating nozzle is defined by the following relation.

(28) $FN_2 = \dot{m}(V_2 - \Omega r_2)$

The term, $-\dot{m}\Omega r_2$, is the force imparted on the rotor at the nozzle radial location due to the acceleration of the gas from the fixed to the rotating reference frame.

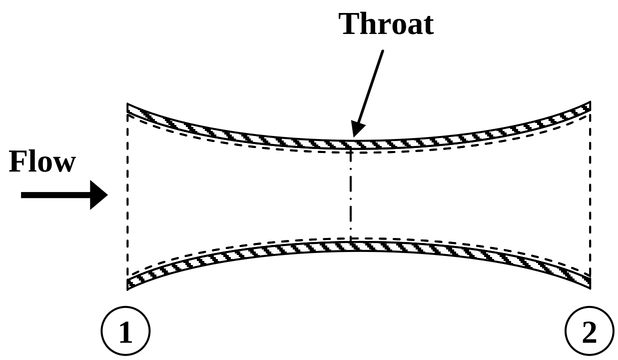

Figure 18: Converging-Diverging Nozzle Schematic

3.3 Ejector Nozzle Thermodynamics

The ejector may be separated into four flow elements and three geometric components. The four flow elements are the primary and secondary flows, mixing regime, and ejector exhaust flow. The three geometric components of the ejector consist of a primary nozzle, secondary inlets, and ejector shroud. A thermodynamic representation of this system is subdivided into three components; secondary inlets, primary nozzle, and ejector exit nozzle.

The secondary inlets provide a flow path from the free stream to the mixing plane and typically diffuse the flow to a specified velocity. The primary nozzle is assumed to be convergent-divergent, resulting in supersonic flow. The ejector exit gas mass flow rate, shown in Figure 19, will be a sum of primary and secondary gas mass flow rates; represented by the following form of the continuity equation.

(29) $\dot{m}_{1P} + \dot{m}_{1S} = \dot{m}_2$

The static pressure of the secondary and primary flow is assumed to be equal at the mixing plane. Similarly, the momentum relation, equation (10), applied to the control volume shown in Figure 19, assuming ideal gas and uniform pressure, temperature and velocity distributions, reduces to the following relationship.

(30) $$[(\dot{m}V + p)A]_{1Su} + [(\dot{m}V + p)A]_{1Sl} + [(\dot{m}V + p)A]_{1P} = [(\dot{m}V + p)A]_2$$

The subscripts *u* and *l* denote the upper and lower secondary flows, which are assumed to be asymmetric for this ejector application. Equation (11) applied to the control volume shown in Figure 19, assuming adiabatic and subsonic exit flow, in addition to those listed above, gives the following relation.

(31) $$\left[\left(\rho\left(e+\frac{V^2}{2}\right)+p\right)VA\right]_{1Su} + \left[\left(\rho\left(e+\frac{V^2}{2}\right)+p\right)VA\right]_{1Sl} + \left[\left(\rho\left(e+\frac{V^2}{2}\right)+p\right)VA\right]_{1P} = \left[\left(\rho\left(e+\frac{V^2}{2}\right)+p\right)VA\right]_2$$

Figure 19 shows a simplified schematic with parallel shroud walls. The ejector exit area is a variable used to close the continuity, momentum, and energy relations above. Therefore, the ejector shroud walls may not be parallel, as depicted.

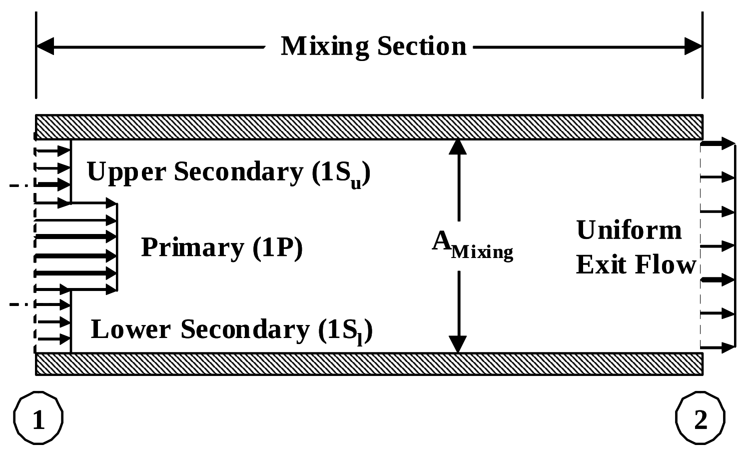

Figure 19: Ejector Nozzle Schematic

A major assumption is that the secondary and primary flows are fully mixed at the ejector exit. This assumption is necessary to close equations (9), (10), and (11) for the control volume in Figure 19. The reality of this problem is that there will not be sufficient length to completely mix the primary and secondary flows. To account for non-ideal mixing, an empirical relationship relating the partially mixed thrust to the fully mixed and unmixed ideal thrust is implemented [Nordstrom *et al*., 1975].

(32) $$FN_{jet,par} = f_{me}\left(FN_{jet,full-mix} - FN_{jet,un-mix}\right) + FN_{jet,un-mix}$$

The term, f_{me}, is defined as the mixing effectiveness and is taken from curve shown in Figure 20. The mixing effectiveness is empirically related to the primary nozzle geometry (perimeter and equivalent diameter) and the ejector shroud length. The primary nozzle used for this empirical relation is fluted, and therefore the perimeter, P, is much greater than a rectangular nozzle. Additionally, the flutes act to enhance the mixing between the high and low speed flows.

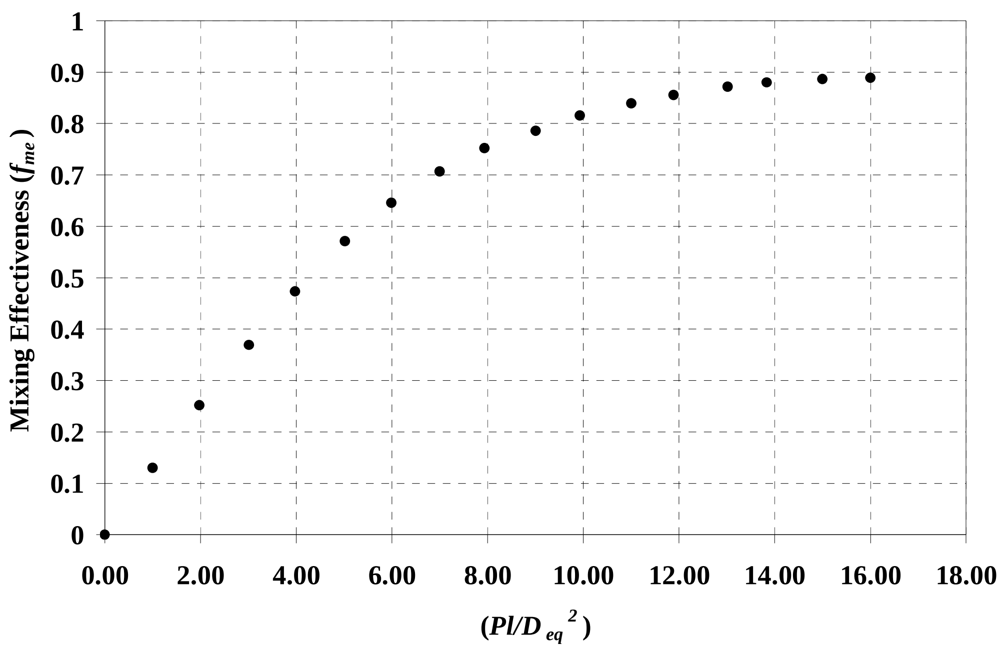

Figure 20: Empirical Mixing Effectiveness [Nordstrom *et al.*, 1975]

3.4 Computational Fluid Dynamics

The three fundamental equations governing the flow properties of a fluid are the continuity equation, momentum equation, and energy equation. Computational fluid dynamics is based on these governing equations applied across a small fluid element or finite volume.

The continuity equation is the result of applying the conservation of mass principle to a finite volume.

(33) $$\frac{\partial \rho}{\partial t} + \nabla \cdot \left(\rho \vec{V}\right) = 0$$

The gradient, ∇, represents the maximum magnitude and direction of the rate of change at a given point and written in Cartesian coordinates results in the relation given below.

(34) $$\nabla = \frac{\partial}{\partial x} i + \frac{\partial}{\partial y} j + \frac{\partial}{\partial z} k$$

The momentum equation represents the physical principle that force equals the time rate change of momentum, which is commonly referred to as Newton's second law. The forces acting on a small fluid element consist of surface forces that are the result of viscous stress and pressure and body forces that include gravitational, electromagnetic, Coriolis, and centrifugal. Neglecting all of the body forces with the exception of gravity, the momentum equation may be written in the form given below.

(35) $$\rho \vec{g} + \nabla \tau = \rho \left(\frac{\partial \vec{V}}{\partial t} + \left(\nabla \vec{V} \cdot \vec{V}\right) \right)$$

The term, τ, represents the viscous normal and shear stresses on the small fluid element and is referred to as the viscous stress tensor.

$$\tau = \begin{bmatrix} \sigma_{xx} & \tau_{xy} & \tau_{xz} \\ \tau_{yx} & \sigma_{yy} & \tau_{yz} \\ \tau_{zx} & \tau_{zy} & \sigma_{zz} \end{bmatrix} \quad \textbf{(36)}$$

For a Newtonian fluid, the viscous stresses are linearly proportional to the rates of strain and can be written in terms of the fluid velocity gradients and fluid properties. In addition, the fluid is assumed to be isotropic, where the bulk viscosity, $\lambda + 2/3\mu$, is equal to zero. The viscous stresses are then defined by the following relations.

$$\begin{aligned}
\sigma_{xx} &= -\frac{2}{3}\mu\left(\frac{\partial u}{\partial x} + \frac{\partial v}{\partial y} + \frac{\partial w}{\partial z}\right) + 2\mu\frac{\partial u}{\partial x} \\
\sigma_{yy} &= -\frac{2}{3}\mu\left(\frac{\partial u}{\partial x} + \frac{\partial v}{\partial y} + \frac{\partial w}{\partial z}\right) + 2\mu\frac{\partial v}{\partial y} \\
\sigma_{zz} &= -\frac{2}{3}\mu\left(\frac{\partial u}{\partial x} + \frac{\partial v}{\partial y} + \frac{\partial w}{\partial z}\right) + 2\mu\frac{\partial w}{\partial z} \\
\tau_{xy} &= \tau_{yx} = \mu\left(\frac{\partial u}{\partial y} + \frac{\partial v}{\partial x}\right) \\
\tau_{yz} &= \tau_{zy} = \mu\left(\frac{\partial w}{\partial y} + \frac{\partial v}{\partial z}\right) \\
\tau_{zx} &= \tau_{xz} = \mu\left(\frac{\partial u}{\partial z} + \frac{\partial w}{\partial x}\right)
\end{aligned} \quad \textbf{(37)}$$

With the definitions presented in equation (37), equation (35) is written as the Navier-Stokes equations in Cartesian coordinates.

$$\begin{aligned}
\rho g_x - \frac{\partial p}{\partial x} + \frac{\partial}{\partial x}(\sigma_{xx}) + \frac{\partial}{\partial y}(\tau_{xy}) + \frac{\partial}{\partial z}(\tau_{xz}) &= \rho\left(\frac{\partial u}{\partial t} + u\frac{\partial u}{\partial x} + v\frac{\partial u}{\partial y} + w\frac{\partial u}{\partial z}\right) \\
\rho g_y - \frac{\partial p}{\partial y} + \frac{\partial}{\partial x}(\tau_{yx}) + \frac{\partial}{\partial y}(\sigma_{yy}) + \frac{\partial}{\partial z}(\tau_{yz}) &= \rho\left(\frac{\partial v}{\partial t} + u\frac{\partial v}{\partial x} + v\frac{\partial v}{\partial y} + w\frac{\partial v}{\partial z}\right) \\
\rho g_z - \frac{\partial p}{\partial z} + \frac{\partial}{\partial x}(\tau_{zx}) + \frac{\partial}{\partial x}(\tau_{zy}) + \frac{\partial}{\partial z}(\sigma_{yy}) &= \rho\left(\frac{\partial w}{\partial t} + u\frac{\partial w}{\partial x} + v\frac{\partial w}{\partial y} + w\frac{\partial w}{\partial z}\right)
\end{aligned} \quad \textbf{(38)}$$

For many aerodynamic applications, the fluid, air, may be assumed to be a perfect gas. The temperature, pressure and density are then related by the equation of state.

(39) $p = \rho R_{gas} T$

The gas temperature is included as an independent variable, requiring the first law of thermodynamics in the form of the energy equation to be included in the formulation.

The energy equation is a representation of the fundamental physical principle where energy can be neither created nor destroyed, only converted from one form to another. This relationship applied to a fluid element, neglecting volumetric heating, is given by the following equation.

(40) $\frac{\partial}{\partial t}(\rho E) + \nabla \cdot \rho E\vec{V} = -\nabla \dot{q} - \nabla \cdot \left(p\vec{V}\right) + \nabla \cdot \tau\vec{V}$

The total energy increase inside the fluid element is represented by the following relation.

(41) $E = e + \frac{1}{2}\left(u^2 + v^2 + w^2\right) - gh$

The internal energy for a perfect gas is related to the gas temperature through the specific heat at constant volume.

(42) $e = c_v dT$

The heat flux, $\dot{q}$, is related to the gas temperature through Fourier's law of conduction.

(43) $\dot{q} = -k\nabla T$

Substituting equations (36), (37), (41), (42), and (43) results in the following form of the energy equation, written in Cartesian coordinates.

(44)
$$\rho c_v \frac{\partial T}{\partial t} + \rho \frac{\partial}{\partial t}\left(\frac{1}{2}\left(u^2 + v^2 + w^2\right) - gh\right) + \rho c_v \left(\frac{\partial (Tu)}{\partial x} + \frac{\partial (Tv)}{\partial y} + \frac{\partial (Tw)}{\partial z}\right)$$
$$+ \rho\left(\frac{V^2}{2} - gh\right)\left(\frac{\partial u}{\partial x} + \frac{\partial v}{\partial y} + \frac{\partial w}{\partial z}\right) = k\left(\frac{\partial^2 T}{\partial x^2} + \frac{\partial^2 T}{\partial y^2} + \frac{\partial^2 T}{\partial z^2}\right) - \frac{\partial (pu)}{\partial x} - \frac{\partial (pv)}{\partial y} - \frac{\partial (pw)}{\partial z}$$
$$+ \frac{\partial}{\partial x}\left(u\sigma_{xx} + v\tau_{xy} + w\tau_{xz}\right) + \frac{\partial}{\partial y}\left(u\tau_{yx} + v\sigma_{yy} + w\tau_{yz}\right) + \frac{\partial}{\partial z}\left(u\tau_{zx} + v\tau_{zy} + w\sigma_{zz}\right)$$

The mechanical energy is represented by the dot product of the momentum equation and the velocity vector.

(45)
$$\left[\rho\left(\frac{\partial \vec{V}}{\partial t} + \left(\nabla \vec{V} \cdot \vec{V}\right)\right) - \rho g + \nabla \tau\right] \cdot \vec{V} = 0$$

Expanding equation (45) and applying the chain rule gives the following relation.

(46)
$$\frac{\rho}{2}\left(\frac{\partial u^2}{\partial t} + \frac{\partial v^2}{\partial t} + \frac{\partial w^2}{\partial t}\right) + \frac{\rho}{2}\left(\frac{\partial u^2}{\partial x} + \frac{\partial v^2}{\partial y} + \frac{\partial w^2}{\partial z}\right)u + \frac{\rho}{2}\left(\frac{\partial u^2}{\partial x} + \frac{\partial v^2}{\partial y} + \frac{\partial w^2}{\partial z}\right)v$$
$$+ \frac{\rho}{2}\left(\frac{\partial u^2}{\partial x} + \frac{\partial v^2}{\partial y} + \frac{\partial w^2}{\partial z}\right)w - \frac{\partial}{\partial t}(\rho gh) - \frac{\partial}{\partial x}(\rho ghu) - \frac{\partial}{\partial y}(\rho ghv) - \frac{\partial}{\partial z}(\rho ghw)$$
$$u\left(\frac{\partial \sigma_{xx}}{\partial x} + \frac{\partial \tau_{yx}}{\partial y} + \frac{\partial \tau_{zx}}{\partial z}\right) + v\left(\frac{\partial \tau_{xy}}{\partial x} + \frac{\partial \sigma_{yy}}{\partial y} + \frac{\partial \tau_{zy}}{\partial z}\right) + w\left(\frac{\partial \tau_{xz}}{\partial x} + \frac{\partial \tau_{yz}}{\partial y} + \frac{\partial \sigma_{zz}}{\partial z}\right) = 0$$

Subtracting the mechanical energy from the total energy results in the thermal energy equation.

(47)
$$\rho c_v \frac{\partial T}{\partial t} + \rho c_v \left(\frac{\partial (Tu)}{\partial x} + \frac{\partial (Tv)}{\partial y} + \frac{\partial (Tw)}{\partial z}\right) = \frac{\partial}{\partial x}\left(k\frac{\partial T}{\partial x}\right) + \frac{\partial}{\partial y}\left(k\frac{\partial T}{\partial y}\right) + \frac{\partial}{\partial z}\left(k\frac{\partial T}{\partial z}\right)$$
$$- \frac{\partial}{\partial x}(pu) - \frac{\partial}{\partial y}(pv) - \frac{\partial}{\partial z}(pw) + \frac{\partial u}{\partial x}\sigma_{xx} + \frac{\partial v}{\partial x}\tau_{xy} + \frac{\partial w}{\partial x}\tau_{xz} + \frac{\partial u}{\partial y}\tau_{yx} + \frac{\partial v}{\partial y}\sigma_{yy} + \frac{\partial w}{\partial y}\tau_{yz}$$
$$+ \frac{\partial u}{\partial z}\tau_{zx} + \frac{\partial v}{\partial z}\tau_{zy} + \frac{\partial w}{\partial z}\sigma_{zz}$$

Equations (33), (38), (39), and (47) are the set of six equations in terms of six unknowns that mathematically represent the behavior of a fluid with respect to a Cartesian coordinate reference frame. These equations can be further simplified by writing them in the following vector form.

(48) $$\frac{\partial \vec{Q}}{\partial t} + \frac{\partial \vec{F}}{\partial x} + \frac{\partial \vec{G}}{\partial y} + \frac{\partial \vec{H}}{\partial z} - \vec{B} = 0$$

Equation (48) orders the flow variables by conservative, flux, and body; given by the following set of relationships.

(49) $$\vec{Q} = \begin{bmatrix} \rho \\ \rho u \\ \rho v \\ \rho w \\ \rho(C_V T) \end{bmatrix}$$

(50) $$\vec{F} = \begin{bmatrix} \rho u \\ \rho u^2 + p - \sigma_{xx} \\ \rho v u - \tau_{xy} \\ \rho w u - \tau_{xz} \\ \rho(C_V T)u + pu - k\frac{\partial T}{\partial x} - u\sigma_{xx} - v\tau_{xy} - w\tau_{xz} \end{bmatrix}$$

(51) $$\vec{G} = \begin{bmatrix} \rho v \\ \rho u v - \tau_{yx} \\ \rho v^2 + p - \sigma_{yy} \\ \rho w v - \tau_{yz} \\ \rho(C_V T)v + pv - k\frac{\partial T}{\partial y} - u\tau_{yx} - v\sigma_{yy} - w\tau_{yz} \end{bmatrix}$$

(52) $$\vec{H} = \begin{bmatrix} \rho w \\ \rho u w - \tau_{zx} \\ \rho v w - \tau_{zy} \\ \rho w^2 + p - \sigma_{zz} \\ \rho(C_V T)w + pw - k\frac{\partial T}{\partial z} - u\tau_{zx} - v\tau_{zy} - w\sigma_{zz} \end{bmatrix}$$

$$\textbf{(53)} \quad \vec{B} = \begin{bmatrix} 0 \\ \rho g_x \\ \rho g_y \\ \rho g_z \\ 0 \end{bmatrix}$$

3.4.1 Reynolds Averaging

The Navier-Stokes equations may be solved by direct numerical simulation (DNS). However, this approach requires a fine enough mesh to capture the smallest spatial and temporal scales required by the fluid problem at hand. A more common approach to model flow over a wide range of conditions is to use the Reynolds-averaged Navier-Stokes equations (RANS), which are time averaged viscous equations for the motion of turbulent flows. The Reynolds averaged Navier-Stokes equations, or RANS, are arrived at by decomposing the dependant variables into mean and fluctuating components.

$$\textbf{(54)} \quad \vec{V} = \vec{U} + \vec{v}', \quad p = P + p', \quad T = \theta_T + \theta_T'$$

The effects of the fluctuating density are negligible, while the effects of the mean density are not [Bradshaw *et al*., 1981; Tannehill *et al*., 1997]. The fluctuating kinetic energy dissipation results in small temperature rises, which may be neglected when modeling the eddy viscosity of high Reynolds number flows [Krist *et al*., 1998]. Substituting the terms from equation (54) into equations (49) through (53) results in the following relationships; written in Cartesian coordinates.

$$\textbf{(55)} \quad \vec{Q} = \begin{bmatrix} \rho \\ \rho u \\ \rho v \\ \rho w \\ \rho(C_V T) \end{bmatrix}$$

$$\textbf{(56)}\quad \vec{F} = \begin{bmatrix} \rho U \\ \rho U^2 + p - \sigma_{xx} + \rho\left(\overline{u'u'}\right) \\ \rho UV - \tau_{xy} + \rho\left(\overline{u'v'}\right) \\ \rho UW - \tau_{xz} + \rho\left(\overline{u'w'}\right) \\ \rho(C_V\theta)U + pU - k\dfrac{\partial\theta}{\partial x} - U\sigma_{xx} - V\tau_{xy} - W\tau_{xz} + \rho C_V\,\overline{\theta'u'} \end{bmatrix}$$

$$\textbf{(57)}\quad \vec{G} = \begin{bmatrix} \rho V \\ \rho UV - \tau_{yx} + \rho\left(\overline{u'v'}\right) \\ \rho V^2 + p - \sigma_{yy} + \rho\left(\overline{v'v'}\right) \\ \rho WV - \tau_{yz} + \rho\left(\overline{w'v'}\right) \\ \rho(C_V\theta)V + pV - k\dfrac{\partial\theta}{\partial y} - U\tau_{yx} - V\sigma_{yy} - W\tau_{yz} + \rho C_V\,\overline{\theta'v'} \end{bmatrix}$$

$$\textbf{(58)}\quad \vec{H} = \begin{bmatrix} \rho W \\ \rho UW - \tau_{zx} + \rho\left(\overline{u'w'}\right) \\ \rho VW - \tau_{zy} + \rho\left(\overline{v'w'}\right) \\ \rho W^2 + p - \sigma_{zz} + \rho\left(\overline{w'w'}\right) \\ \rho(C_V\theta)W + pW - k\dfrac{\partial\theta}{\partial z} - U\tau_{zx} - V\tau_{zy} - W\sigma_{zz} + \rho C_V\,\overline{\theta'w'} \end{bmatrix}$$

$$\textbf{(59)}\quad \vec{B} = \begin{bmatrix} 0 \\ \rho g_x \\ \rho g_y \\ \rho g_z \\ 0 \end{bmatrix}$$

3.4.2 Coordinate Transformation

Transforming the Navier-Stokes equations into a generalized, body-fitted, curvilinear coordinate system allows the formulation to be independent of the body geometry. This coordinate system allows for standard differencing schemes of the spatial derivatives and a straight forward application of the thin-layer approximation. The generalized coordinate transformation is defined by the following relation.

(60)
$$\begin{aligned}\xi &= \xi(x,y,z,t)\\ \eta &= \eta(x,y,z,t)\\ \zeta &= \zeta(x,y,z,t)\end{aligned}$$

The transformation Jacobian obtained through the chain rule for multi-variable functions is given by the following relationship [Vinokur, 1974].

(61)
$$J^{-1} = \begin{vmatrix} x_\xi & x_\eta & x_\zeta & x_t \\ y_\xi & y_\eta & y_\zeta & y_t \\ z_\xi & z_\eta & z_\zeta & z_t \\ 0 & 0 & 0 & 1 \end{vmatrix}$$

The terms in the Jacobian are shorthand for partial derivatives, i.e. $x_\xi = \partial x / \partial \xi$, etc… The transformation metrics are written below.

(62)
$$\begin{aligned}
\xi_x &= J\left(y_\eta z_\zeta - y_\zeta z_\eta\right) & \zeta_x &= J\left(y_\xi z_\eta - y_\eta z_\xi\right)\\
\xi_y &= J\left(x_\zeta z_\eta - x_\eta z_\zeta\right) & \zeta_y &= J\left(x_\eta z_\xi - x_\xi z_\eta\right)\\
\xi_z &= J\left(x_\eta y_\zeta - x_\zeta y_\eta\right) & \zeta_z &= J\left(x_\xi y_\eta - x_\eta y_\xi\right)\\
\eta_x &= J\left(y_\zeta z_\xi - y_\xi z_\zeta\right) & \xi_t &= -x_t \xi_x - y_t \xi_y - z_t \xi_z\\
\eta_y &= J\left(x_\xi z_\zeta - x_\zeta z_\xi\right) & \eta_t &= -x_t \eta_x - y_t \eta_y - z_t \eta_z\\
\eta_z &= J\left(x_\zeta y_\xi - x_\xi y_\zeta\right) & \zeta_t &= -x_t \zeta_x - y_t \zeta_y - z_t \zeta_z
\end{aligned}$$

The transformation Jacobian represents the inverse of the local grid cell volume, while the metrics represent the grid cell area projections. Combined, they give an indication of the quality of the grid. Applying the transformation to the Navier-Stokes equations, results in the following relation.

(63)
$$\frac{\partial \vec{\hat{Q}}}{\partial t} + \frac{\partial \vec{\hat{F}}}{\partial \xi} + \frac{\partial \vec{\hat{G}}}{\partial \eta} + \frac{\partial \vec{\hat{H}}}{\partial \zeta} - \vec{\hat{B}} = 0$$

The transformed conservative flow variable and flux vectors are given by the following relationships.

$$
\textbf{(64)}\quad \vec{\hat{Q}} = J^{-1}\begin{bmatrix} \rho \\ \rho u \\ \rho v \\ \rho w \\ \rho\left(C_V T + V^2/2\right) \end{bmatrix}
$$

$$
\textbf{(65)}\quad \vec{\hat{F}} = J^{-1}\begin{bmatrix} \rho V_\xi \\ \rho u V_\xi + \xi_x p - \left(\xi_x \sigma_{xx} + \xi_y \tau_{xy} + \xi_z \tau_{xz}\right) \\ \rho v V_\xi + \xi_y p - \left(\xi_x \tau_{yx} + \xi_y \sigma_{yy} + \xi_z \tau_{yz}\right) \\ \rho w V_\xi + \xi_z p - \left(\xi_x \tau_{zx} + \xi_y \tau_{zy} + \xi_z \sigma_{zz}\right) \\ \rho\left(C_V T + V^2/2\right) V_\xi + p V_\xi - \left(\xi_x \beta_x + \xi_y \beta_y + \xi_z \beta_z\right) \end{bmatrix}
$$

$$
\textbf{(66)}\quad \vec{\hat{G}} = J^{-1}\begin{bmatrix} \rho V_\eta \\ \rho u V_\eta + \eta_x p - \left(\eta_x \sigma_{xx} + \eta_y \tau_{xy} + \eta_z \tau_{xz}\right) \\ \rho v V_\eta + \eta_y p - \left(\eta_x \tau_{yx} + \eta_y \sigma_{yy} + \eta_z \tau_{yz}\right) \\ \rho w V_\eta + \eta_z p - \left(\eta_x \tau_{zx} + \eta_y \tau_{zy} + \eta_z \sigma_{zz}\right) \\ \rho\left(C_V T + V^2/2\right) V_\eta + p V_\eta - \left(\eta_x \beta_x + \eta_y \beta_y + \eta_z \beta_z\right) \end{bmatrix}
$$

$$
\textbf{(67)}\quad \vec{\hat{H}} = J^{-1}\begin{bmatrix} \rho V_\zeta \\ \rho u V_\zeta + \zeta_x p - \left(\zeta_x \sigma_{xx} + \zeta_y \tau_{xy} + \zeta_z \tau_{xz}\right) \\ \rho v V_\zeta + \zeta_y p - \left(\zeta_x \tau_{yx} + \zeta_y \sigma_{yy} + \zeta_z \tau_{yz}\right) \\ \rho w V_\zeta + \zeta_z p - \left(\zeta_x \tau_{zx} + \zeta_y \tau_{zy} + \zeta_z \sigma_{zz}\right) \\ \rho\left(C_V T + V^2/2\right) V_\zeta + p V_\zeta - \left(\zeta_x \beta_x + \zeta_y \beta_y + \zeta_z \beta_z\right) \end{bmatrix}
$$

$$
\textbf{(68)}\quad \vec{\hat{B}} = J^{-1}\begin{bmatrix} 0 \\ \rho g_x \\ \rho g_y \\ \rho g_z \\ 0 \end{bmatrix}
$$

The transformed velocity, conduction, and stresses are given by the following relations.

$$
\textbf{(69)}\quad \begin{aligned} V_\xi &= \left(\xi_t + \xi_x u + \xi_y v + \xi_z w\right) \\ V_\eta &= \left(\eta_t + \eta_x u + \eta_y v + \eta_z w\right) \\ V_\zeta &= \left(\zeta_t + \zeta_x u + \zeta_y v + \zeta_z w\right) \end{aligned}
$$

$$\beta_x = k\frac{\partial T}{\partial x} + u\sigma_{xx} + v\tau_{xy} + w\tau_{xz}$$

(70) $$\beta_y = k\frac{\partial T}{\partial y} + u\tau_{yx} + v\sigma_{yy} + w\tau_{yz}$$

$$\beta_z = k\frac{\partial T}{\partial z} + u\tau_{zx} + v\tau_{zy} + w\sigma_{zz}$$

3.4.3 Thin-Layer Approximation

For many aerodynamic problems the ratio of inertia forces to viscous forces, or Reynolds number, is high. This allows for the assumption that the viscous effects are predominant near the surface of a body and in the wake of the body, including shed and trailing vortices. Concentrating grid points in these regions results in a fine grid spacing normal to the surface, but a relatively course grid spacing tangentially along the surface. Resolving the viscous effects tangentially over the body surface requires large grids that are limited by computational power and time. Viscous effects for high Reynolds number flows are typically greater in the normal direction, thereby justifying the assumption that they are negligible in the tangential directions. The viscous terms in equation (52) can be separated, resulting in the following relationship.

(71) $$\frac{\partial \vec{\hat{Q}}}{\partial t} + \frac{\partial \vec{\hat{F}}}{\partial \xi} + \frac{\partial \vec{\hat{G}}}{\partial \eta} + \frac{\partial \vec{\hat{H}}}{\partial \zeta} - \frac{\partial \vec{\hat{F}}_v}{\partial \xi} - \frac{\partial \vec{\hat{G}}_v}{\partial \eta} - \frac{\partial \vec{\hat{H}}_v}{\partial \zeta} - \vec{\hat{B}} = 0$$

Applying the thin-layer approximation to equation (71) retains only the viscous terms in the normal direction.

(72) $$\frac{\partial \vec{\hat{Q}}}{\partial t} + \frac{\partial \vec{\hat{F}}}{\partial \xi} + \frac{\partial \vec{\hat{G}}}{\partial \eta} + \frac{\partial \vec{\hat{H}}}{\partial \zeta} - \frac{\partial \vec{\hat{H}}_v}{\partial \zeta} - \vec{\hat{B}} = 0$$

The viscous stress component, $\vec{\hat{H}}_v$, is given by the following relation.

$$\textbf{(73)} \quad \vec{\hat{H}}_v = \begin{bmatrix} 0 \\ \mu C_1 u_\zeta + \frac{\mu}{3} C_2 \zeta_x \\ \mu C_1 v_\zeta + \frac{\mu}{3} C_2 \zeta_y \\ \mu C_1 w_\zeta + \frac{\mu}{3} C_2 \zeta_z \\ \mu C_1 C_3 u_\zeta + \frac{\mu}{3} C_2 (\zeta_x u + \zeta_y v + \zeta_z w) \end{bmatrix}$$

The coefficients in equation (73) are defined below.

$$\textbf{(74)} \quad \begin{aligned} C_1 &= \zeta_x^2 + \zeta_y^2 + \zeta_z^2 \\ C_2 &= \zeta_x u_\zeta + \zeta_y v_\zeta + \zeta_z w_\zeta \\ C_3 &= \frac{(V^2)_\zeta}{2} + \frac{1}{\Pr(\gamma - 1)} (a^2)_\zeta \end{aligned}$$

3.4.4 Turbulence Modeling

Time averaging the Navier-Stokes equations creates additional unknowns, resulting in a closure problem. The turbulence model is then used to supplement the existing set of equations, thereby balancing the number unknowns with the number of equations [Wilcox, 1994]. Reynolds averaging reduces the number of grid points to resolve turbulent flows, greatly decreasing the computational time required to solve the flow problem.

There are many turbulence models available that predict turbulent fluid motion, ranging from algebraic to higher order differential field-equations. All of these approaches require the turbulent momentum flux and turbulent energy flux to be resolved through either algebraic relationships or numerically solving the transport equations [Hunt, 1999]. The turbulent momentum flux is given by the following relation.

$$\textbf{(75)} \quad \tau'_{ij} = -\rho \overline{u_i u_j}$$

Equation (75) is referred to as the Reynolds stress tensor and represents the apparent stresses on the fluid element that are not a result of the thermodynamic pressure or viscous stresses [Hinze, 1975]. The Boussinesq assumption, which relates the turbulent stresses to the rate of mean strain through an eddy viscosity, reduces the number of unknowns required to resolve the Reynolds stress tensor from six to two.

$$\textbf{(76)} \quad -\rho\overline{u_i' u_j'} = \mu_T\left(\frac{\partial U_i}{\partial x_j}+\frac{\partial U_j}{\partial x_i}\right)-\frac{2}{3}\delta_{ij}\left(\mu_T\frac{\partial U_k}{\partial x_k}+\rho k\right)$$

Equation (76) requires resolution of the eddy viscosity and turbulent kinetic energy in order to solve the Reynolds averaged Navier-Stokes equations. The turbulent energy flux may be approximated using the turbulent Prandtl number and the Reynolds analogy, given by the following relation.

$$\textbf{(77)} \quad -\rho\overline{u_j'\theta_T'} \cong \frac{\mu_T}{\mathrm{Pr}_T}\frac{\partial \theta_T}{\partial x_j}$$

The turbulent Prandtl number, Pr_T, is the ratio of the momentum eddy diffusivity and the heat transfer eddy diffusivity and is equal to 0.9 for this application of the Reynolds averaged Navier-Stokes equations [Krist *et al.*, 1998]. The selection of a turbulence model is somewhat dependant on the flow phenomena for a given problem. Due to the uniqueness of the problem presented in this research, several turbulence models are investigated.

3.4.4.1 Abid k-Epsilon Model

The k-ε turbulence model is built on two transport variables: the turbulent kinetic energy, *k*, and turbulent dissipation, ε, allowing for convection and diffusion of turbulent energy to be modeled. The Abid k-Epsilon turbulence model can is described by the following relationship for the eddy viscosity.

(78) $$\mu_T = \rho C_\mu f_\mu \frac{k^2}{\varepsilon}$$

The turbulence kinetic energy is defined by the following relation.

(79) $$\rho \frac{\partial k}{\partial t} + \rho u_j \frac{\partial k}{\partial x_j} = P_k \left(\frac{M_\infty}{\mathrm{Re}} \right) - \rho \varepsilon \left(\frac{M_\infty}{\mathrm{Re}} \right) + \frac{\partial}{\partial x_j} \left[(\mu + \mu_T / \sigma_k) \frac{\partial k}{\partial x_j} \right] \left(\frac{M_\infty}{\mathrm{Re}} \right)$$

The turbulent dissipation rate is then described below.

(80) $$\rho \frac{\partial \varepsilon}{\partial t} + \rho u_j \frac{\partial \varepsilon}{\partial x_j} = P_\varepsilon \left(\frac{M_\infty}{\mathrm{Re}} \right) - C_{\varepsilon_2} \rho \frac{\varepsilon^2}{k} f_2 \left(\frac{M_\infty}{\mathrm{Re}} \right) + \frac{\partial}{\partial x_j} \left[(\mu + \mu_T / \sigma_\varepsilon) \frac{\partial \varepsilon}{\partial x_j} \right] \left(\frac{M_\infty}{\mathrm{Re}} \right)$$

The production terms from equations (79) and (80) are defined by the following relations.

(81) $$P_k = \mu_T \Omega^2 \qquad P_\varepsilon = C_{\varepsilon_1} \frac{\varepsilon}{k} \mu_T \Omega^2$$

The turbulence model coefficients required by the Abid k-Epsilon turbulence model are described below.

(82) $$C_{\varepsilon 1} = 1.45, \quad C_{\varepsilon 2} = 1.83, \quad C_\mu = 0.09, \quad \sigma_k = 1.0 \quad \sigma_\varepsilon = 1.4$$

3.4.4.2 Spalart-Allmaras Model

The Spalart-Allmaras turbulence model solves the eddy viscosity through a single field equation, described below.

(83) $$\mu_T = \rho \hat{v} f_{v_1}.$$

The term $\hat{v}$ is the variable in the following field equation.

(84)
$$\frac{\partial \hat{v}}{\partial t}+u_j\frac{\partial \hat{v}}{\partial x_j}=C_{b_1}\left(1-f_{t_2}\right)\Omega\hat{v}+\frac{M_\infty}{\mathrm{Re}}\left[C_{b_1}\left(\left(1-f_{t_2}\right)f_{v_2}+f_{t_2}\right)\frac{1}{\kappa^2}-C_{w_1}f_w\right]\left(\frac{v}{d}\right)^2$$
$$-\frac{M_\infty}{\mathrm{Re}}\frac{C_{b_2}}{\sigma}\hat{v}\frac{\partial^2\hat{v}}{\partial x^2}+\frac{M_\infty}{\mathrm{Re}}\frac{1}{\sigma}\frac{\partial}{\partial x_j}\left[\left(\hat{v}+\left(1+C_{b_2}\right)\hat{v}\right)\frac{\partial \hat{v}}{\partial x_j}\right]$$

The mean strain rate and mean vorticity tensors are given by the following relations.

(85) $$S_{ij}=\frac{1}{2}\left(\frac{\partial u_i}{\partial x_j}+\frac{\partial u_j}{\partial x_i}\right)\qquad W_{ij}=\frac{1}{2}\left(\frac{\partial u_i}{\partial x_j}-\frac{\partial u_j}{\partial x_i}\right)$$

The factors and associated coefficients are defined in equations (86) and (87) respectively.

(86)
$$f_{v_1}=\frac{\left(\hat{v}/v\right)^3}{\left(\hat{v}/v\right)^3+C_{v_1}^3}\qquad f_{t_2}=C_{t_3}\exp\left(-C_{t_4}\left(\frac{\hat{v}}{v}\right)^2\right)\qquad f_w=g\left[\frac{1+C_{w_3}^6}{g^6+C_{w_3}^6}\right]^{\frac{1}{6}}$$
$$g=r+C_{w_2}\left(r^6-r\right)\qquad r=\frac{\hat{v}}{\hat{S}\left(\frac{\mathrm{Re}}{M_\infty}\right)\kappa^2 d^2}\qquad \hat{S}=\Omega+\frac{\hat{v}f_{v_2}}{\left(\frac{\mathrm{Re}}{M_\infty}\right)\kappa^2 d^2}$$
$$f_{v_2}=1-\frac{\hat{v}/v}{1+\left(\hat{v}/v\right)f_{v_1}}\qquad \Omega=\sqrt{2W_{ij}W_{ij}}$$

(87)
$$C_{b_1}=0.1355\qquad \sigma=\frac{2}{3}\qquad C_{b_2}=0.622\qquad \kappa=0.41\qquad C_{w_2}=0.3$$
$$C_{w_3}=2.0\qquad C_{v_1}=7.1\qquad C_{t_3}=1.2\qquad C_{t_4}=0.5\qquad C_{w_1}=\frac{C_{b_1}}{\kappa^2}+\frac{1+C_{b_2}}{\sigma},$$

The term *d* is defined as the distance to the closest wall.

3.4.4.3 Wilcox k-Omega Model

The Wilcox k-Omega turbulence model uses two transport equations, one describing the turbulent kinetic energy and one relating the turbulent vorticity magnitude.

(88) $$\frac{\partial k}{\partial t}+u_j\frac{\partial k}{\partial x_j}=\frac{1}{\rho}P_k\left(\frac{M_\infty}{\mathrm{Re}}\right)-\beta' k\omega\left(\frac{\mathrm{Re}}{M_\infty}\right)+\frac{1}{\rho}\frac{\partial}{\partial x_j}\left[\left(\mu+\frac{\mu_T}{\sigma_k}\right)\frac{\partial k}{\partial x_j}\right]\left(\frac{M_\infty}{\mathrm{Re}}\right)$$

(89) $$\frac{\partial \omega}{\partial t}+u_j\frac{\partial \omega}{\partial x_j}=\frac{1}{\rho}P_\omega\left(\frac{M_\infty}{\mathrm{Re}}\right)-\beta\omega^2\left(\frac{\mathrm{Re}}{M_\infty}\right)+\frac{1}{\rho}\frac{\partial}{\partial x_j}\left[\left(\mu+\frac{\mu_T}{\sigma_\omega}\right)\frac{\partial \omega}{\partial x_j}\right]\left(\frac{M_\infty}{\mathrm{Re}}\right)$$

The eddy viscosity is then related to the turbulent kinetic energy and turbulent vorticity magnitude by the following relation.

(90) $$\mu_T=\frac{\rho k}{\omega}$$

The production terms from equations (88) and (89) are given below.

(91) $$P_k=\mu_T\Omega^2 \qquad P_\omega=\gamma\rho\Omega^2$$

The coefficients are then defined by the following relations.

(92) $$\gamma=\frac{\beta}{C_\mu}-\frac{\kappa^2}{\sigma_\omega\sqrt{C_\mu}} \qquad \beta'=C_\mu=0.09 \qquad \beta=0.075$$
$$\sigma_k=\frac{1}{0.5} \qquad \sigma_\omega=\frac{1}{0.5} \qquad \kappa=0.41$$

3.4.4.4 Menter's k-Omega SST Model

The Menter k-Omega Shear Stress Transport (SST) turbulence model uses two transport equations, where the near wall region uses a k-Omega formulation and the far wall region uses a k-Epsilon formulation. A blending function is used to transition between the formulations. The turbulent kinetic energy and the turbulent vorticity magnitude are given by the following relationships.

(93) $$\frac{\partial k}{\partial t}+u_j\frac{\partial k}{\partial x_j}=\frac{1}{\rho}P_k\left(\frac{M_\infty}{\mathrm{Re}}\right)-\beta' k\omega\left(\frac{\mathrm{Re}}{M_\infty}\right)+\frac{1}{\rho}\frac{\partial}{\partial x_j}\left[\left(\mu+\frac{\mu_T}{\sigma_k}\right)\frac{\partial k}{\partial x_j}\right]\left(\frac{M_\infty}{\mathrm{Re}}\right)$$

(94) $$\frac{\partial \omega}{\partial t}+u_j\frac{\partial \omega}{\partial x_j}=\frac{1}{\rho}P_\omega\left(\frac{M_\infty}{\mathrm{Re}}\right)-\beta\omega^2\left(\frac{\mathrm{Re}}{M_\infty}\right)+\frac{1}{\rho}\frac{\partial}{\partial x_j}\left[\left(\mu+\frac{\mu_T}{\sigma_\omega}\right)\frac{\partial \omega}{\partial x_j}\right]\left(\frac{M_\infty}{\mathrm{Re}}\right)$$
$$+2(1-F_1)\frac{1}{\sigma_{\omega_2}\omega}\frac{\partial k}{\partial x_j}\frac{\partial \omega}{\partial x_j}\left(\frac{M_\infty}{\mathrm{Re}}\right)$$

The eddy viscosity is then related to the turbulent kinetic energy and turbulent vorticity magnitude by the following function.

(95) $$\mu_T = \min\left[\frac{\rho k}{\omega}, \frac{a_1 \rho k}{\Omega F_2}\left(\frac{\mathrm{Re}}{M_\infty}\right)\right]$$

The production terms from equations (93) and (94) are defined below.

(96) $$P_k = \mu_T \Omega^2 \qquad P_\omega = \gamma \rho \Omega^2$$

The set of constants are calculated from the sets ϕ_1 and ϕ_2, where the sets are related by the following blending relationship.

(97) $$\phi = F_1 \phi_1 + (1 - F_1)\phi_2$$

The constants are then defined by the following relations.

(98) $$\begin{array}{cc}
\phi_1 : & \phi_2 : \\
\gamma_1 = \dfrac{\beta_1}{C_\mu} - \dfrac{\kappa^2}{\sigma_{w_1}\sqrt{C_\mu}} & \gamma_2 = \dfrac{\beta_2}{C_\mu} - \dfrac{\kappa^2}{\sigma_{w_2}\sqrt{C_\mu}} \\
\sigma_{k_1} = 1/0.85 & \sigma_{k_2} = 1.0 \\
\sigma_{w_1} = 1/0.5 & \sigma_{w_2} = 1/0.856 \\
\beta_1 = 0.075 & \beta_2 = 0.0828
\end{array}$$

(99) $$\begin{array}{l}
\kappa = 0.41 \qquad a_1 = 0.31 \qquad \beta' = C_\mu = 0.09 \\
F_1 = \tanh\left(\Gamma^4\right) \qquad \Gamma = \min\left[\max\left(\Gamma_1, \Gamma_3\right), \Gamma_2\right] \\
\Gamma_1 = \dfrac{500 v}{d^2 \omega}\left(\dfrac{M_\infty}{\mathrm{Re}}\right)^2 \qquad \Gamma_2 = \dfrac{4 \rho k}{d^2 \sigma_{\omega_2}\left(CD_{k-\omega}\right)} \qquad \Gamma_3 = \dfrac{\sqrt{k}}{C_\mu \omega d}\left(\dfrac{M_\infty}{\mathrm{Re}}\right) \\
CD_{k-\omega} = \max\left(\rho \dfrac{2}{\sigma_{\omega_2} \omega} \dfrac{\partial k}{\partial x_j} \dfrac{\partial \omega}{\partial x_j}, 10^{-20}\right) \qquad F_2 = \tanh\left(\Pi^2\right) \qquad \Pi = \max\left(2\Gamma_3, \Gamma_1\right)
\end{array}$$

Again, the term *d* is defined as the distance to the closest wall.

CHAPTER 4

VALIDATION AND VERIFICATION

Validation studies are performed to compare the analytical models presented in this research to experimental data in order to determine the model prediction fitness, and the appropriate grid density and turbulence model for CFD. The first validation study compares the prescribed vortex wake model used to predict the rotor aerodynamics in hover to the benchmark experimental study performed by Caradonna and Tung (1981). The second validation study compares a CFD model of an ejector flow in two dimensions against an experimental study performed by Gilbert and Hill (1973). The final validation study compares a three-dimensional CFD model of a hovering rotor, again, to the experimental study performed by Caradonna and Tung (1981).

The CFD tool used in this study is CFL3D; a Reynolds-Averaged thin-layer Navier-Stokes multi-block flow solver for structured grids with parallel processing capabilities. A semi-discrete finite-volume approach is used for spatial discretization, with up-wind biasing for convective and pressure terms. A central differencing approach is implemented for shear stress terms, and implicit time advancement is used for steady and unsteady flows. A handful of turbulence models are included, ranging from zero-equation to two-equation [Krist *et al*., 1998]. Multigrid convergence acceleration is also available; requiring grid dimensions such that when every other grid point is removed, the dimensions still maintain an integer value.

The first validation study is carried out to adjust the blade element, prescribed vortex wake model parameters to achieve a good prediction for the thrust and power generated by the rotor. The second validation study allows for fine tuning the CFD model parameters for ejector flows in two dimensions. The third validation study is conducted to determine the CFD model parameters and grid topology for a three-dimensional model of a hovering rotor.

4.1 Blade Element Rotor Aerodynamic Model

The experimental study selected to compare the blade element, prescribed vortex wake rotor aerodynamic model was performed by Caradonna and Tung (1981). Chord-wise pressure measurements were made at several radial locations. The pressure data were then integrated to give the radial load distribution. From the load distribution, the rotor thrust was computed by integrating along the radial direction. A blade element rotor aerodynamic formulation cannot predict the pressure distributions over a rotor blade surface. However, lift and drag are available through empirical coefficients that are dependent on the airfoil shape, angle of attack, free stream Mach number, and Reynolds number.

4.1.1 Rotor Definition and Model Parameters

The rotor considered in this validation study has a low aspect ratio and rigid blades. The blade planform contains no twist or taper distributions and a NACA series, 12% thick, symmetric airfoil. There are several operating speeds and collective pitch angles available. The highest collective pitch angle and a moderate tip speed are selected for comparison. The basic model rotor parameters are presented in Table 1.

Table 1: Model Rotor Definition

Radius (ft)	3.75
Mean Chord (ft)	0.5
Root Cutout (ft)	0.75
Number of Blades	2
Rotor RPM	1250
Tip Speed (ft/s)	491
Collective (deg)	12
Twist	None
Taper	None
Airfoil	NACA 0012

There are several parameters that may be adjusted within the blade element, prescribed vortex wake rotor model to achieve the desired results. The first parameter is the number of elements along the radial direction of the blade. This controls the coarseness of the radial integration of lift and drag for the associated rotor thrust and power. It is desirable to have a large number of blade elements; however, the computational time increases along with the number of elements. The second model parameter is the number of wake increments between the trailing edge of the blade and the end of the rotor wake structure. In general, the more wake points that are available, the better the model approximates a hovering rotor. The third model parameter is the maximum age of the wake, which determines the end of the rotor wake structure. The contribution to the induced velocity at the rotor blade from the vortex filament is inversely proportional to the square of its distance to the blade. Therefore, the effects of increasing the maximum age after 10 rotations of the rotor will be small. The final model parameter is the wake contraction coefficient. This parameter has the greatest effect on the radial load distribution, most notably over the blade tip region. A summary of the parameters used in the blade element, prescribed vortex wake rotor model is presented in Table 2.

Table 2: Rotor Aerodynamic Model Parameters

Number of Blade Elements	60
Number of Vortex Wake Filaments	220
Maximum Wake Age (Degrees)	3600
Wake Contraction Coefficient	0.87

4.1.2 Rotor Aerodynamic Model Validation

The radial load distribution provides a good comparison benchmark for a hovering rotor and is shown in Figure 21. The non-uniform trend in the radial load distribution predicted by the blade element, prescribed vortex wake rotor model shows good agreement to the experimental data. The thrust produced by the rotor, determined by integrating the lift along the radial direction of the blade, is compared to the experimental value in Table 3 in coefficient form. The power consumed by the rotor is not available from the experimental study. However, the predicted value is presented in Table 3 for completeness. Tung *et al*. (1981) analytically computed the rotor thrust and power, which is also tabulated for comparative purposes. The thrust predicted by the blade element, prescribed vortex wake rotor model shows good agreement to the experimental value and to the analytical predictions made by the lifting surface formulation used by Tung *et al*. (1981).

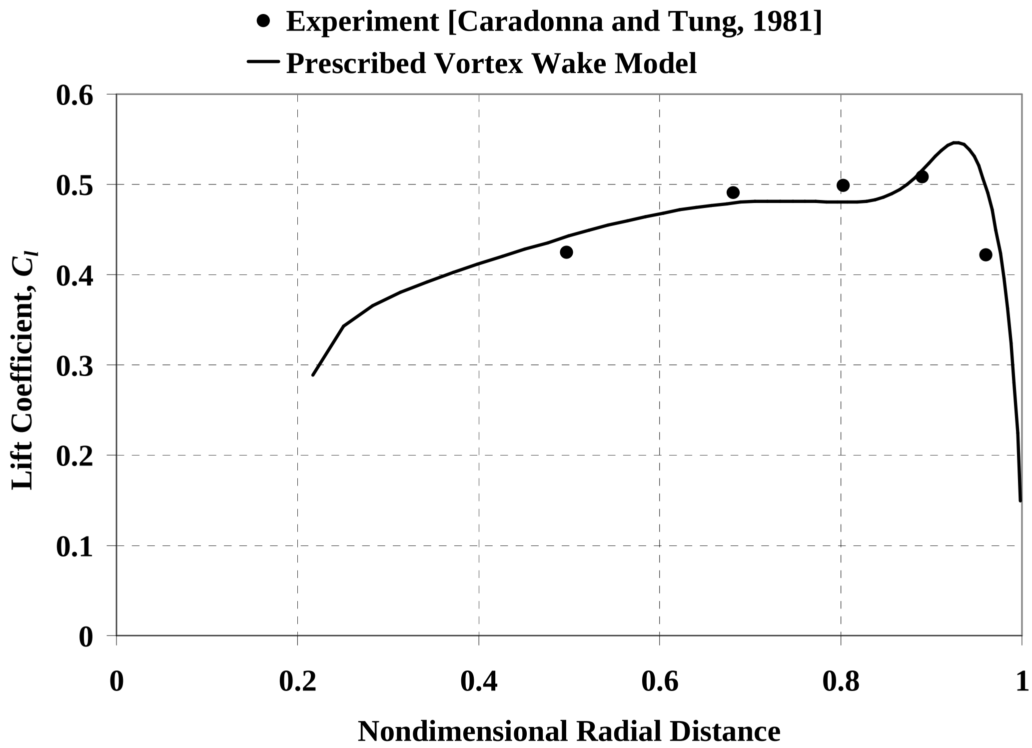

Figure 21: Radial Lift Coefficient Distribution Comparison

Table 3: Rotor Thrust Comparison

	C_T	C_P
Experiment [Caradonna and Tung, 1981]	7.90E-03	-
Prescribed Vortex Wake Model	8.14E-03	1.05E-03
Analytical Model [Tung *et al*., 1981]	8.30E-03	9.58E-04
Error (%)	3.04%	-

4.1.3 Conclusion

Overall, the blade element, prescribed vortex wake rotor aerodynamic model shows good agreement the experimental study conducted by Caradonna and Tung (1981). While this rotor aerodynamic formulation cannot capture the full physics of the rotary wing ejector, it is well suited for first order calculations. Appropriate corrections to the empirical lift and drag coefficients are required to account for the geometry and high speed exhaust flow of the ejector nozzle.

4.2 Two-Dimensional Ejector Flow

The ejector experiment selected to correlate the two-dimensional CFD model was conducted by Gilbert and Hill (1973). The ejector configuration includes a high aspect ratio rectangular nozzle enclosed by a duct with a bell mouth inlet and exhaust diffuser. This experimental ejector study is selected for the large volume of data available, especially traverse data in the mixing section. Two-dimensional approximations can be made with the turbulent shear layer being the primary mechanism for the mixing of the high speed flow and low speed flow within the ejector. Additionally, the flow is assumed to be steady-state. Several turbulence models are applied to determine which is appropriate; including: k-Epsilon, Spalart-Allmaras, k-Omega, and Menter SST.

4.2.1 Computational Grid and Boundary Conditions

The computational grid is generated using Gridgen® and is presented in Figure 22, with every fourth point shown for clarity. The grid contains 93,144 nodes, with 60,258 nodes used for the mixing section. The grid is split into four blocks; with the first two blocks assigned as the upper and lower inlet sections up to the primary nozzle exhaust. The third block is the convergent nozzle and the fourth block contains the mixing section, from the primary nozzle discharge to the ejector outlet. Each block is multigridable to four coarseness levels to accelerate model convergence. Additionally, the blocks are split into smaller equal sized blocks to take advantage of parallel processing.

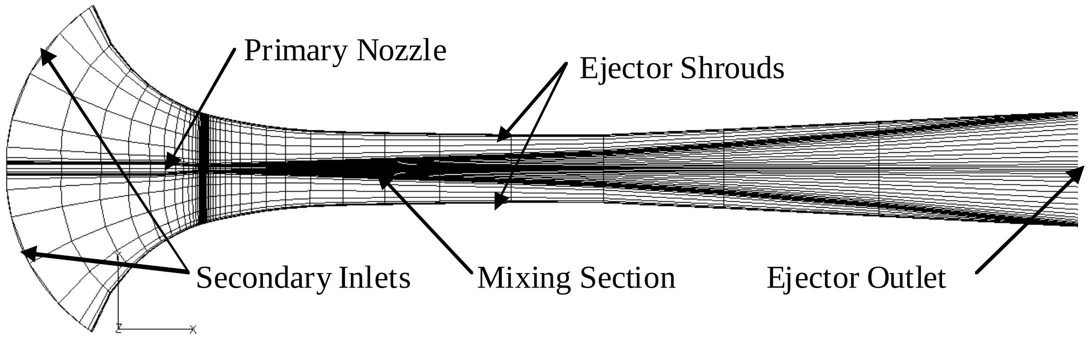

Figure 22: Two-Dimensional Ejector Grid

The high speed flow exhausting from the nozzle will draw the ambient air into the ejector. This fluid entrainment results in a positive flow at the entrance of the bell mouth. The boundary condition at this location is assumed to be an inflow. The ejector exhaust pressure ratio is subsequently adjusted to match the measured mass flow rate. The walls are assumed to be adiabatic with the no-slip condition. Additionally, the ejector is not moving with respect to the ambient air. Therefore, the secondary inlet flow conditions are equal to the static values. A summary of the values for the inflow and outflow boundary conditions are presented in Table 4.

Table 4: Two-Dimensional Ejector Boundary Conditions

	P/P_∞	T/T_∞	P_∞ (lb/ft^2)	T_∞ (R)
Inlet	1.00	1.00	2131.20	547.00
Nozzle	2.42	1.19	2131.20	547.00
Outlet	1.06	1.00	2131.20	547.00

4.2.2 Two-Dimensional Model Validation

The experiment conducted by Gilbert and Hill (1973) produced a large amount of data for the ejector nozzle. The data used for correlation purposes includes the mass flow rates, velocity traverse data, and the shroud wall pressure distribution. The grid convergence for this model is determined by comparing the mass flow rate at the ejector exit plane for varying grid coarseness levels. A comparison of the mass flow rate computed on multiple grid levels is presented in Table 5 using Menter's SST turbulence model.

Table 5: Mass Flow Rate Comparison

	Experimental Mass Flow Rate (lb/s)	Computed Mass Flow Rate (lb/s)				% Error
		Coarse Grid	Medium Grid	Fine Grid	Richardson Extrapolation	
Inlet	2.77	3.17	2.74	2.74	2.74	0.85%
Nozzle	0.71	0.72	0.72	0.72	0.72	-1.42%
Outlet	3.47	3.89	3.45	3.45	3.45	0.52%

Table 5 shows a very good agreement between the experimental and computed ejector mass flow rates, indicating that the fluid entrainment process is captured. Both the extrapolated and fine grid mass flow rates are within ±1% of the experimental values, indicating good grid convergence.

Gilbert and Hill (1973) estimated an uncertainty in the exit mass flow rate calculations upwards of ±4%. The error computed in Table 5 is well within that range. They reported an error in the mass flow rate of the primary nozzle of ±1%, with an estimated increase in nozzle area of 0.33% when pressurized. The error in the primary mass flow rate is slightly over the experimental error. This could be easily resolved through a small increase in the nozzle throat area; achieved by thinning the nozzle walls to account for the increase in nozzle area under pressure.

The experimental velocity profile data was calculated through the isentropic relations for compressible flows from the measured static and stagnation pressure and the stagnation temperature. Since the mass flow rate is computed from the traverse data, the associated uncertainty is assumed to be derived directly from the transverse data measurements [Gilbert and Hill, 1973]. For brevity, the velocity profile comparisons are only shown for two traverse positions downstream of the nozzle. Figure 23 shows the velocity profile at 3 inches downstream of the primary nozzle and Figure 24 shows the velocity profile at 10.5 inches downstream of the primary nozzle.

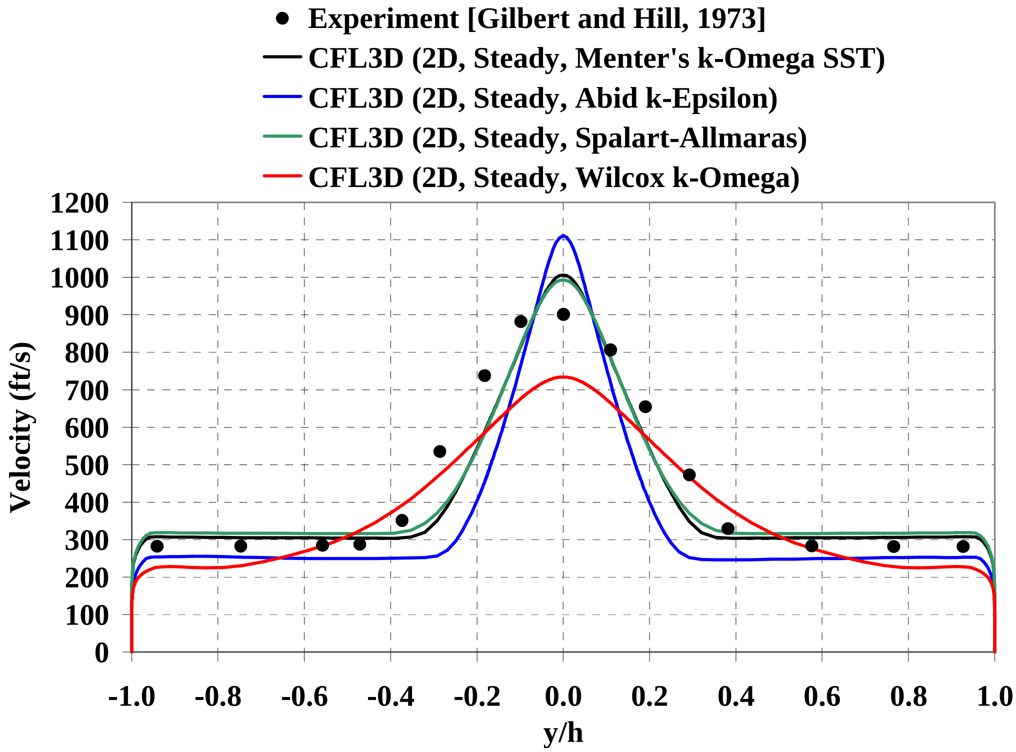

Figure 23: Velocity Profiles 3 Inches Downstream of the Primary Nozzle

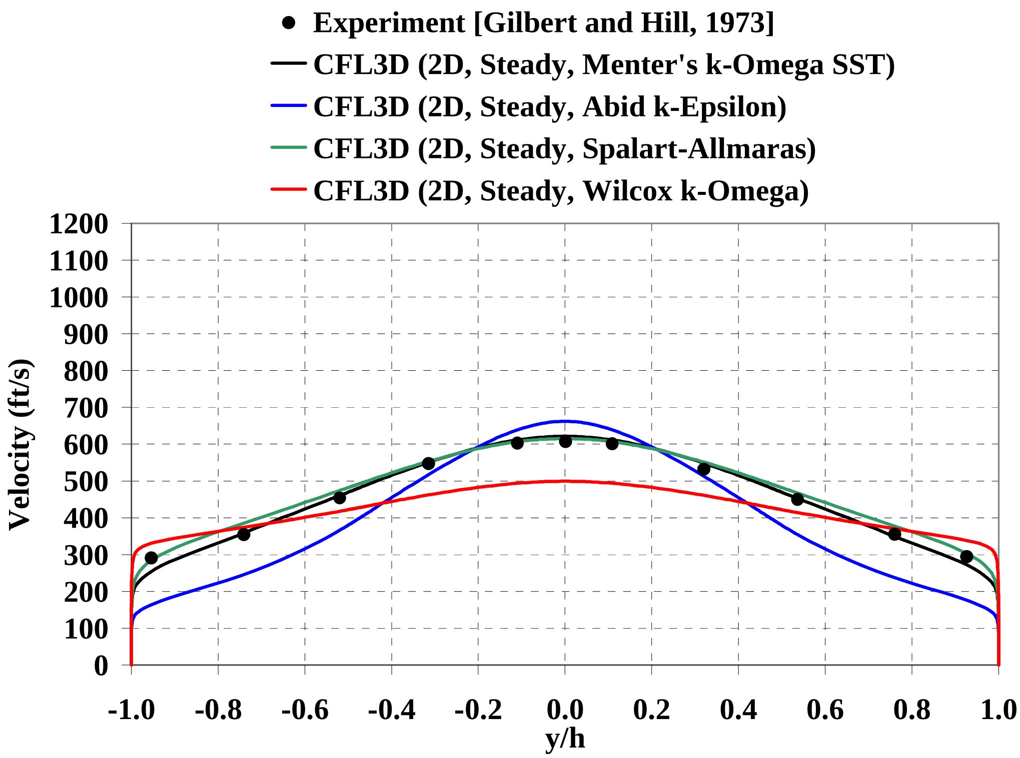

Figure 24: Velocity Profiles 10.5 Inches Downstream of the Primary Nozzle

It is apparent from Figure 23 and Figure 24 that the trends in the velocity profiles are captured. Menter's SST and Spalart-Allmaras both show good agreement with the experimental data. Abid k-Epsilon under-predicts the mixing between the high speed and low speed flows, indicated by the high peak and low spread in the velocity profiles. Wilcox k-Omega, on the other hand, over-predicts the mixing compared to the experimental data, indicated by the low peak and high spread in the velocity profiles.

The static pressure was measured through pressure ports along the shroud wall, downstream of the nozzle. There is only a small error associated with this experimental data, amounting to approximately 0.4% [Gilbert and Hill, 1973]. Figure 25 shows the comparison of the shroud wall static pressure between the experiment and the CFD model. The static pressure trend is captured by each of the turbulence models, resulting in good correlation for this aspect of the modeling.

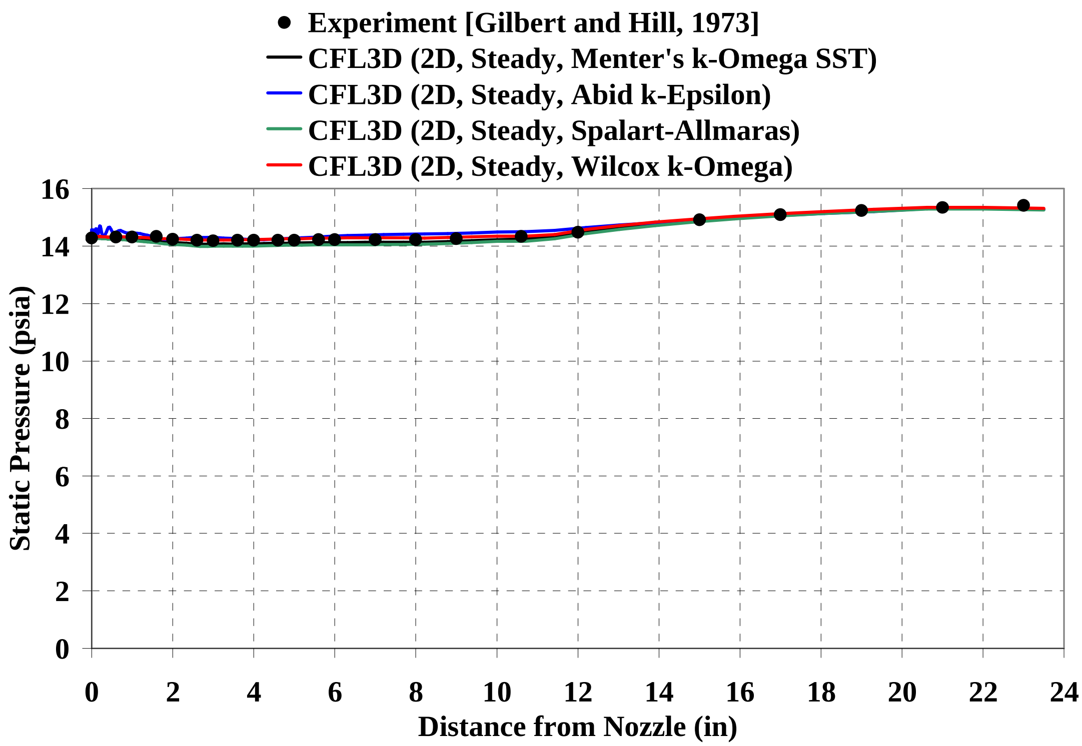

Figure 25: Shroud Wall Static Pressure Comparison

4.2.3 Conclusion

Overall, the CFD model of this ejector shows promise. Based on the results, the Spalart-Allmaras and Menter k-Omega SST turbulence models give better overall prediction of the two-dimensional ejector flow compared to the other turbulence models tested. Spalart-Allmaras is a one equation turbulence model while Menter’s k-Omega SST is a two equation turbulence model. Spalart-Allmaras requires the least computer resources between the two turbulence models and is selected for all of the subsequent CFD modeling of ejector flows.

4.3 Hovering Rotor

The experimental study selected to correlate a computational model of a hovering rotor was performed by Caradonna and Tung (1981). This test serves as an excellent benchmark and includes the rotor thrust, span-wise loading, blade surface pressure, and rotor wake data. Data for a variety of rotor tip speeds and blade collective pitch angles are available in this experimental study. However, the conditions selected for the previous comparison are repeated for consistency.

4.3.1 Computational Grid and Boundary Conditions

The computational grid is generated using Gridgen®. The grid is a structured, body fitted, C-H type grid with ξ (i) aligned to the blade radial direction, η (j) aligned along the chord-wise direction, and ζ (k) aligned in the viscous direction normal to the surface, as shown in Figure 26. The computational grid is generated for one rotor blade and contains 24,606,063 points, shown in Figure 27. The boundary conditions for this problem, shown in Figure 27, consist of extrapolation, inflow/outflow, viscous wall, singularity, and periodic. An extrapolation boundary condition is assigned to the inside vertical grid boundaries surrounding the axis of rotation. Inflow/outflow boundaries are located around the outside far-field, and the viscous wall boundary conditions are applied to the rotor blade surface. The grid block protruding in the radial direction away from the blade tip contains two grid singularities that require the singularity boundary condition. Periodic boundary conditions are assigned to the grid faces perpendicular to the rotor blade at the half cylindrical domain cut. The model rotor parameters the computational grid is based on are presented in Table 6.

Rotor wake trajectory data are used to cluster the grid points trailing from the rotor blade. This practice provides reduced numerical dissipation of the tip vortex, improving the overall accuracy of the model, when the data are available. The blocked C-grid arrangement surrounding the rotor blade is presented in Figure 28. The blade tip grid treatment in presented in Figure 29, consisting of two poles at the leading and trailing edge. This creates a sharp cornered blade tip, requiring an additional block that protrudes from the blade tip to the far-field.

The model employs an unsteady formulation with the grid rotating at a constant rate, stepping incrementally by one tenth of one degree for each time step. Five sub-iterations are used for the dual time stepping method to achieve second order temporal accuracy. The Spalart-Allmaras turbulence model is selected, primarily to reduce the computational cost and to improve model stability.

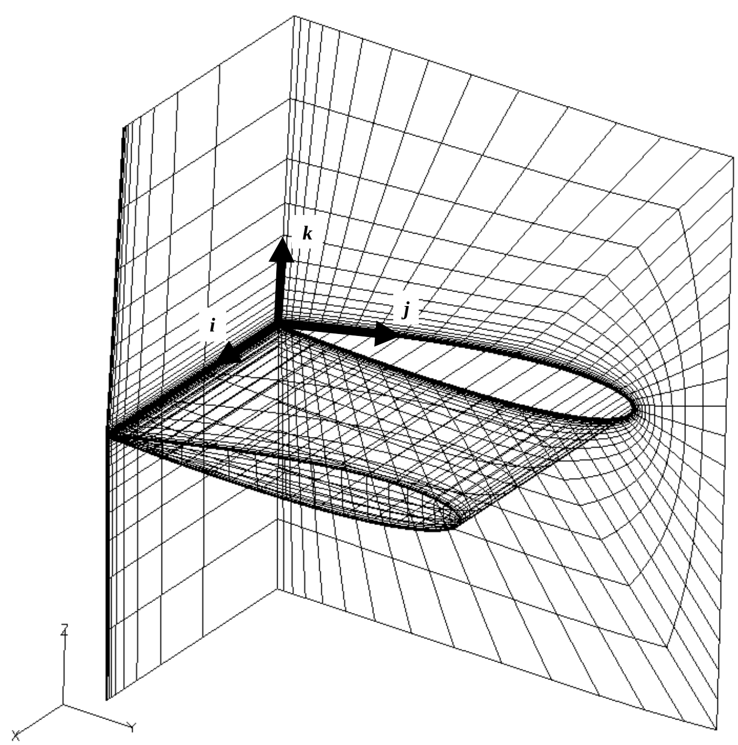

Figure 26: Three-Dimensional Rotor Computational Grid Orientation

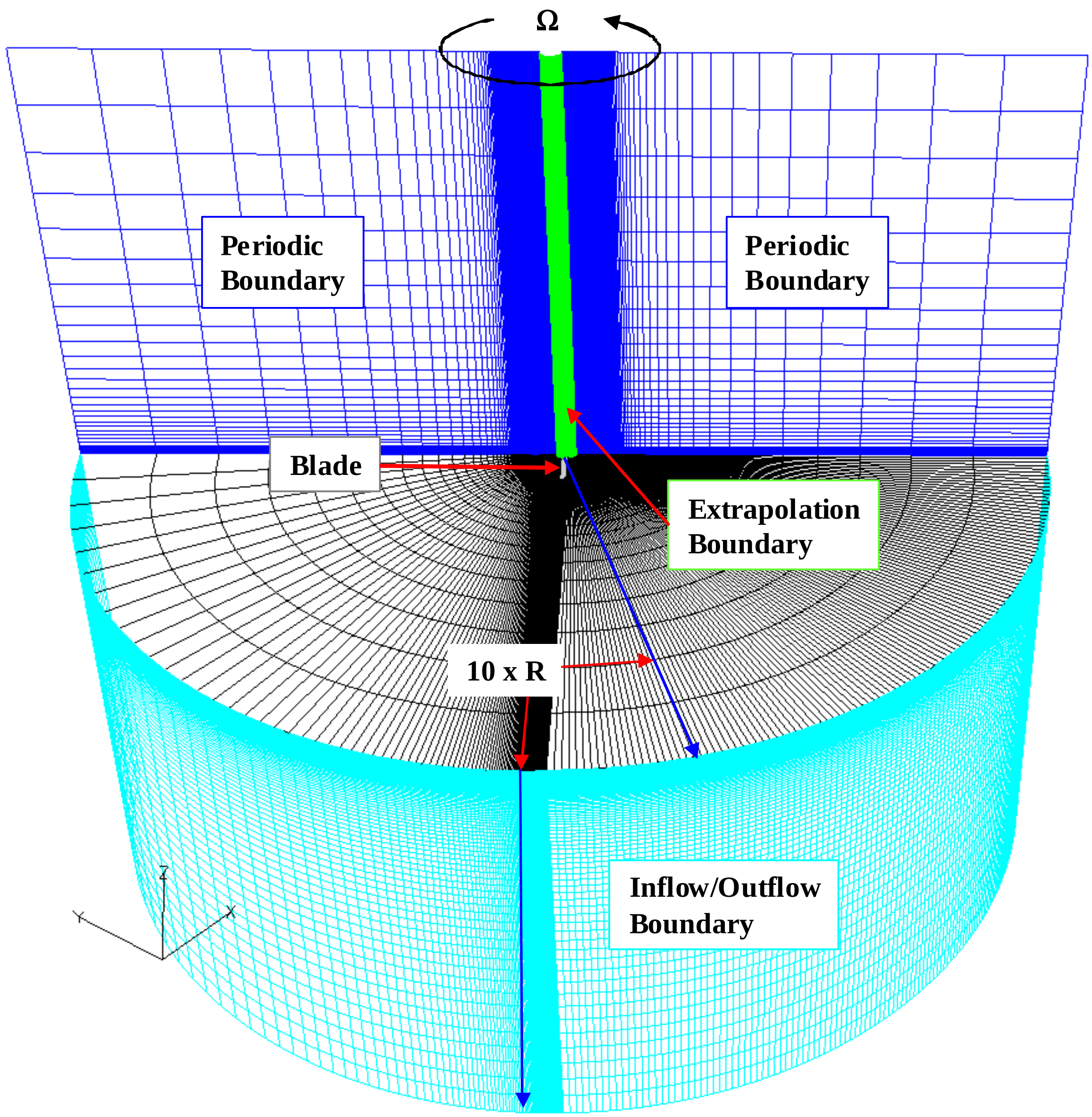

Figure 27: Three-Dimensional Rotor Computational Grid Domain

Table 6: Three-Dimensional CFD Model Rotor Parameters

Radius (ft)	3.75
Mean Chord (ft)	0.5
Root Cutout (ft)	0.75
Rotor RPM	1250
Collective (deg)	12
Temperature (R)	519

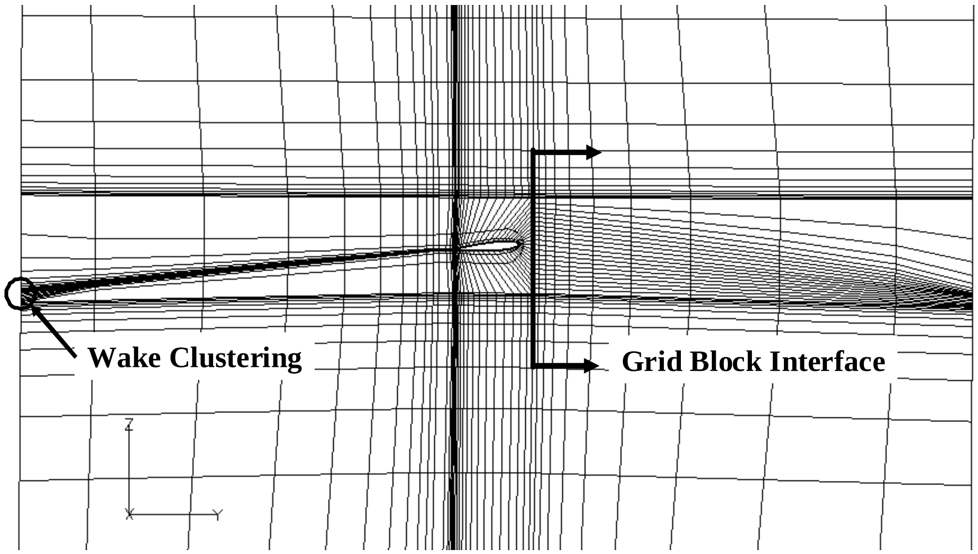

Figure 28: Near-Rotor Blocked C-Grid Arrangement

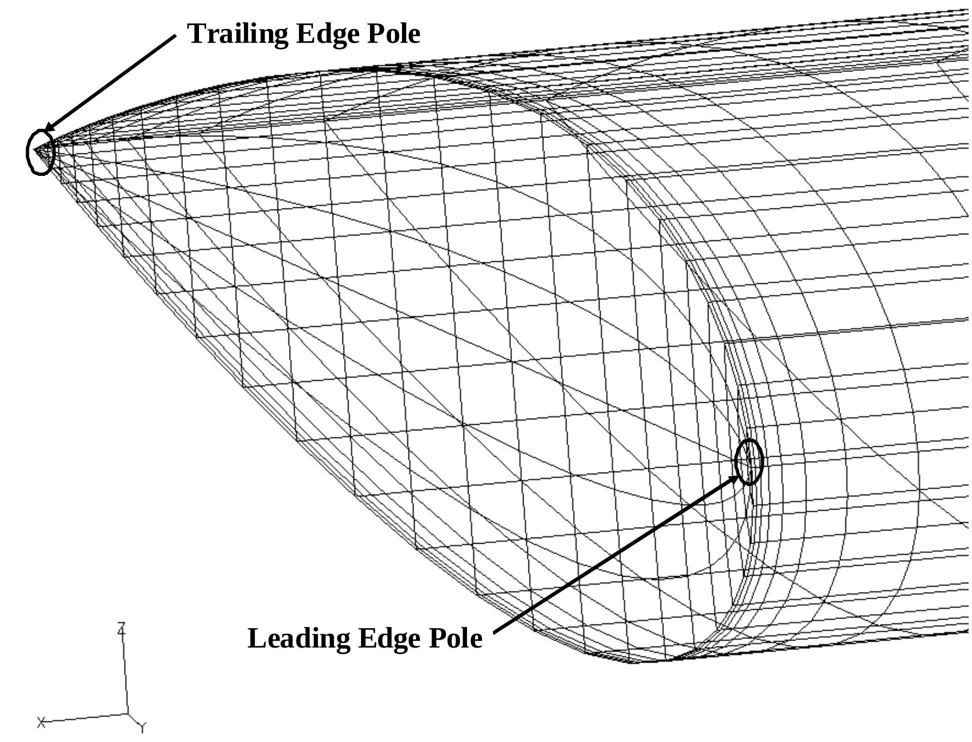

Figure 29: Rotor Blade Tip Grid Treatment

4.3.2 Rotor Model Validation

The experiment conducted by Caradonna and Tung (1981) produced a large amount of surface pressure and rotor wake data for a range of rotor speeds and collective pitch angles. The primary data set provided from the experiment, used for CFD model correlation, is the surface pressure; which is then integrated in the chord-wise direction at several radial locations to give the blade loading distribution. The overall convergence of the CFD model is determined by the change in the mean drag value over time. The model, distributed over 32 processors, is run for 54,000 time steps; representing 15 full rotations of the blade. The total wall time for the simulation, including three grid coarseness levels, is 617 hours, 12 minutes, and 26 seconds. The mean drag coefficient history is presented in Figure 30, showing damped oscillatory behavior over the first two thirds and then stabilizing over the final third to a value of 0.117. The mean drag coefficient over the three grid coarseness levels is used to asymptotically extrapolate the infinitely fine grid solution. Table 7 shows that the change between the three grid coarseness levels is relatively small, which indicates good grid convergence.

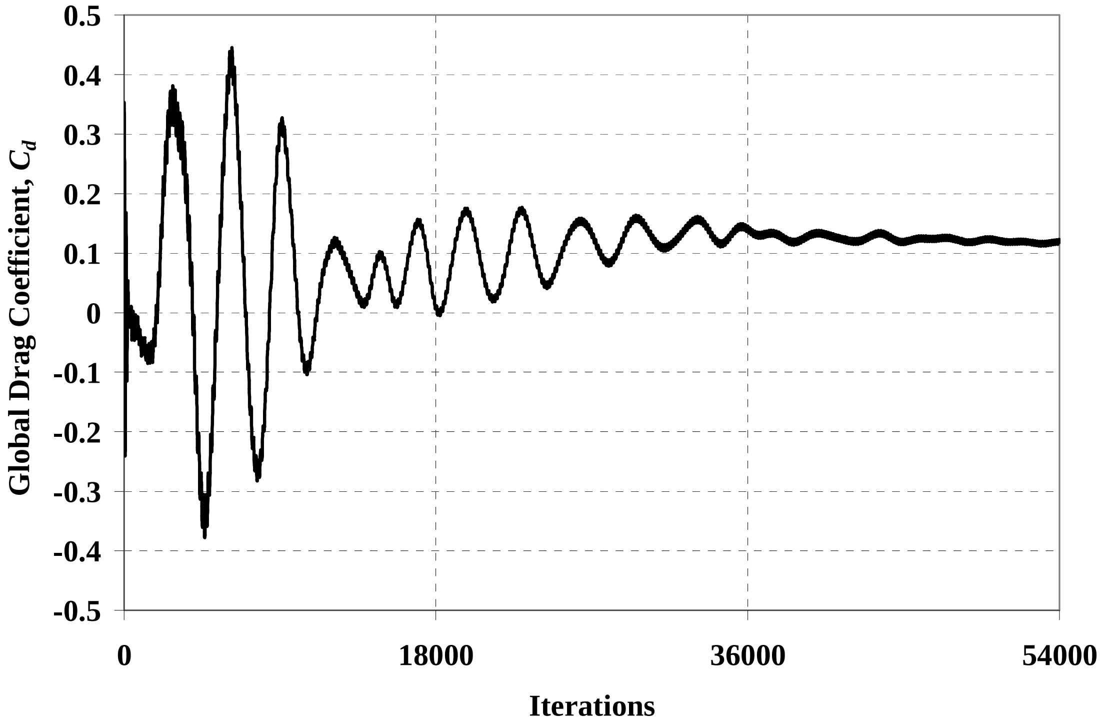

Figure 30: Three-Dimensional Rotor CFD Model Global Drag Convergence History

Table 7: Three-Dimensional Rotor CFD Model Mean Drag Grid Convergence

	Number of Grid Points	Mean Drag Coefficient, C_d
Coarse Grid	6,151,517	0.1300
Medium Grid	12,303,032	0.1170
Fine Grid	24,606,063	0.1174
Richardson Extrapolation	-	0.1175

The wake generated by the hovering rotor is visualized in terms of contours of constant Mach number and presented in Figure 31. The tip vortex shows a large degree of dissipation after it reaches one revolution. Refining the grid in the wake region should improve these results.

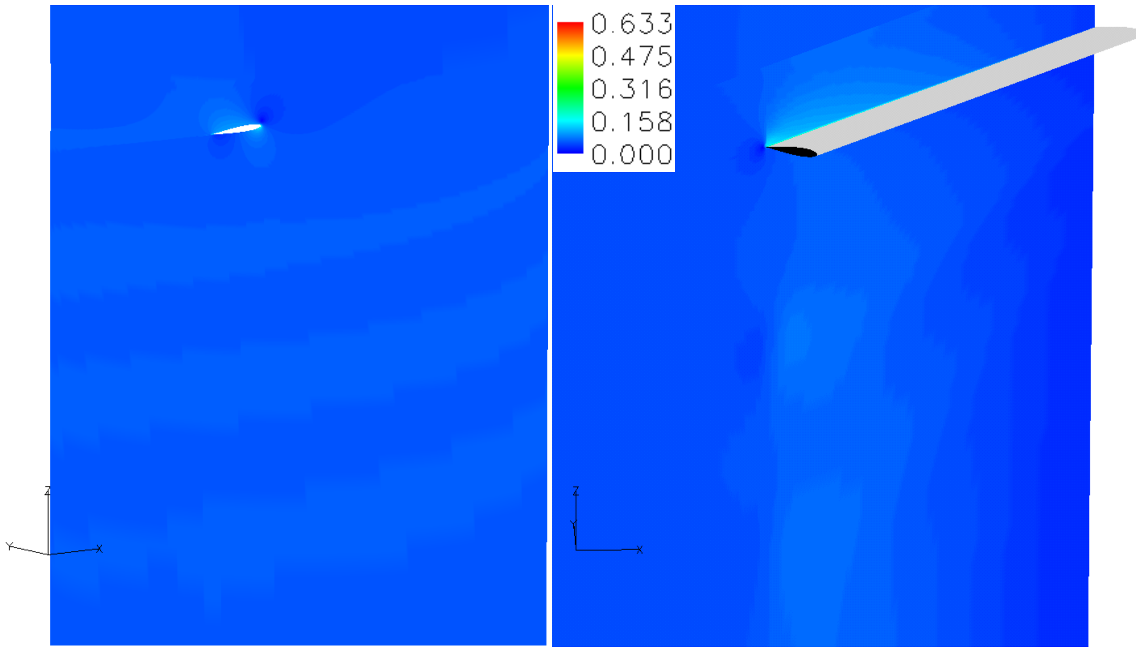

Figure 31: Flow Field Contours of Constant Mach Number

The chord-wise pressure distributions are extracted from surface grid and conserved variable data output files generated by CFL3D. The surface pressure is calculated from the conserved variable data at each grid point on the blade surface by the following relation.

(100) $$p = \rho_\infty a_\infty^2 (\gamma - 1)\left(e - \rho \vec{V}^2 / 2\right)$$

The surface pressure is then converted to the coefficient form below.

(101) $$cp = \frac{p - p_\infty}{1/2\, \rho (\Omega r)^2}$$

The resulting pressure distributions for several radial locations are compared to the experimental data in Figure 32 - Figure 35. The results show that the CFD model has a tendency for over predicting the blade surface pressure, which leads to higher rotor thrust estimates.

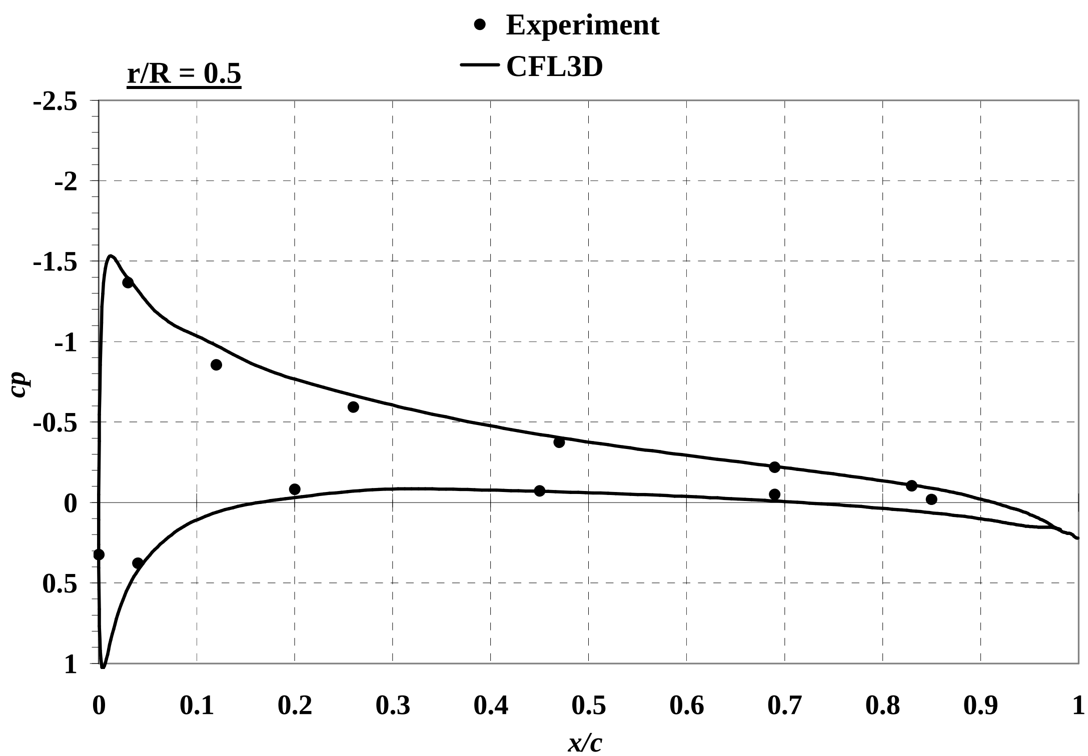

Figure 32: Chord-wise Pressure Distribution at *r/R* of 0.50

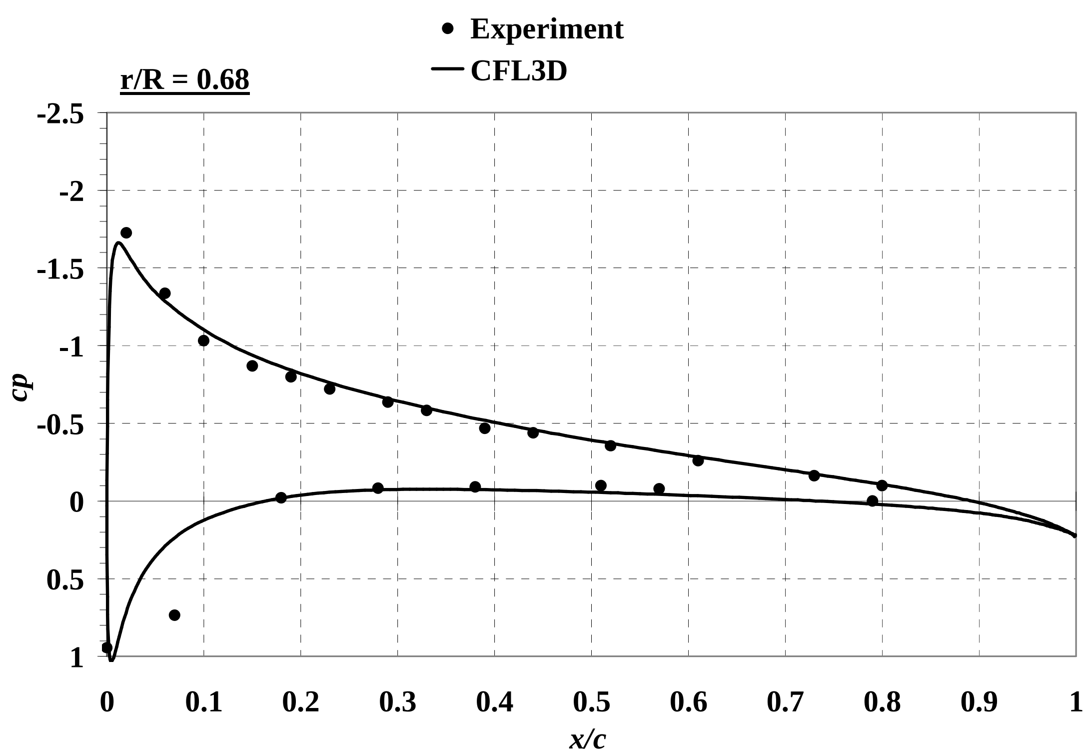

Figure 33: Chord-wise Pressure Distribution at *r/R* of 0.68

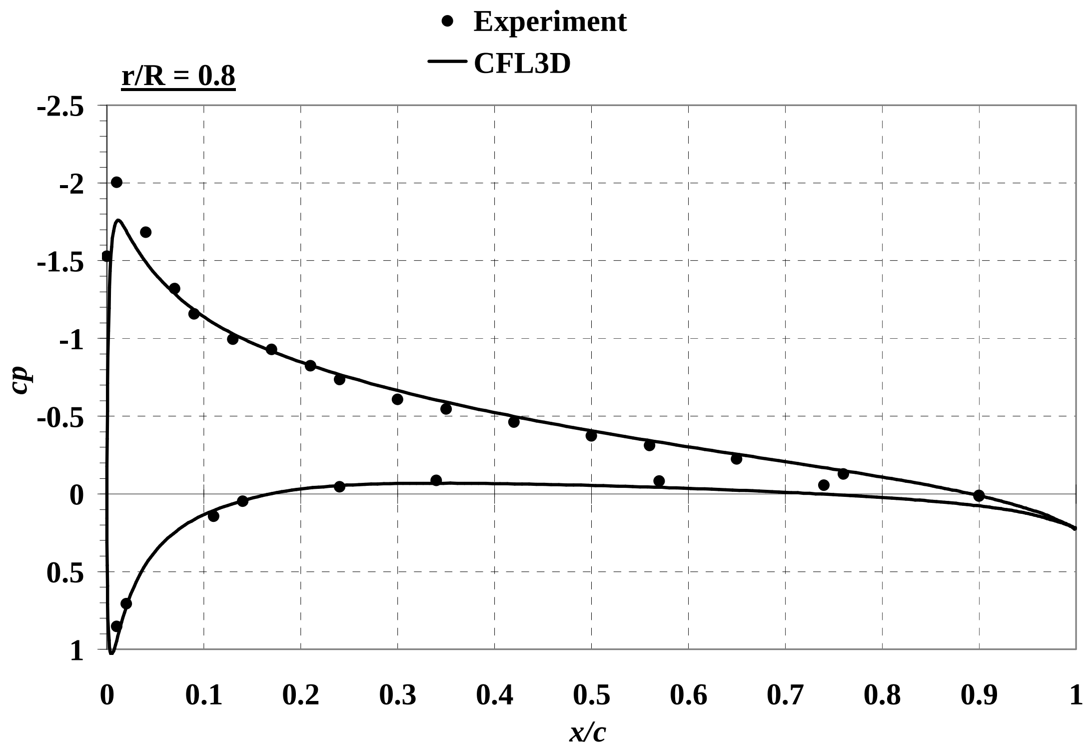

Figure 34: Chord-wise Pressure Distribution at *r/R* of 0.80

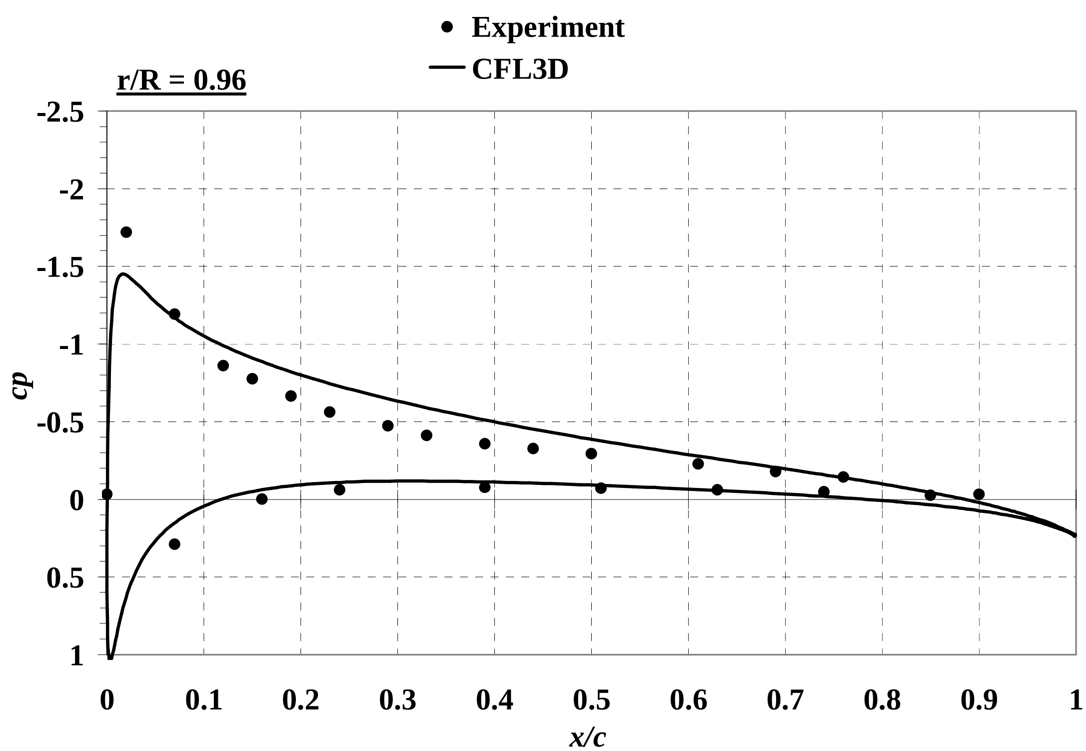

Figure 35: Chord-wise Pressure Distribution at *r/R* of 0.96

The rotor blade radial load distribution is determined from the pressure and viscous forces components acting on each discretized segment of the blade surface. The pressure force acting on the surface of a segment is given by the following relation.

(102) $$\vec{F}_p = \frac{2}{\gamma(\Omega r/a_\infty)^2}(\gamma p - 1)\vec{n}\,\frac{S_{seg}}{S_{ref}}$$

The viscous force acting on the same blade segment is defined by the following equation.

(103) $$\vec{F}_v = \frac{4}{(\Omega r/a_\infty)\mathrm{Re}}\mu\left(\vec{V} - \left(\vec{V}\cdot\vec{n}\right)\right)\frac{S_{seg}^2}{S_{ref}\,v_{seg}}$$

The lift and drag coefficients are then determined from the Cartesian force components resulting from equations (102) and (103).

(104) $$C_l = \frac{\left(F_z\cos(\alpha) + F_y\sin(\alpha)\right)_r}{1/2\,\rho(\Omega r)^2 S_{ref}}$$

(105) $$C_d = \frac{\left(F_z\sin(\alpha) + F_y\cos(\alpha)\right)_r}{1/2\,\rho(\Omega r)^2 S_{ref}}$$

The rotor torque can then be computed by summing the Cartesian force components, multiplied by the radial distance, along the blade.

(106) $$Q = \sum_{r=r_0}^{R}\left(F_z\sin(\alpha) + F_y\cos(\alpha)\right)_r r$$

The comparison of the radial load distribution between the CFD model and the experimental results is shown in Figure 36. The trend of the radial lift coefficient shows good agreement with the experimental results over most of the blade span. The increased loading compared to the experimental data produces a larger value for the rotor thrust as predicted by the chord-wise pressure distributions. An analytical study of the rotor configuration, containing an estimate of the rotor power, is included for comparative purposes and is presented in Table 8 along with the experimental and CFD results [Tung *et al*., 1981].

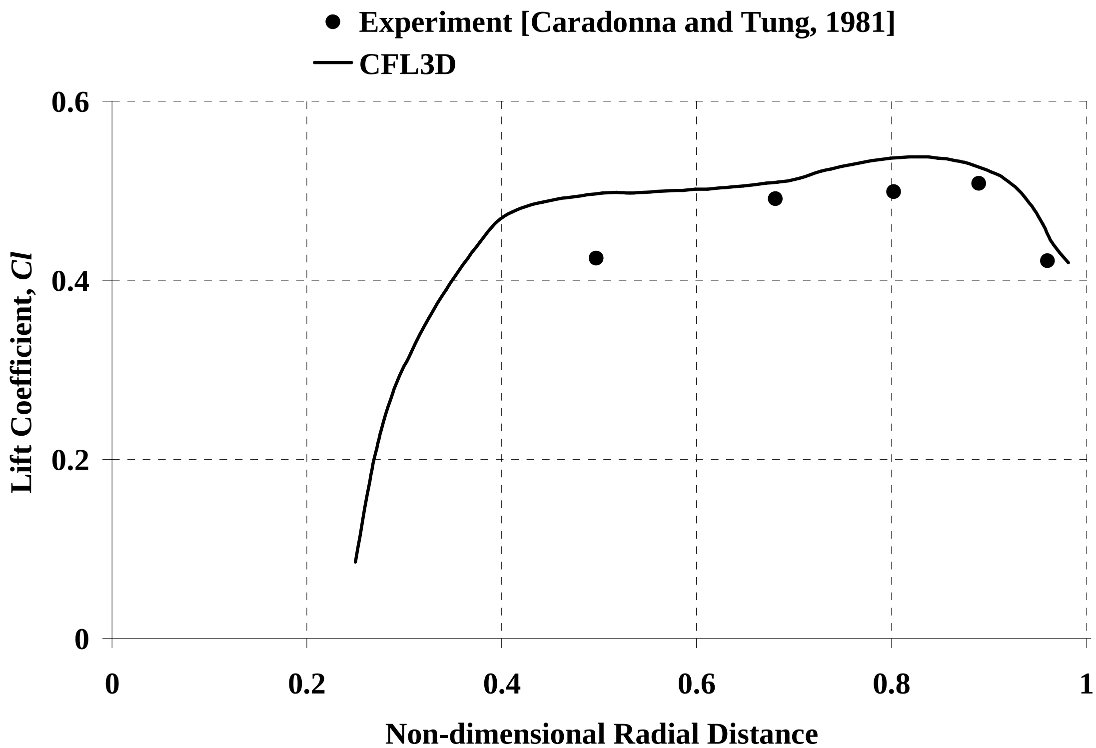

Figure 36: Radial Lift Coefficient Distribution Comparison

Table 8: Rotor Thrust Comparison at 12 Degrees Collective Pitch

	C_T	C_P
Experiment [Caradonna and Tung, 1981]	7.90E-03	-
Analytical [Tung *et al*., 1981]	8.30E-03	9.58E-04
CFL3D	8.71E-03	1.19E-03
Difference (%)	10.25%	-

4.3.3 Conclusion

The computational model of the hovering rotor shows good agreement with the experimental results given by Caradonna and Tung (1981) in terms of predicting the radial pressure distributions and the radial blade load distribution trend. The resulting difference in the predicted rotor trust is around 10% higher than the measured value. The model shows an increased dissipation of the tip vortex after a wake age of 360 degrees. Increasing the grid points in the rotor wake is a possible solution to improve the model accuracy. However, the computation time is already very high for this simulation, given the available computer resources.

4.4 Chapter Summary

Three validation studies were performed for this research. The first validation study compares a blade element, prescribed vortex wake rotor aerodynamic model to experimental data. This study allowed for the appropriate model parameters to be determined. The rotor aerodynamic model may now be applied to the rotary wing ejector sizing and performance prediction methods presented in the subsequent chapter. The second validation study is a comparison of an ejector flow using a 2D model in order to determine the model prediction fitness, appropriate grid density, and turbulence model. The knowledge gained from this study is applied to the two-dimensional CFD models critical to the rotary wing ejector sizing and performance prediction methods. The third validation study compares a three-dimensional model of a hovering rotor to an experimental study to determine CFL3D's fitness for predicting this type of flow. The experience gained in this study aid in the grid generation and model execution of the more complicated 3D rotary wing ejector model.

CHAPTER 5

ROTARY WING EJECTOR SIZING AND PERFORMANCE PREDICTION METHODS

A reaction drive rotor with an integrated ejector nozzle involves the coupled disciplines of thermodynamics and aerodynamics to characterize the complete system. The ejector nozzle geometry is dependant on the available volume at the tip of the rotor blade and the thrust required by the device. The geometry and gas flow characteristics in turn affect the lifting capability and power requirements of the rotor for a given flight condition, which directly translate back into the ejector nozzle thrust requirement. This coupling is addressed through a fixed point iterative procedure in order to determine both the size of the tip jet ejector nozzle and its performance for a given rotor configuration.

5.1 Rotary Wing Ejector Nozzle Sizing

The first step in predicting the performance of a rotary wing ejector is to size the ejector geometry based on a given rotor configuration. This requires the integration of the rotor aerodynamic model, reaction drive thermodynamic model, ejector thermodynamic model, and two-dimensional CFD model. A hovering rotor flight condition is assumed as the sizing point for the rotary wing ejector, which is typically the most demanding for a rotorcraft. A basic ejector layout is selected for this study, with upper and lower shrouds trailing aft of the blade tip as shown in Figure 37.

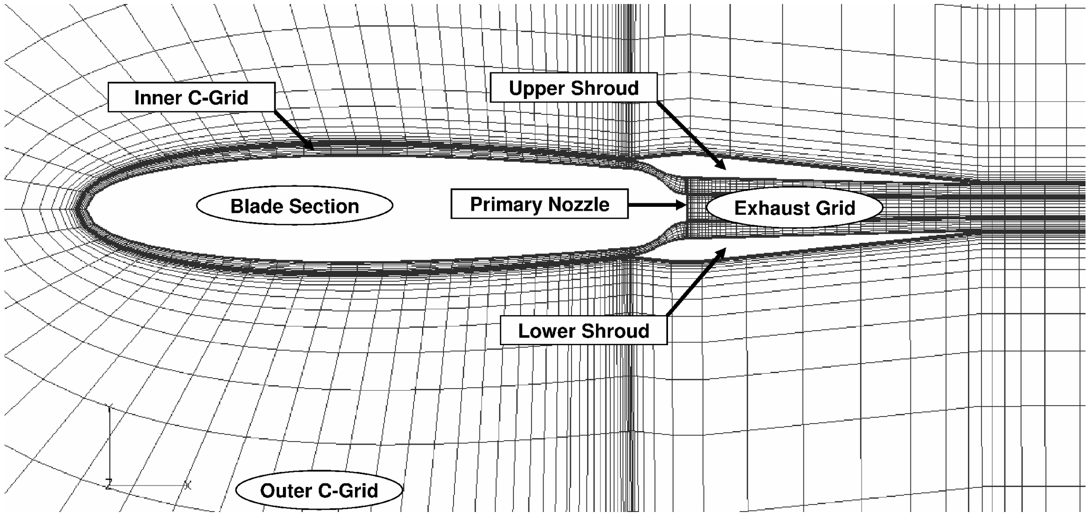

Figure 37: Rotary Wing Ejector 2D Geometric and Computational Grid Layout

5.1.1 Sizing Analysis Method

The two-dimensional geometric configuration of the rotary wing ejector nozzle, shown in Figure 37, allows for the computational grid to be divided into three primary blocks; an inner C-grid, an outer C-grid, and an exhaust grid. The geometric definition of this blade section is based on a 12% thick, symmetric, NACA four series airfoil. In order to determine the upper and lower inlet areas, mixing section area, and exit area of the ejector nozzle, both the position of the ejector shroud along chord-wise direction and length of the ejector shroud are assumed for this research. In addition, the chord-wise length of the ejector inlets and radial-wise width of the ejector are assumed.

The rotary wing ejector sizing procedure begins with the basic rotor parameters presented in Table 9 and sectional lift and drag values for a 12% thick symmetric NACA airfoil [Dadone, 1976]. The subsequent sizing iterations rely on the lift and drag predicted using 2D CFD modeling for the geometric configuration presented in Figure 37. Overall convergence is determined both geometrically and thermodynamically through the change in flow areas and flow parameters within the ejector nozzle. To initialize the thermodynamic model within the sizing procedure for this ejector nozzle, a first guess assumes the upper and lower inlet pressure, temperature, and Mach number are equal to the free stream conditions at the rotor blade tip.

Table 9: Model Rotor Parameters

Radius (ft)	3.75
Mean Chord (ft)	0.5
Root Cutout (ft)	0.75
Number of Blades	2
Rotor RPM	1250
Tip Speed (ft/s)	491
Linear Twist Rate (deg/ft)	0
Taper Ratio	1

The lift and drag of the blade tip section are used in the rotor aerodynamic model to predict the required torque to hover and the subsequent ejector nozzle thrust required. The reaction drive and ejector nozzle thermodynamic models balance the flow conditions and areas needed to produce this required nozzle thrust.

After the first iteration and the ejector nozzle geometry defined, a two-dimensional computational grid can be generated. CFL3D is utilized to compute the lift and drag over a range of angles of attack and free stream Mach numbers. Data collected from the CFD model sweeps are compiled into several formatted look up tables; providing updated lift and drag coefficients for the rotor aerodynamic model and the upper and lower inlet flow conditions for the reaction drive and ejector nozzle thermodynamic models. After the ejector solution has been updated, it is compared to the previous solution to determine the relative change in the ejector geometry and flow conditions. These relative changes, or residuals, are the primary metrics for determining convergence. A graphical representation of the rotary wing ejector sizing method is presented in Figure 38.

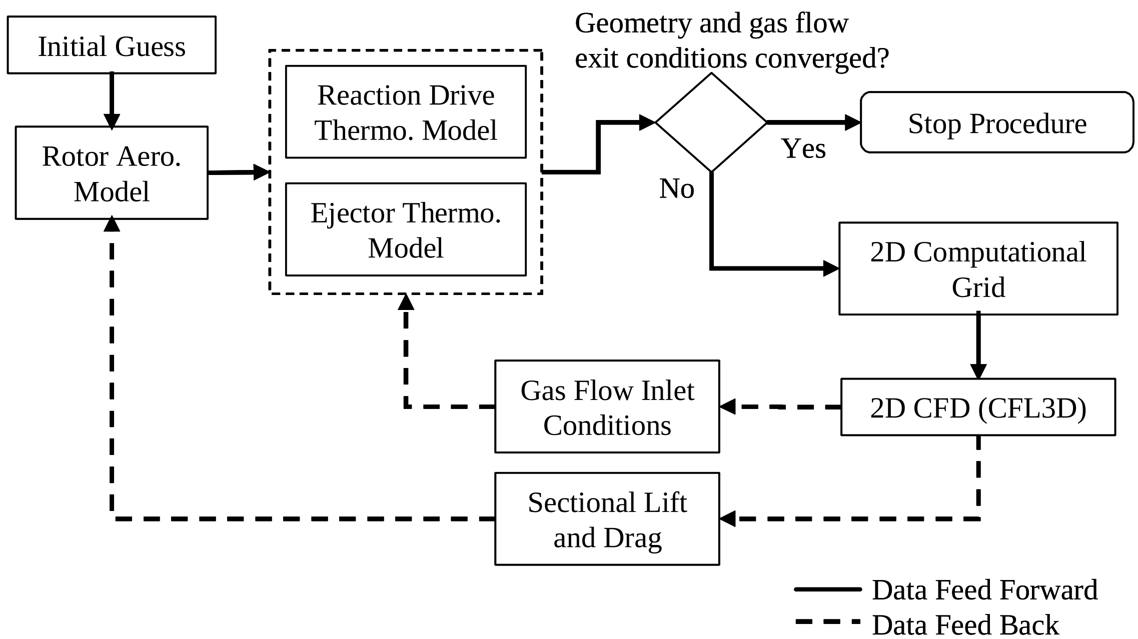

Figure 38: Rotary Wing Ejector Sizing Procedure Flow Chart

5.1.2 Two-Dimensional CFD Grid Convergence

The 2D structured grid generated for the rotor blade tip jet ejector section, shown in Figure 37 with every fourth point displayed for clarity, contains 841,854 grid points and is multigridable to four grid coarseness levels. There are a total of 33 2D CFD models run for each iteration, representing 11 angles of attack ranging from 0 degrees to 10 degrees and 3 Mach numbers ranging from 0.3 to 0.5. For brevity, a small sample of these models is selected to examine the 2D CFD model grid convergence using the drag coefficient as a metric. The resulting grid convergence is presented in Table 10.

Table 10: Two-Dimensional Drag Grid Convergence

	Number of Grid Points	Drag Coefficient, *Cd*		
		Mach 0.3 AoA 0 deg	Mach 0.4 AoA 6 deg	Mach 0.5 AoA 10 deg
Coarse Grid	210,464	0.088	0.039	0.175
Medium Grid	420,928	0.061	0.033	0.144
Fine Grid	841,854	0.060	0.034	0.138
Richardson Extrapolation	-	0.060	0.034	0.137

5.1.3 Geometric and Thermodynamic Convergence

The convergence of the rotary wing ejector sizing procedure is determined by the change in the upper and lower inlet areas and ejector exit area, and the change in continuity, momentum, and energy. This change, or residual, is defined by the generalized equation below.

$$\textbf{(107)} \quad residual = \sqrt{\sum_j \left(\frac{x_{j,i+1} - x_{j,i}}{x_{j,i}} \right)^2}$$

The term x represents the vector of convergence metrics and i is the iteration number. After each iteration, the current values for the ejector areas, continuity, momentum, and energy are compared to the values computed at the previous iteration using equation (107). There is presumed to be a tangible difference in the rotor power required between a clean rotor and the reaction drive rotor with the ejector nozzle. The ejector nozzle geometry and flow properties are linked to the rotor power through the ejector nozzle thrust required to produce the respective rotor power. CFD estimates of the lift and drag of the ejector nozzle, located at the blade tip, are needed to predict the rotor power for this configuration. The change in rotor power due to the ejector nozzle will result in a change in ejector geometry and flow conditions required to meet the power demand.

Figure 39: Sizing Procedure Geometric Convergence History

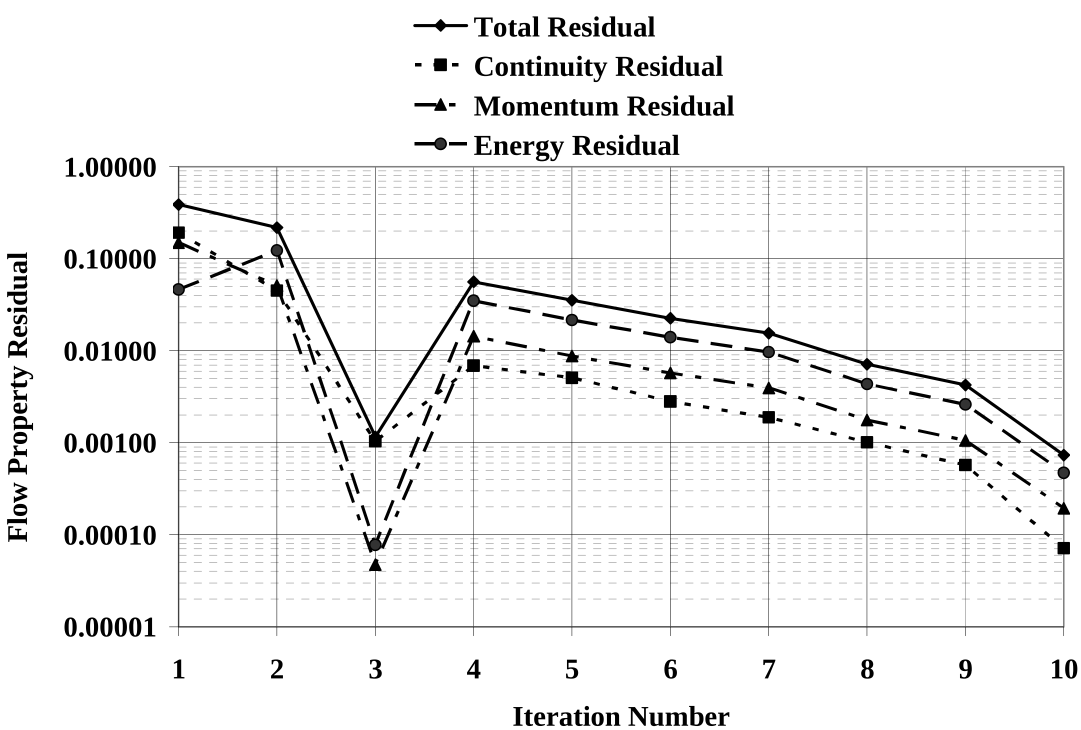

Figure 40: Sizing Procedure Flow Property Residual Convergence History

The convergence criterion for the rotary wing ejector sizing procedure is a total residual, defined as the sum of the areas, continuity, momentum, and energy residuals, less than or equal to 10^{-3}. This is achieved after ten iterations, as shown in Figure 39 and Figure 40. The convergence criterion represents less than five hundredth of a square inch in area, one degree Rankine, and one thousandth of a pound of air per second. More stringent convergence can be achieved with increasing number of iterations before convergence. The current procedure implements a manual grid generation for each step, resulting in a large amount of effort required by the user.

The convergence criteria for the rotor aerodynamic model, reaction drive thermodynamic model, and ejector thermodynamic model is 10^{-7}. The resulting sub-iteration convergence for each model over the ten iterations is shown in Figure 41. The residual for the rotor aerodynamic model represents the change in the power required as the rotor wake influence on the rotor inflow is computed during each sub-iteration. The reaction drive thermodynamic model sub-iteration residual is a function of the fuel flow to the combustion chamber, which is solved iteratively based on the ejector nozzle thrust requirement at each iteration. The ejector thermodynamic model sub-iteration residual represents the numerical convergence of the Newton method used to solve the system of equations for the one-dimensional control volume model of the ejector.

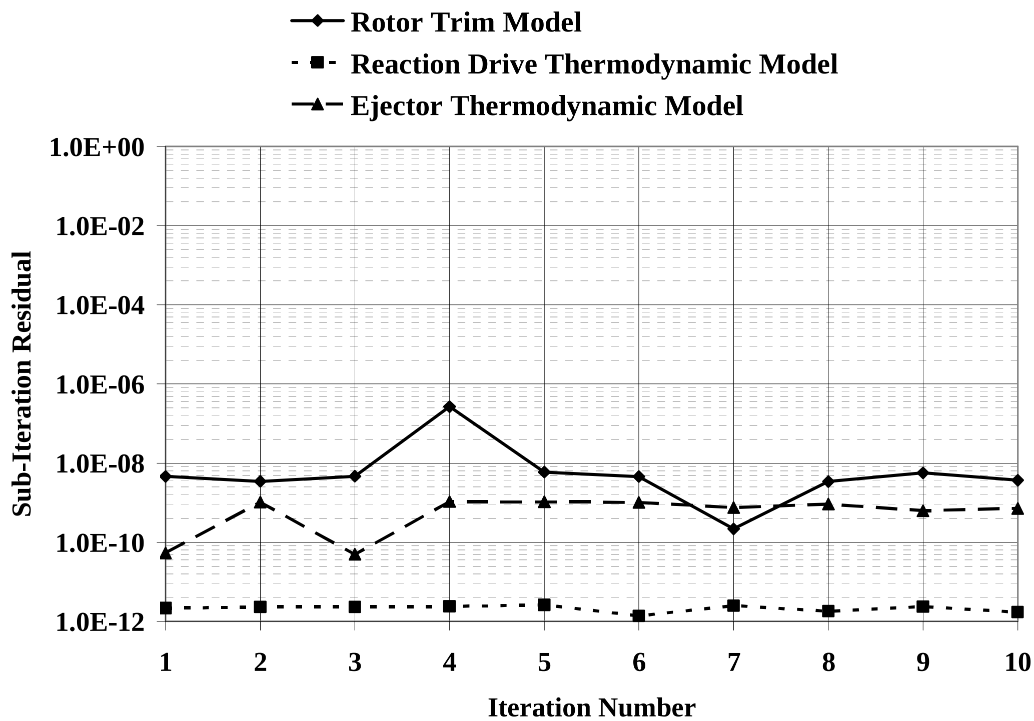

Figure 41: Sizing Procedure Sub-Iteration Convergence History

5.1.4 Rotary Wing Ejector Solution

Once the design point iteration has completed, the blade tip and ejector nozzle geometry is sized. The resulting ejector parameters are presented in Table 11. The entrance conditions at the upper and lower secondary inlets are not the same, due to the ejector nozzle operating at a positive angle of attack. This is evident by the lower secondary inlet having a larger area to provide the same mass flow rate when compared to the upper secondary inlet. Flow over the top surface of an airfoil is accelerated compared to the flow over the bottom surface at positive angles of attack. Therefore, the flow entering the lower inlet is at a slower velocity compared to the upper inlet, requiring a larger area for a fixed mass flow rate. It is important to note that the local angle of attack is not uniform across the inlet of the ejector, due to the non-uniform inflow through the rotor disk as a result of the rotor wake. The ejector secondary inlet flow parameters applied to the control volume boundaries are taken from the center section of the ejector nozzle in the radial direction and are functions of the local angle of attack and free stream Mach number. The ejector nozzle constitutes a small percentage of the rotor radius, and therefore, the variation of the local angle of attack over the ejector nozzle is small. Additionally, the rotor is assumed to be in hover, resulting in fairly steady inlet conditions around the rotor azimuth. Many of the assumptions used for this portion of the research will break down with the use of a forward flight sizing condition.

Table 11: Rotary Wing Ejector Sizing Summary

Ejector Geometry	
Upper Secondary Inlet Area (in^2)	0.35
Lower Secondary Inlet Area (in^2)	0.37
Primary Nozzle Area (in^2)	0.83
Exit Area (in^2)	1.79
Mixing Section L/D_e	1.22
Ejector Flow Parameters	
Primary Nozzle Mass Flow Rate (lb/s)	0.31
Upper Secondary Mass Flow Rate (lb/s)	0.09
Lower Secondary Mass Flow Rate (lb/s)	0.09
Total Mass Flow Rate (lb/s)	0.49
Exit Mach Number	0.70
Exit Velocity (ft/s)	1165.33
Exit Stagnation Temperature (R)	1282.88
Ejector Nozzle Thrust (lb)	16.98
Thrust Augmentation Ratio (Φ)	0.97
Rotor and Tip Jet Parameters	
Power Required (hp)	15.05
Blade Collective (deg)	12.00
Fuel Flow - JP-8 (gal/hr)	4.69

The ejector nozzle is traveling through the air at approximately Mach 0.4. The forward speed effect tends to reduce the thrust augmentation ratio, defined by the following equation [Clark, 1973].

(108) $\Phi = FN_{Ejector} \big/ FN_{\Pr imary\_Nozzle}$

The thrust augmentation ratio indicates the amount of energy transferred from the primary nozzle thrust generation to the ejector fluid entrainment and the associated ram drag. The reduction in thrust generated by the ejector nozzle, due to this transfer of energy and increased drag, requires the addition of energy from the primary nozzle, in this case additional fuel, to meet the ejector nozzle thrust requirement for the hovering rotor. Additionally, the amount of fuel burned in the combustor model needed to be increased over the value required by the reaction drive nozzle alone (without the ejector) in order for the ejector thermodynamic model to reach a feasible solution. In fact, the percentage of increase in the amount of fuel burned by the rotary wing ejector may be treated as a design variable due to its influence on the final thermodynamic solution.

A comparison of the radial load distribution is presented in Figure 42. The rotary wing ejector rotor shows a reduced amount of lift along the inboard section of the blade when compared to the model of a clean rotor. A pronounced increase, followed by a large decrease in lift is present at the tip region. The discontinuous drop in the lift is due to the model transitioning from the airfoil section to the ejector section. It is undetermined at this time whether this behavior is purely the result of the rotor aerodynamic model, or if it has some physical basis. Figure 43 shows that the local angle of attack of the ejector nozzle section of the rotor blade is not greater than 5 degrees, well below flow separation due to stall. Again, the discontinuous break in the radial distribution of the local angle of attack indicates the change from the 12% thick symmetric airfoil section to the ejector section within the rotor aerodynamic model.

The increased drag of the tip jet ejector nozzle blade section, shown in Figure 44, is expected due to the geometry and ejector exhaust. The maximum lift coefficient is slightly greater for the ejector section. A closer inspection of the CFD results shows some recirculation of the airfoil upper surface separated flow into the upper inlet at the higher angles of attack, shown in Figure 45.

A comparison of the thrust and power between the rotary wing ejector and a clean rotor is presented in Table 12. The resulting rotor thrust coefficient is significantly less for the same collective pitch angle and has a higher power requirement. Trimming the blade collective pitch angle to match the rotor thrust further increases the power required above the baseline rotor configuration, shown in Table 12.

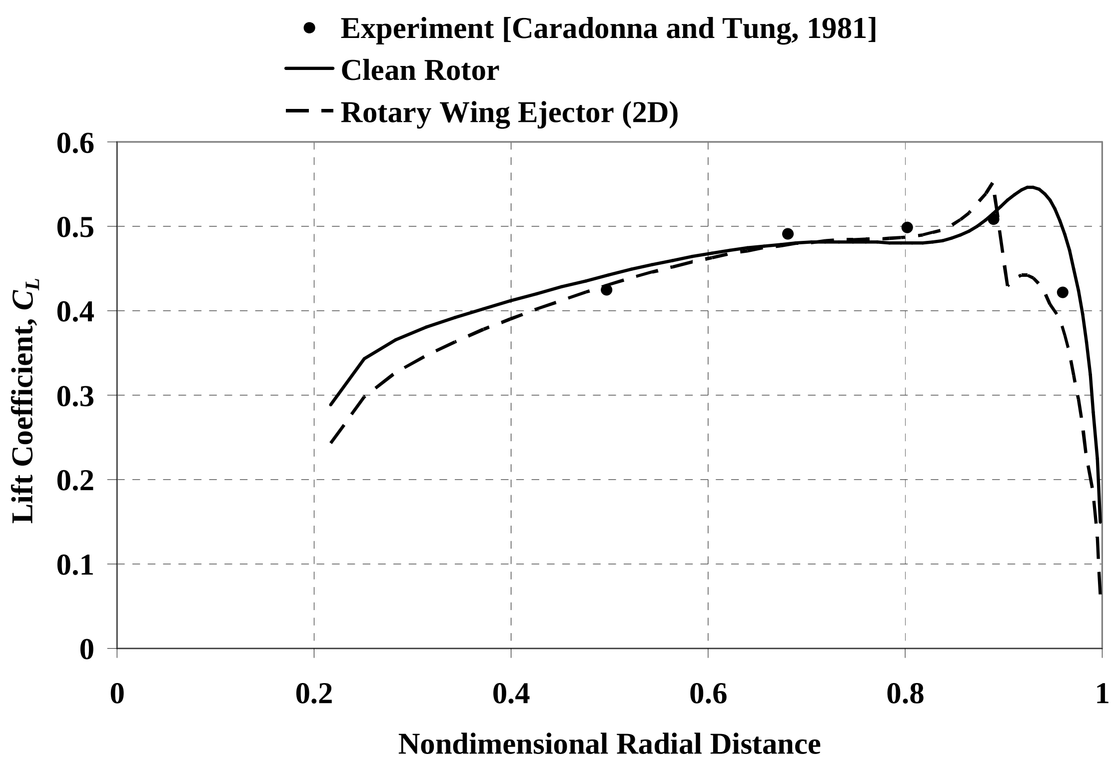

Figure 42: Radial Lift Coefficient Distribution Comparison

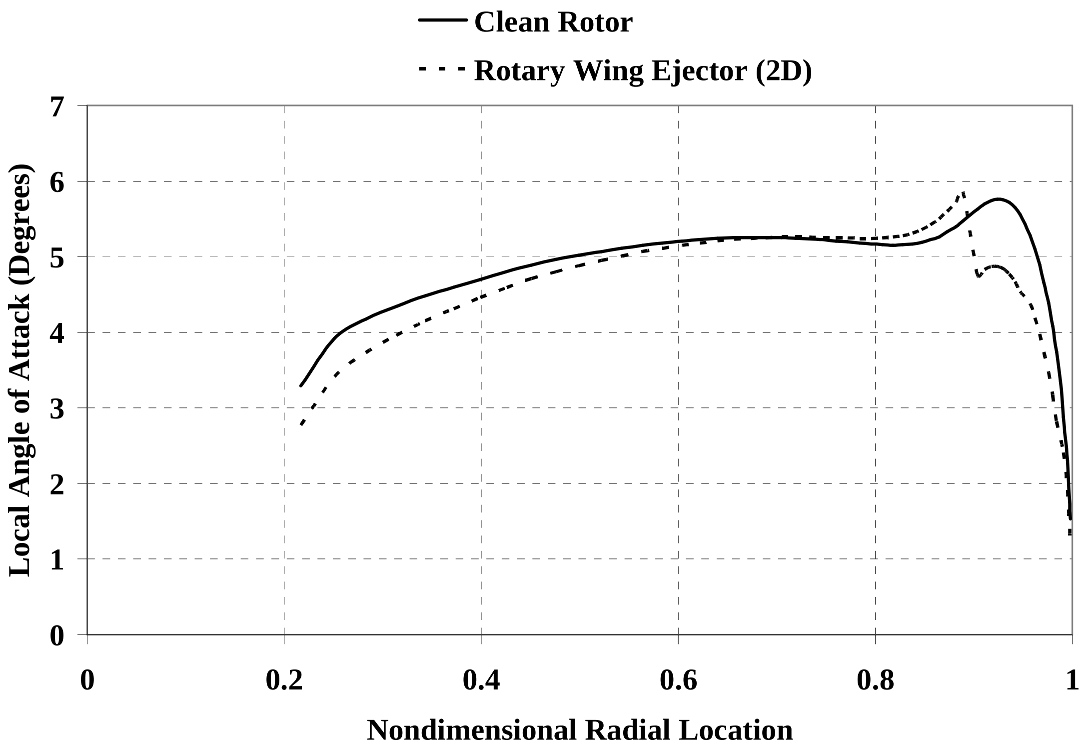

Figure 43: Angle of Attack Radial Distribution Comparison

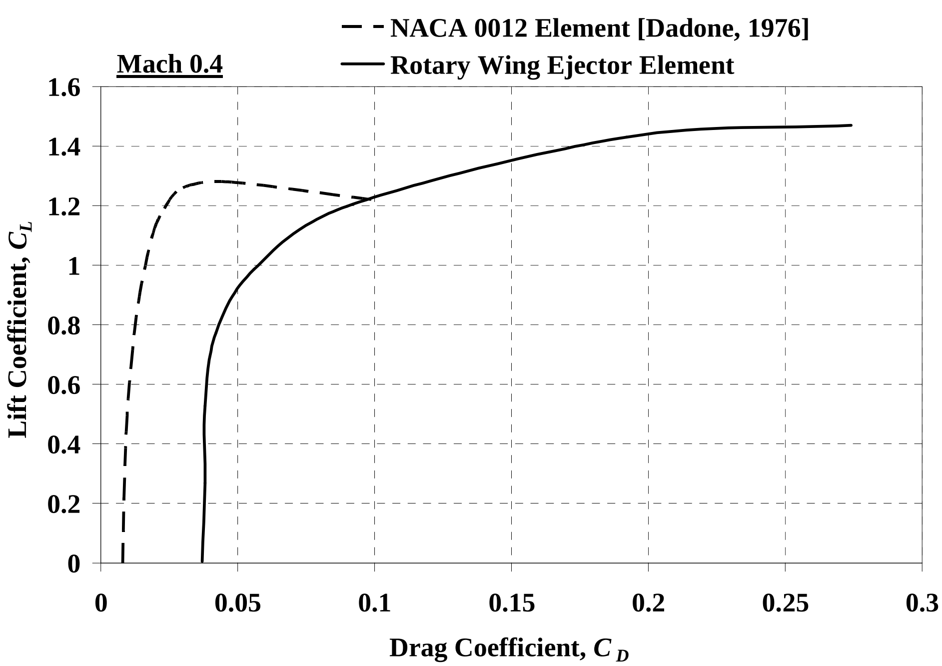

Figure 44: Two-Dimensional Sectional Drag Polar Comparison

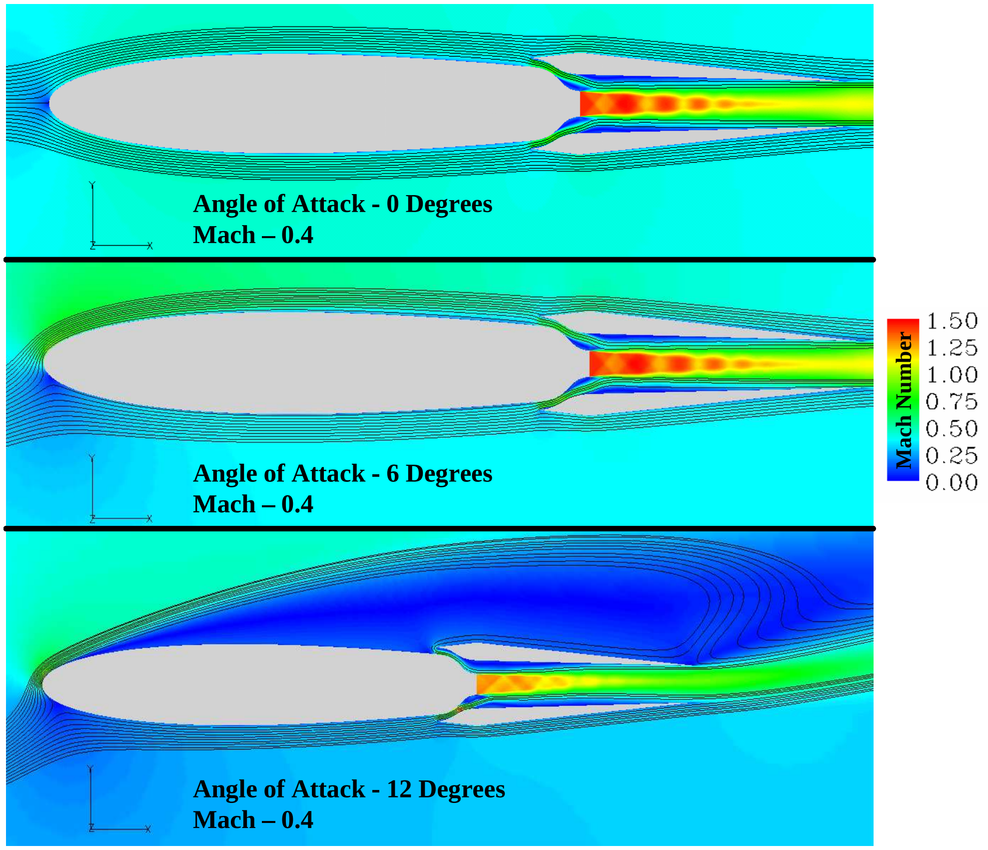

Figure 45: Two-Dimensional CFD Flow Visualization

Table 12: Rotor Thrust and Power Comparison

	Collective (deg)	C_T	C_P
Clean Rotor	12.00	8.14E-03	1.05E-03
Rotary Wing Ejector (2D)	12.00	6.87E-03	1.33E-03
Rotary Wing Ejector (2D)	13.33	8.14E-03	1.49E-03
Constant Collective Pitch Angle (%)	0.00%	-15.60%	26.67%
Constant Thrust (%)	9.94%	0.00%	41.62%

5.2 Rotary Wing Ejector Performance

The thermodynamic models of the reaction drive and ejector nozzle developed above are modified to compute the thermodynamic flow properties for a fixed geometric configuration. This allows for the prediction of performance characteristics of the rotary wing ejector at conditions separate from the sizing point. The operating conditions for this performance prediction method are only dependant on the capability of rotor aerodynamic model selected. The current study is focused on a hovering rotor model; however, forward flight could be analyzed by simply replacing the rotor aerodynamic model.

5.2.1 Performance Prediction Method

Off design reaction drive and ejector nozzle thermodynamic models are developed to predict the performance for a range of hovering flight conditions. CFL3D is used in a similar fashion to the rotary wing ejector sizing procedure by computing the sectional air loads and secondary inlet temperature, pressure, Mach number, and mass flow rate as functions of angle of attack and free stream Mach number.

The hovering rotor model computes the required torque for given rotor collective pitch angles utilizing the CFD generated lift and drag data for the ejector nozzle section of the blade. The torque required is then passed to the reaction drive and ejector off design thermodynamic models. The primary nozzle and ejector exit areas, determined by the thermodynamic models, are then used to update the 2D computational grid used by CFL3D. The sectional air loads and the secondary inlet conditions are recomputed and the associated lookup tables containing the sectional lift and drag are updated. This procedure is repeated to account for the effects of the change in the ejector nozzle thrust, and subsequent exit area and flow conditions. The rotary wing ejector performance prediction method allows for varying rotor thrusts and flight altitudes and temperatures. A graphical representation of the analysis method just described is presented in Figure 46.

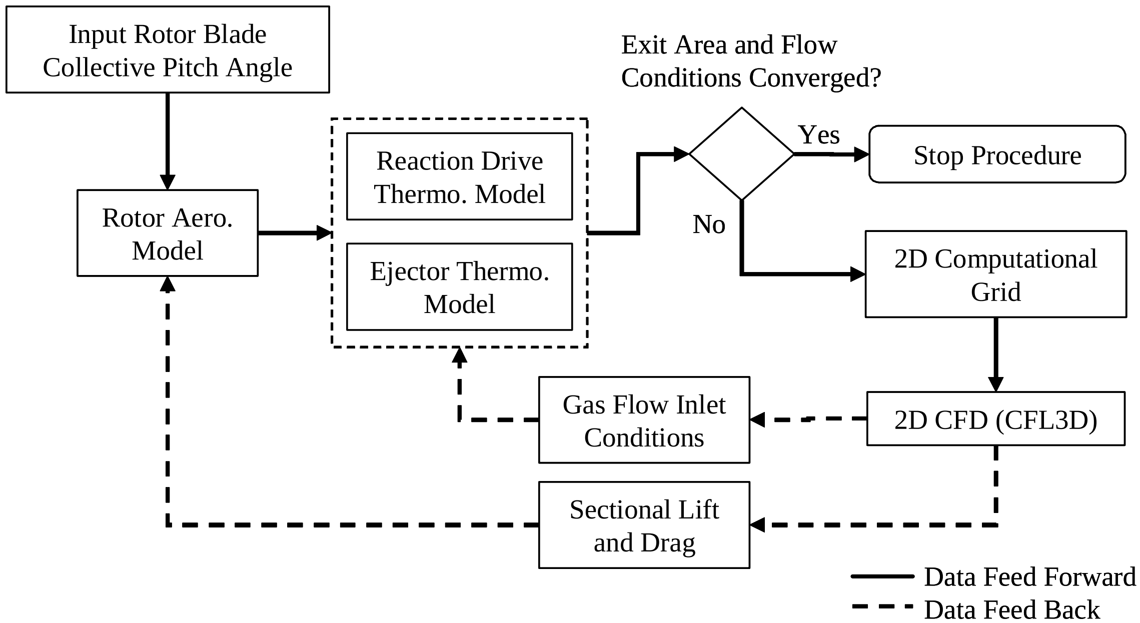

Figure 46: Rotary Wing Ejector Performance Procedure Flow Chart

5.2.2 Rotary Wing Ejector Performance Trends

The rotary wing ejector performance analysis, shown in Figure 46, is applied to a range of rotor blade collective pitch angles from 8 to 14 degrees. At each collective pitch angle the primary nozzle flow conditions are computed based on the rotor aerodynamic model, which is dependant on the blade tip CFD predicted lift and drag. The blade tip sectional lift and drag is also dependant on the nozzle flow conditions, thus requiring an iterative procedure. An initial run for each collective pitch angle is performed using the ejector sectional air load data from the final sizing solution at a collective pitch angle of 12 degrees. The CFD models re-compute the ejector sectional lift and drag using the updated ejector nozzle thermodynamic solution for the current collective pitch angle. This procedure is repeated iteratively until the relative change in convergence metrics is below a residual of 5^{-2}. This convergence criterion is higher than that of the sizing procedure primarily due to the large number of CFD models required for the rotor thrust sweep. There are 33 CFD model cases per iteration for each collective pitch angle, resulting in a significant amount of computational resources required. The total wall time for five iterations is 512 hours, 22 minutes, 15 seconds split across 8 processors.

The collective pitch selected for the sizing procedure is repeated during the performance sweep to check that the performance version of the model matches the sizing version and is presented in Table 13. The performance version of the rotary wing ejector model shows good agreement with the sizing version. The difference between the initial iteration and the final iteration for the range of collective pitch angles is shown in Figure 47 in terms of the ejector exhaust flow total residual, defined as the sum of the area, continuity, momentum, and energy residuals. Increasing the number of iterations for each collective pitch angle cases will improve the overall convergence. The maximum residual of 3% occurs at the lowest collective pitch angle analyzed. This is a relatively low residual and therefore the increase in model accuracy is traded against the computational cost.

Table 13: Rotary Wing Ejector Sizing and Performance Model Comparison

	Sizing Version	Performance Version	Difference (%)
Ejector Flow Parameters			
Primary Nozzle Mass Flow Rate (lb/s)	0.31	0.31	-0.47%
Upper Secondary Mass Flow Rate (lb/s)	0.09	0.09	0.66%
Lower Secondary Mass Flow Rate (lb/s)	0.09	0.09	-0.27%
Total Mass Flow Rate (lb/s)	0.49	0.49	-0.43%
Exit Mach Number	0.70	0.70	-0.50%
Exit Mean Velocity (ft/s)	1165.33	1166.87	-0.13%
Exit Stagnation Temperature (R)	1282.88	1279.97	0.23%
Ejector Nozzle Thrust (lb)	16.98	17.14	0.93%
Rotor and Tip Jet Parameters			
Power Required (hp)	15.05	15.19	0.93%
Blade Collective (deg)	12.00	12.00	-
Fuel Flow - JP-8 (gal/hr)	4.69	4.72	-0.65%

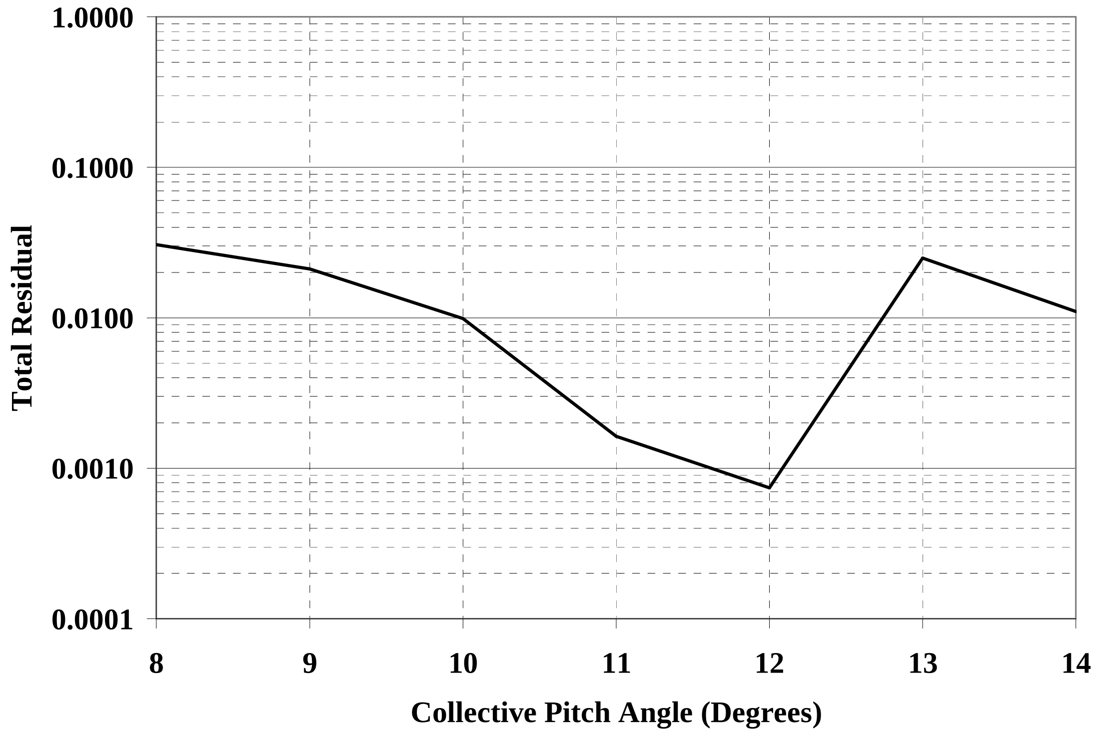

Figure 47: Performance Procedure Flow Property Total Residual Convergence

The performance of the rotary wing ejector for a range of rotor thrusts is compared to a clean rotor and a reaction drive rotor. The clean rotor has the same blade planform as the rotary wing ejector blade, with the main difference being the clean rotor blade has a 12% NACA airfoil section from the blade root to the blade tip. The reaction drive rotor also uses the same planform as the rotary wing ejector blade. The tip section of this blade is similar to the tip section of the rotary wing ejector blade with the ejector shrouds removed. The differences between the three rotor blades are concentrated at the blade tip region, isolating the causality of any performance implications to this region of the blade. The reaction drive rotor requires an iterative procedure to achieve trim at each blade collective pitch angle. The reaction drive thermodynamic model is run in isolation to determine the nozzle flow conditions based on a clean rotor torque required. A two-dimensional CFD model of the blade section with the reaction drive nozzle is setup and run over a range of angles of attack and Mach numbers. The lift and drag are then tabulated as functions of angle of attack and Mach number and fed back into the rotor aerodynamic model to re-compute the rotor torque required for the selected hover condition. This procedure is repeated for each hovering rotor thrust condition until there is a small relative change in the rotor torque required and reaction drive nozzle flow conditions between iterations.

A comparison of the rotor power required and Figure of Merit as a function of rotor thrust between the rotary wing ejector, clean rotor, and reaction drive rotor is presented in Figure 48 and Figure 49, respectively. The rotary wing ejector shows the expected increase in required power compared to both the reaction drive and clean rotors due to the added geometry and ejector nozzle flow. Additionally, the rotor thrust is reduced for a given collective pitch angle, indicated by the horizontal shift of the curve to the left compared to the reaction drive and clean rotor configurations. The amount of fuel burned in the combustion chamber over the range of collective pitch angles is presented in Figure 50. This trend follows the power curve trend as expected for a reaction drive rotor configuration. The increase in fuel burn compared to the reaction drive rotor is due to both the increased drag resulting from the ejector geometry and flow and the increase in energy required to mix the secondary and primary flows within the ejector. Figure 51 shows a comparison of the exit velocity between the primary nozzle and ejector nozzle computed by the ejector control volume model and the exit velocity of the reaction drive rotor nozzle. The result shows the ejector nozzle reducing the exit velocity across the range of rotor thrusts. The magnitude of the reduction in exit velocity is based on idealized assumptions; therefore, this result only provides a lower bound. The peak velocity at the exit plane of the ejector from the 2D CFD model is also included in Figure 51. This provides an upper bound, as the two flows are only mixed thought the turbulent shear layer. Comparing the exit velocities between the 2D CFD results and the reaction drive rotor show that indicate that the peak velocity is greater for the rotary wing ejector. This is due to increased output from the primary nozzle to overcome the thrust losses and drag penalties caused by the ejector nozzle. Because there is limited volume at the tip of the rotor blade, the mixing length to achieve complete mixing is insufficient through the turbulent shear layer alone. A forced mixing primary nozzle would increase the amount of mixing between the secondary and primary flows; however, it may still not achieve the one-dimensional control volume results.

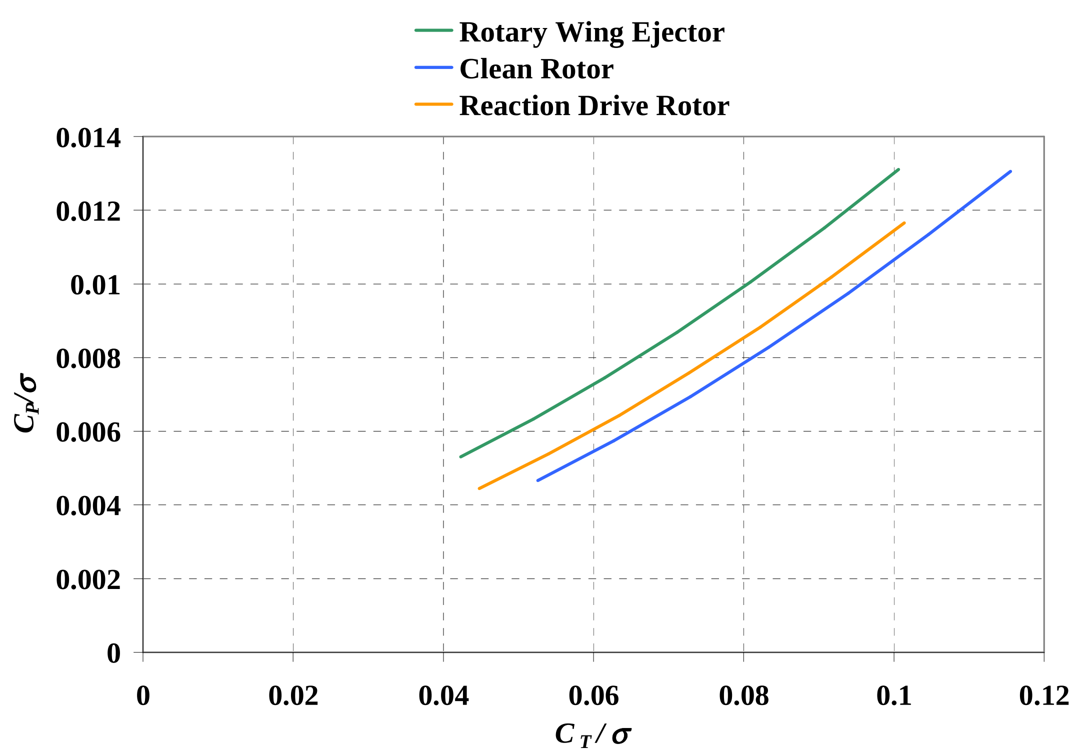

Figure 48: Rotor Power as a Function of Thrust

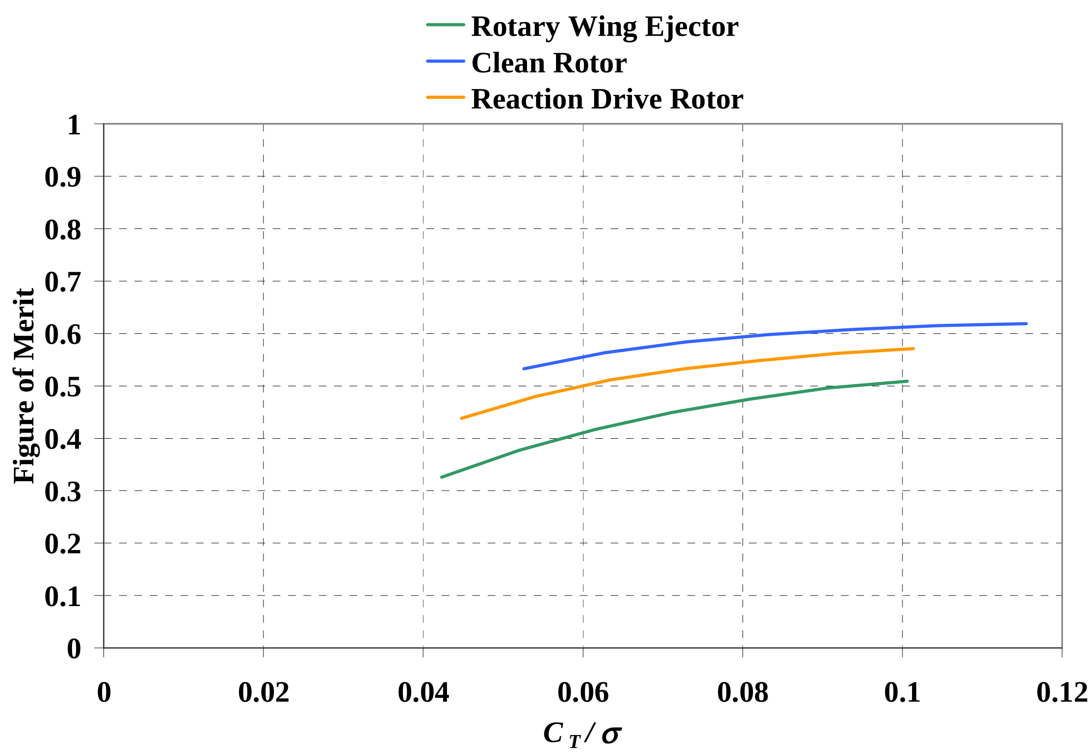

Figure 49: Rotor Figure of Merit as a Function of Thrust

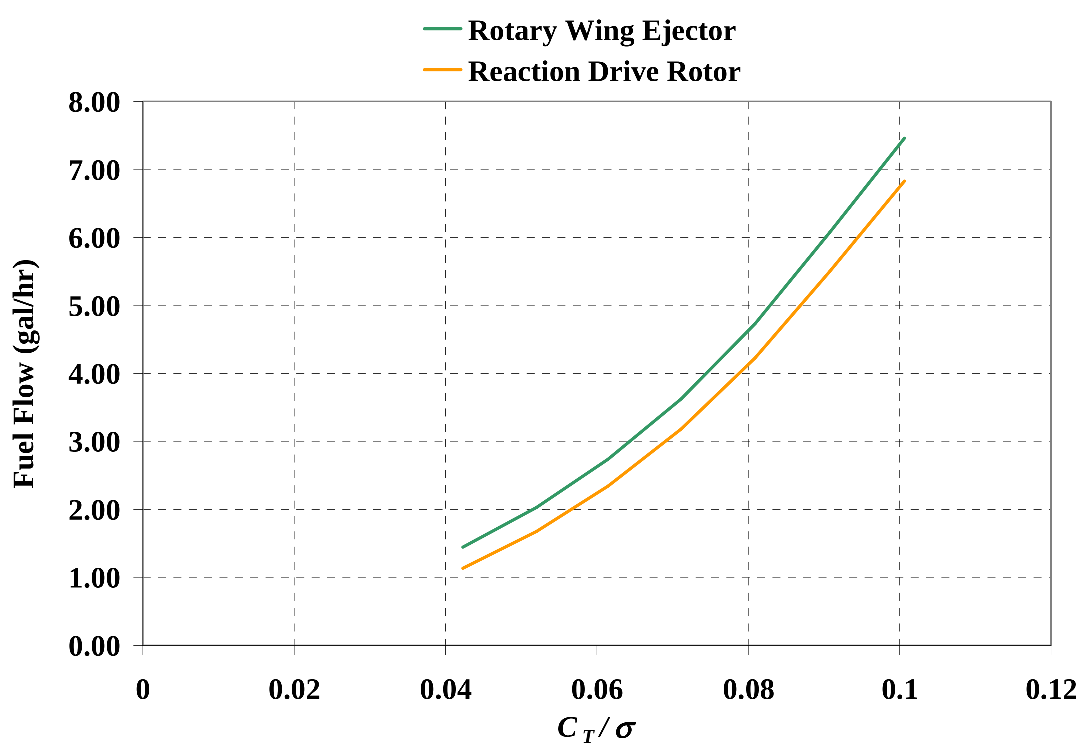

Figure 50: Tip Jet Fuel Flow as a Function of Rotor Thrust

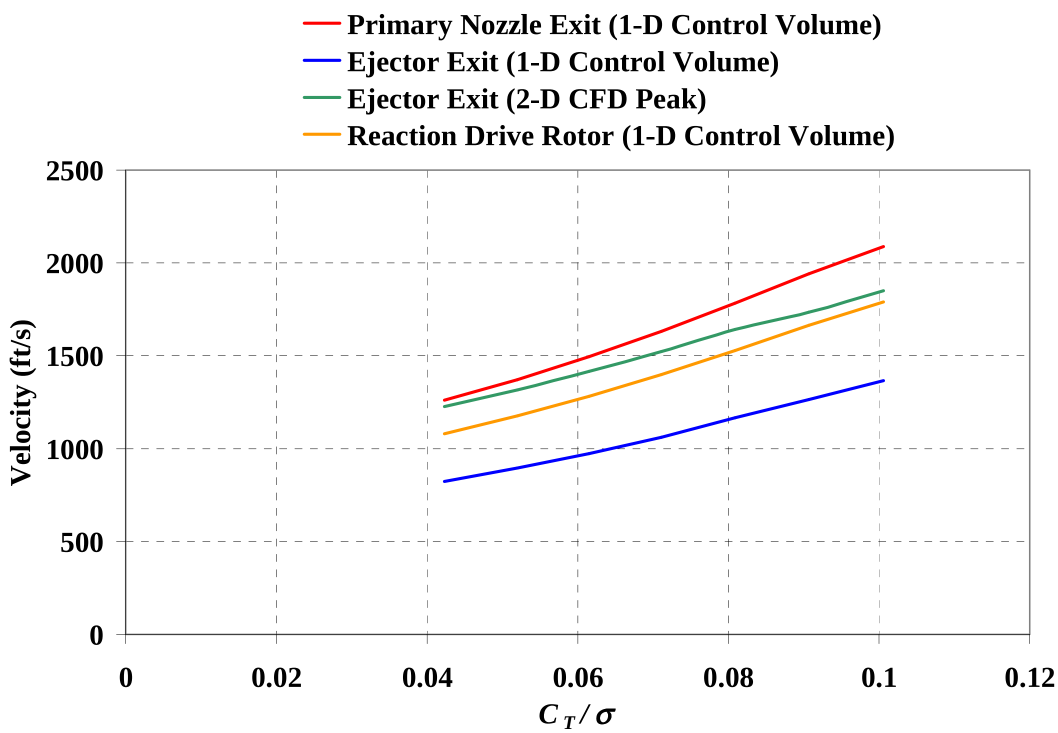

Figure 51: Ejector Nozzle Exit Velocity as a Function of Rotor Thrust

5.3 Chapter Summary

The primarily focus of this study is the development of a coupled, multi-disciplinary, analytical method to address sizing and performance of a rotary wing ejector in hover. The study also provides some insight into the aerodynamic and thermodynamic characteristics of this rotor and ejector configuration in the hovering flight condition. Basic aerodynamic and thermodynamic aspects are investigated with the intent of providing a foundation for both higher fidelity aerodynamic modeling and acoustic predictions.

It is recognized that not all of the fluid dynamic processes and interactions are captured under the present assumptions. However, the reduced computational modeling effort allows for design tradeoffs and basic performance trends to be performed for this rotor configuration in an early stage of design that may lack detailed knowledge of the rotor. Full integration of the grid generation and CFD modeling into both the sizing and performance procedures will reduce the modeler's effort and the possibility of error. Additionally, it was discovered that the amount of fuel burned in the combustor model needed to be increased over the value required by the reaction drive nozzle alone (without the ejector) in order for the ejector thermodynamic model to reach a feasible solution. In fact, the percentage of increase in the amount of fuel burned by the rotary wing ejector may be treated as a design variable due to its influence on the final thermodynamic solution.

CHAPTER 6

ROTARY WING EJECTOR AERODYNAMIC ANALYSIS

A three-dimensional CFD model of the rotary wing ejector is developed to study the aerodynamic effects in a hovering flight condition. The geometric configuration is determined by the sizing procedure presented in Chapter 5. A trim procedure is implemented to balance the ejector nozzle thrust computed by the thermodynamic model with the ejector nozzle thrust required, derived from the rotor torque required calculated by the CFD model. The aerodynamic performance of this rotor configuration is compared to the clean rotor presented in Chapter 4 and the two-dimensional modeling results presented in Chapter 5. Additionally, the three-dimensional internal flow field of the ejector is compared to the two-dimensional results.

6.1 Rotary Wing Ejector Nozzle Thrust Balancing

The thrust produced by the ejector nozzle equals the thrust required to rotate the rotor blades at a specified RPM for a trimmed flight condition. The ejector nozzle thrust is a function of the primary nozzle pressure and temperature ratio, and gas velocity. These parameters are computed by the thermodynamic model presented in Chapter 5 and are based on the rotor torque required calculated by an aerodynamic model of the rotor. Therefore, an iterative procedure is required to balance the ejector nozzle thrust for a given flight condition.

The ejector nozzle thrust balancing procedure is presented graphically in Figure 52. The rotor configuration defined in Chapter 5, Table 11, is used as the starting point. The rotor and ejector geometry are used to generate a three-dimensional computational grid. The primary nozzle pressure and temperature ratio, and Mach number are boundary conditions for the CFD model. Upon convergence of the CFD model, the rotor torque required and ejector thrust are computed. The rotor torque required is passed to the thermodynamic model of the reaction drive and ejector nozzle, where the primary nozzle pressure, temperature and Mach number are computed to match the ejector nozzle thrust required, thus providing the rotor torque required. The ejector nozzle thrust computed by the thermodynamic model is compared to the ejector nozzle thrust computed by the CFD model. If the ejector thrusts do not match, the resulting ejector primary nozzle boundary conditions are updated and the CFD model is run again; otherwise, the thrust balancing procedure is complete.

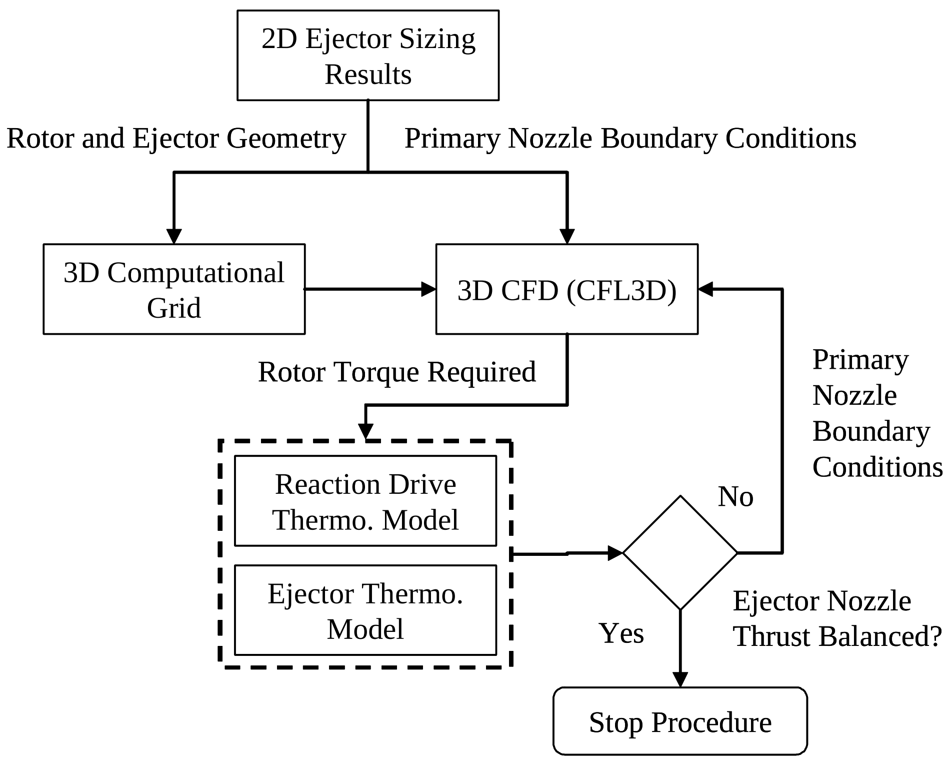

Figure 52: Ejector Nozzle Thrust Balancing Procedure

6.2 Rotary Wing Ejector Three-Dimensional Model

The three-dimensional CFD model of the rotary wing ejector is based on the configuration presented in Chapter 5, Table 11. The rotor is operating in a hovering flight condition at a specified collective pitch angle. Therefore, it is assumed that there is no flapping or lagging motion of the blades, and they are rigid. Additionally, the rotor is assumed to be axi-symmetric about the rotational axis. The entire domain is rotated at the rotational speed of the rotor in an unsteady formulation. Each time step is related to the rotational speed and the desired azimuth angle increment by the following equation.

(109) $$dt = \frac{d\psi}{360\Omega}$$

The azimuth angle increment selected for this study is 0.1 degrees, requiring 3600 time steps for one full blade rotation.

6.2.1 Grid Topology

The three-dimensional computational grid is a structured, blocked, C-H grid generated in Gridgen®. The axi-symmetric assumption allows for only one half of the two-bladed rotor to be modeled. The ejector geometry requires the C-grid surrounding the rotor to be split into several blocks. The grid points are clustered in the far wake using the wake trajectory data provided by Caradonna and Tung (1981). The overall grid topology is presented in Figure 53. The total number of grid points is 25,945,479 for the entire computational domain.

The layout of the grid blocks surrounding the rotor and ejector is presented in Figure 54. The rotary wing ejector blade is separated into four blocks along the radial direction. The first block surrounds the rotor blade from the root to the beginning of the ejector nozzle. The second block surrounds the rotor blade forward of the ejector secondary inlets and is bounded in the surface normal direction (ζ) by the ejector shroud outer surface. The third block surrounds the ejector shrouds and second block. The last block contains the upper and lower secondary inlets and the mixing section of the ejector.

A radial sectional slice of the grid surrounding the ejector nozzle is presented in Figure 55. A total of 4,549,770 grid points are contained within the ejector mixing section. The grid dimensions of this section are based on the two-dimensional modeling presented in Chapter 5. In order to interface the ejector mixing section block with the grid block trailing the rotor blade, a singularity boundary is required to collapse the grid points extending from the ejector primary nozzle.

The blade tip grid treatment is presented in Figure 56. A sharp edge at the blade tip is created with a grid block protruding from the blade tip surface, in the radial direction, to the far field. This tip arrangement provides a minimal amount of grid cell skewness; however, singular boundaries are required. These boundaries protrude from the leading and trailing edges, in the radial direction, and make up two of the grid block faces of the grid block protruding from the blade tip.

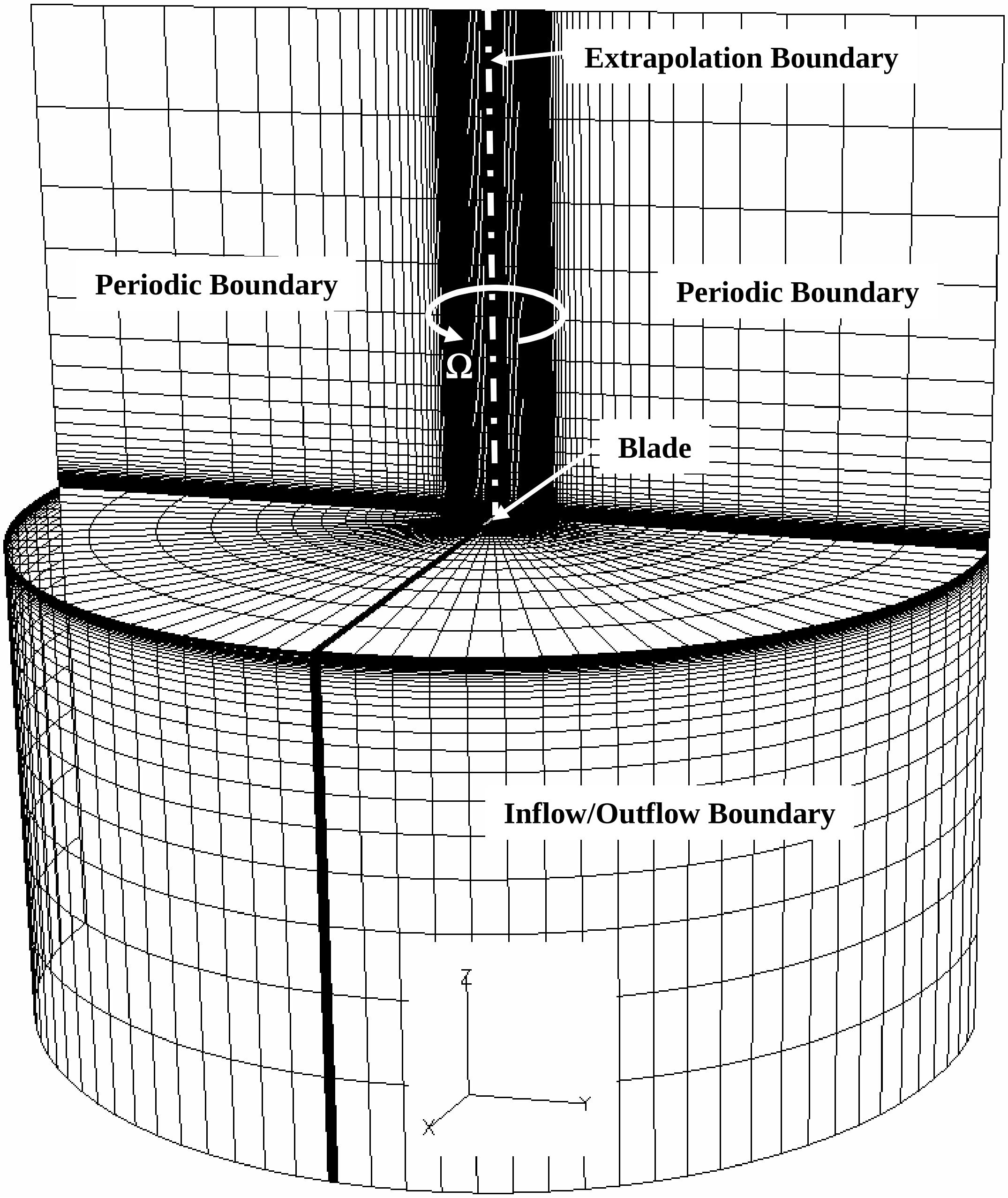

Figure 53: Rotary Wing Ejector Grid Topology

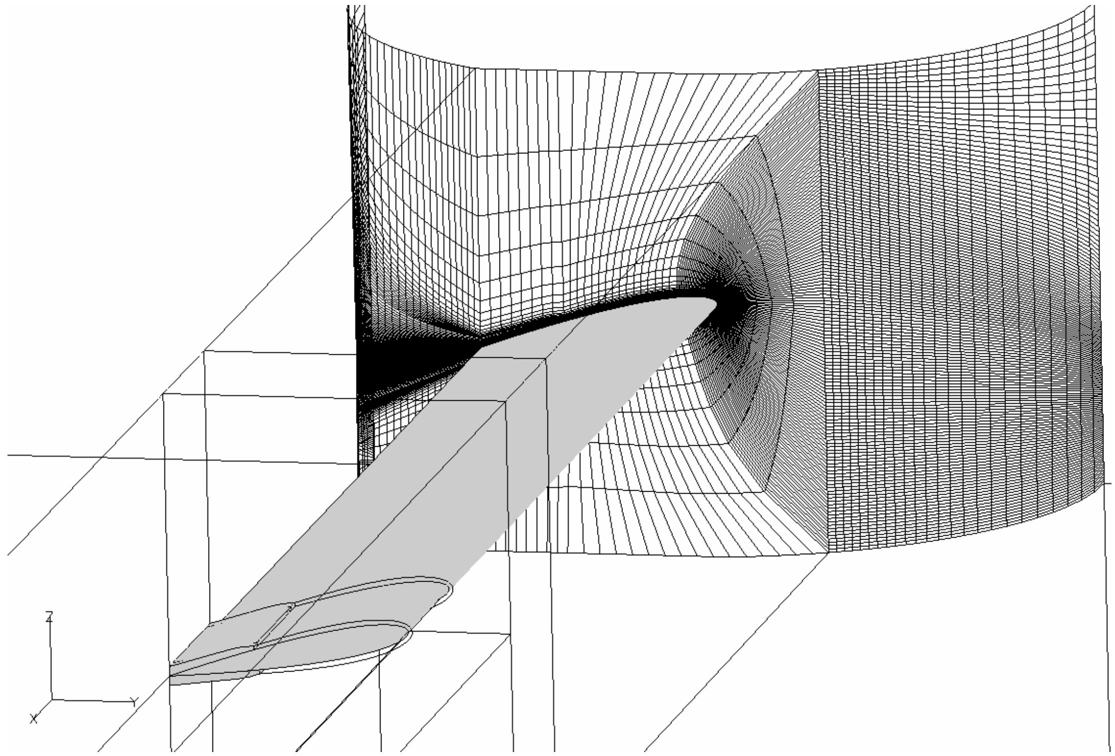

Figure 54: Rotor and Ejector Grid Block Layout

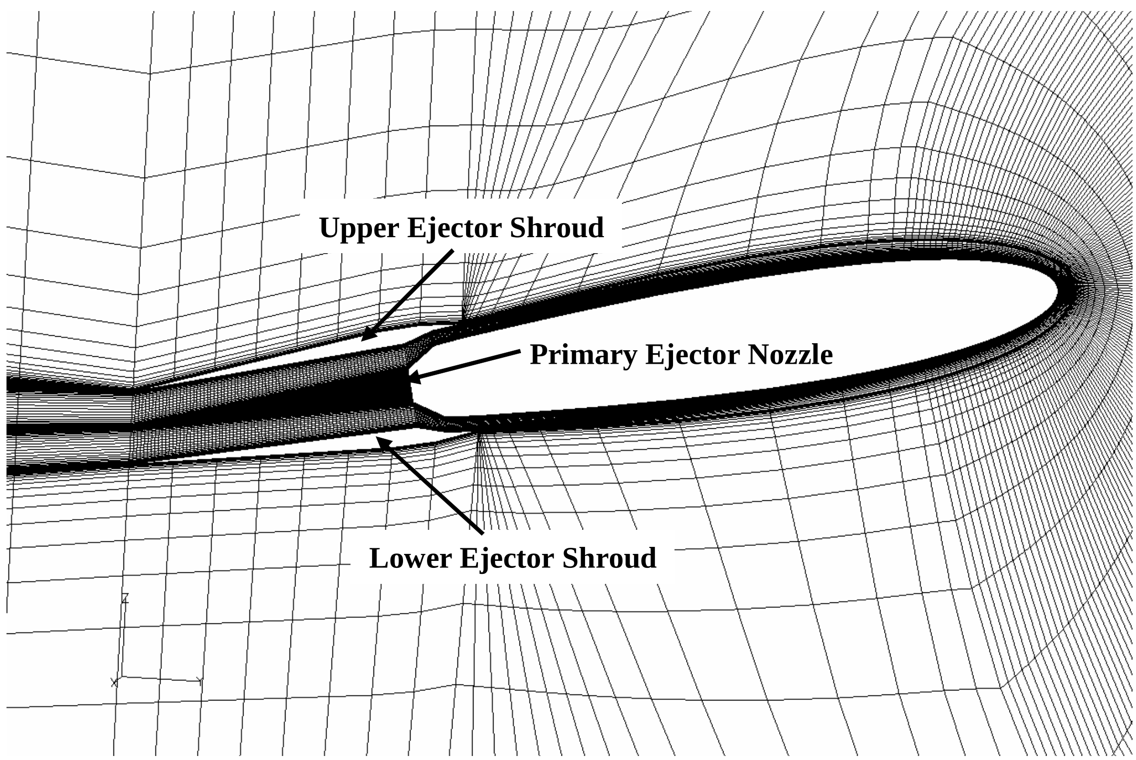

Figure 55: Ejector Radial Sectional Grid Topology

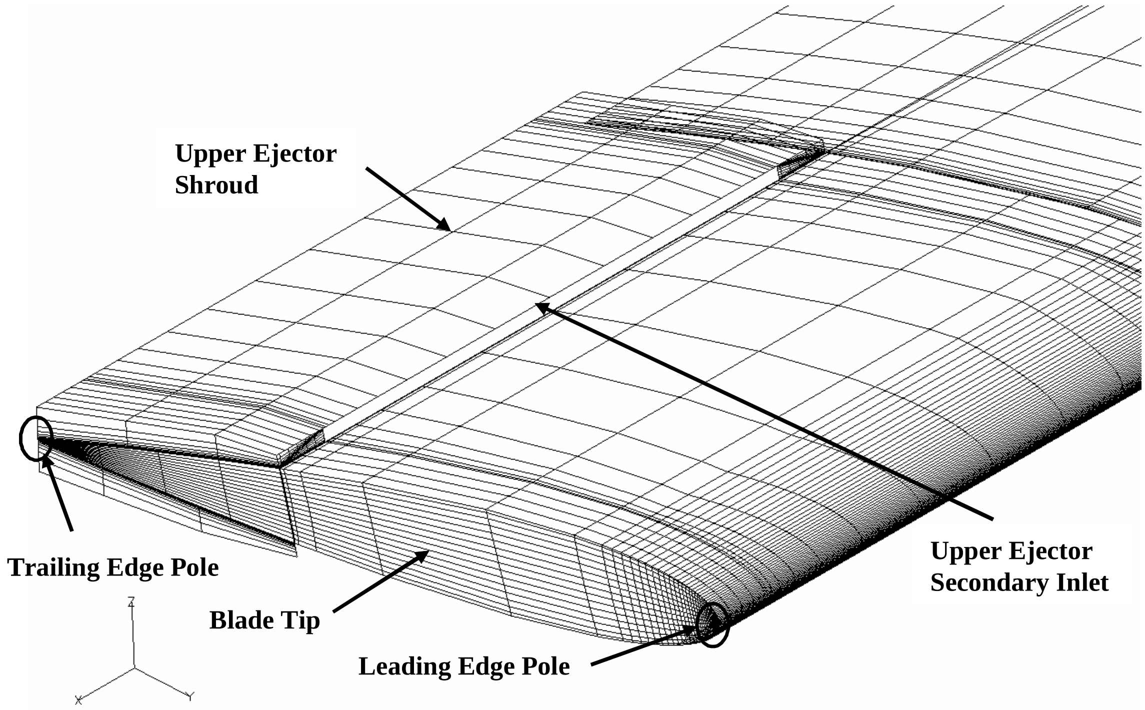

Figure 56: Blade Tip Grid Treatment

6.2.2 Boundary Conditions

The boundary conditions applied to the three-dimensional rotary wing ejector model are similar to those defined in the three-dimensional rotor model analyzed in Chapter 4. One of the two blades is modeled assuming the flow is axi-symmetric, requiring periodic boundaries at the domain split, shown in Figure 53. The center of the domain surrounding the center of rotation is defined as an extrapolation boundary, while the outer far field domain surfaces are inflow/outflow boundaries. The blade and ejector shroud surfaces are no-slip viscous wall boundaries. The primary ejector nozzle, shown in Figure 55, is an inflow boundary with the total pressure, total temperature, and Mach number defined for the flow entering the domain.

There are several singular boundaries that are required for this grid topology. The first is located at the interface of the ejector mixing plane and the grid block trailing the rotor blade. The second and third singular boundaries are faces in the grid block protruding in the radial direction from the blade tip and provide the means to model a sharp tipped rotor blade.

6.2.3 Model Convergence

The overall convergence of the rotary wing ejector model is observed by the reduction of the total residual, decay of the global drag to a constant value, and the change in the global drag over varying levels of grid refinement. The model is run for 36,000 iterations, representing 10 full rotations at 0.1 degrees and 10 sub-iterations per time step. The computation time for 64 processors is 381 hours, 12 minutes, and 5 seconds. The total residual as a function of iteration number is presented in Figure 57. The total residual attains a relatively constant value after 8000 iterations and reduces more than 1 and a half orders of magnitude. The mean drag coefficient as a function of iteration number is presented in Figure 58. Each grid coarseness level is run for 12,000 iterations. The coarse grid shows some high frequency oscillations in the mean drag value before the model transitions to the medium grid. This behavior is not present in the 3D rotor validation study and is therefore attributed to the ejector nozzle. The change in the mean drag coefficient for varying grid coarseness levels is presented in Table 14, showing good grid convergence.

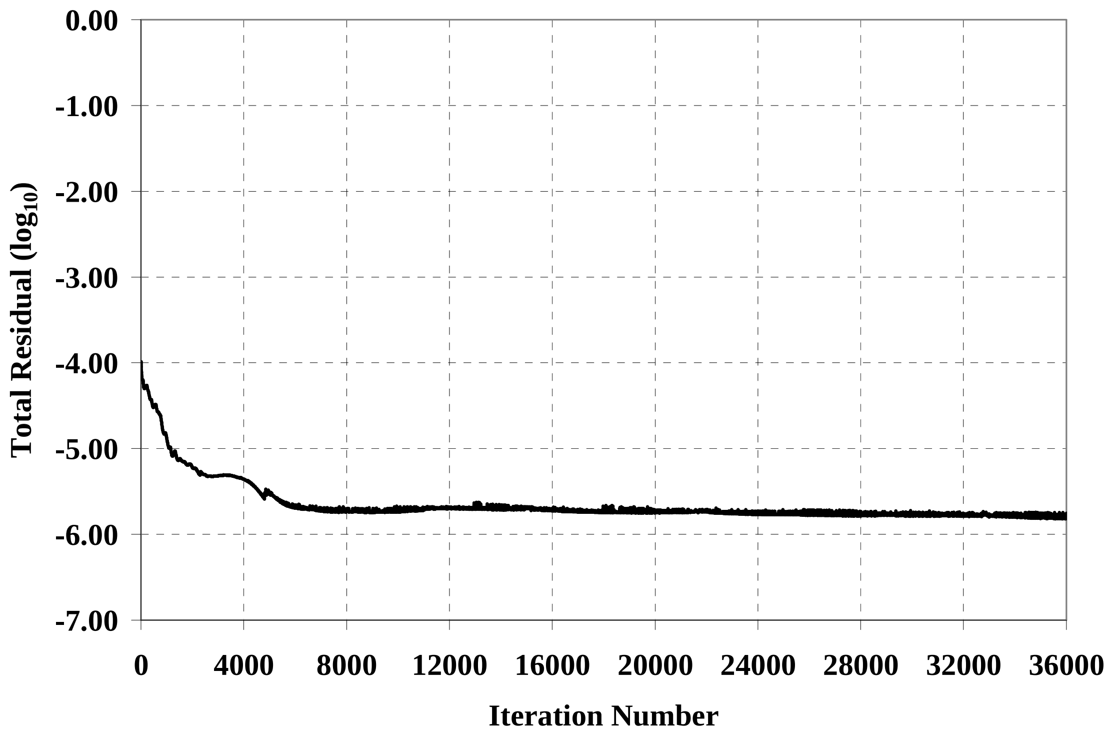

Figure 57: Three-Dimensional CFD Model Total Residual Convergence History

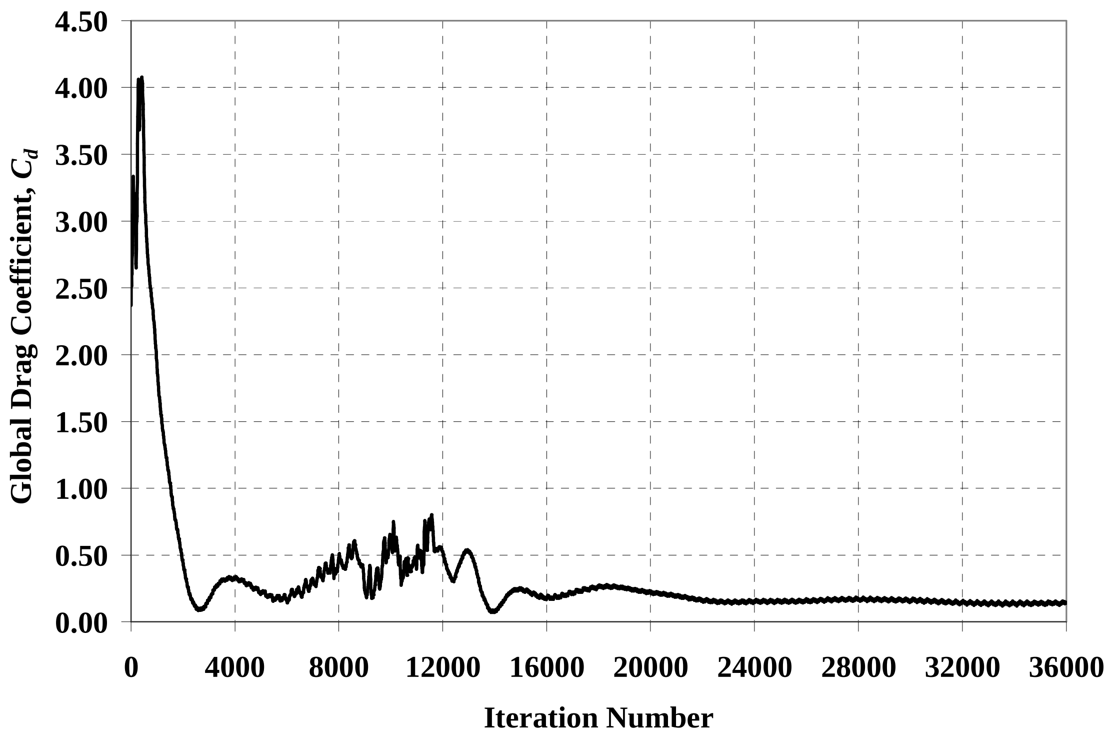

Figure 58: Three-Dimensional CFD Model Mean Drag Convergence History

Table 14: Three-Dimensional CFD Model Mean Drag Grid Convergence

	Number of Grid Points	Mean Drag Coefficient, C_d
Coarse Grid	6,486,371	0.443
Medium Grid	12,972,740	0.164
Fine Grid	25,945,479	0.146
Richardson Extrapolation	-	0.145

The thrust balancing procedure, presented in Figure 52, is applied to the three-dimensional model of the rotary wing ejector. The initial model is executed using the primary nozzle boundary conditions obtained from the rotary wing ejector sizing procedure in Chapter 5. Upon completion of the 3D CFD model, the torque is computed by summing the resultant drag force, multiplied by the radial distance, along the blade. The net thrust required is then the torque divided by the blade radius. The net thrust produced by the ejector nozzle is found by summing the integrated momentum at the secondary inlets and ejector exit, given in the following relation.

$$\textbf{(110)} \quad FN = \int_A \rho\left(\vec{V} \cdot \vec{V}\right) dA \bigg|_{Upper\_Inlet} + \int_A \rho\left(\vec{V} \cdot \vec{V}\right) dA \bigg|_{Lower\_Inlet} + \int_A \rho\left(\vec{V} \cdot \vec{V}\right) dA \bigg|_{Exit}$$

The first two terms in equation (110) represent the ram drag of the ejector, and the third term represents the gross thrust. The net thrust values are compared and the primary nozzle boundary condition is adjusted by increasing or decreasing the fuel flow within the reaction drive thermodynamic model. The results after three iterations, presented in Figure 59, show a slight overshoot. This could be easily remedied by switching to a gradient based scheme as opposed to the fixed point scheme currently implemented. The ejector nozzle ram drag, gross thrust, and net thrust are presented in Table 15, where the secondary inlet ram drag is shown as a negative thrust. It is interesting to note that the ram drag of the upper secondary inlet is over two and a half times greater than that of the lower secondary inlet. The angle of attack over the tip region is positive, which results in a greater air velocity entering the upper secondary inlet compared to the lower secondary inlet. The upper secondary inlet area is slightly smaller than the lower secondary inlet area, as presented in Chapter 5, Table 11. This is done in an attempt to balance the mass flow rate through the upper and lower secondary inlets. The mass flow rates are computed for the 3D rotary wing ejector model by the following equation.

$$\textbf{(111)} \quad \dot{m} = \int_A \rho \vec{V} dA \Big|_{Upper\_Inlet} + \int_A \rho \vec{V} dA \Big|_{Lower\_Inlet} + \int_A \rho \vec{V} dA \Big|_{Exit}$$

The resulting mass flow rates are presented in Table 16. The upper secondary inlet mass flow rate is greater than that of the lower secondary inlet. This certainly contributes to the increased ram drag shown in Table 15. Additionally, both of the secondary inlet mass flow rates are greater than those predicted by the 2D modeling.

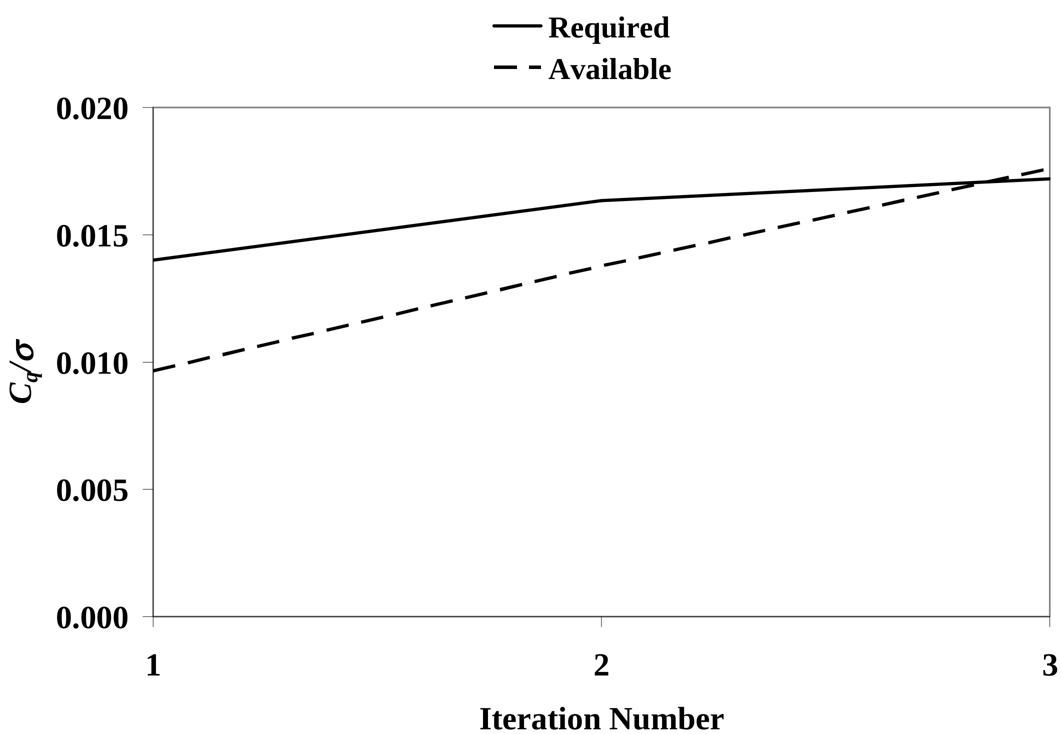

Figure 59: Thrust Balancing Procedure Convergence History

Table 15: Ejector Thrust

	Thrust (lb)
Upper Secondary Inlet	-6.52
Lower Secondary Inlet	-2.42
Ejector Exit	17.48
Net	8.54

Table 16: Ejector Mass Flow Rate

	Mass Flow Rate (lb/s)
Upper Secondary Inlet	0.17
Lower Secondary Inlet	0.12
Primary Nozzle	0.30
Ejector Exit	0.58

6.2.4 Rotary Wing Ejector Modeling Results

The lift coefficient is computed along the radial direction of the blade using equation (104) with the force components computed by CFL3D. The resulting radial load distribution is presented in Figure 60. Immediately, the difference between the clean rotor and rotary wing ejector is apparent at the tip region. There are spikes in C_L at the locations where the blade transitions to the ejector nozzle. The sharp drop in C_L at the start and end of the ejector nozzle section is primarily due to the shape of the ejector nozzle sidewalls, shown in Figure 61. The transition in loading from the ejector nozzle sidewall section to the ejector nozzle section is very abrupt and in the opposite direction of the two-dimensional CFD based model of the rotary wing ejector. This effect appears to primarily be the result of the change in geometry and could be reduced by smoothing the transition from the blade to the ejector. The lift coefficient shows a decaying trend along the radial direction across the ejector nozzle. From the data presented in Figure 60, it is unclear as to why this is the case. The total loading at the ejector sections of the rotor blade are the sum of the blade tip section loading and the loading of the upper and lower ejector shroud. The pressure distributions in the chord-wise direction of these components, at three radial sections within the ejector nozzle, are presented in Figure 62 - Figure 64. The upper shroud (Figure 62) shows an increase in negative pressure, indicating an increase in download, from the inboard section to the outboard section. The lower shroud (Figure 63) has a similar trend; however, the greatest change occurs between nondimensional radial distances 0.9 and 0.935.

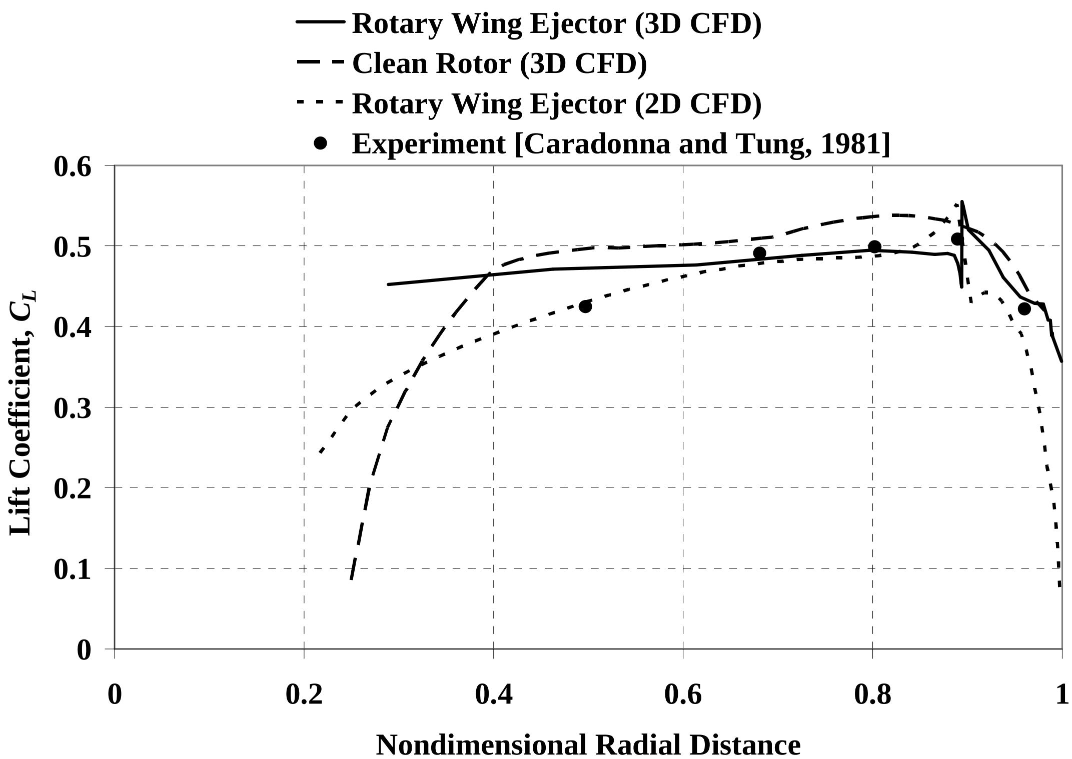

Figure 60: Rotary Wing Ejector Radial Lift Distribution

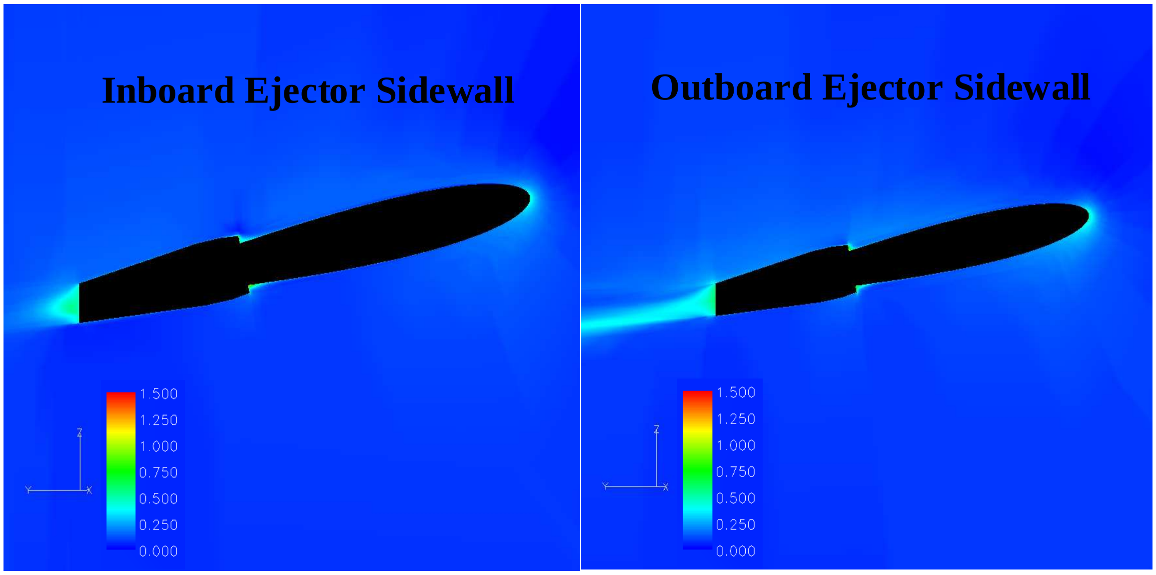

Figure 61: Ejector Sidewall Contours of Constant Mach Number

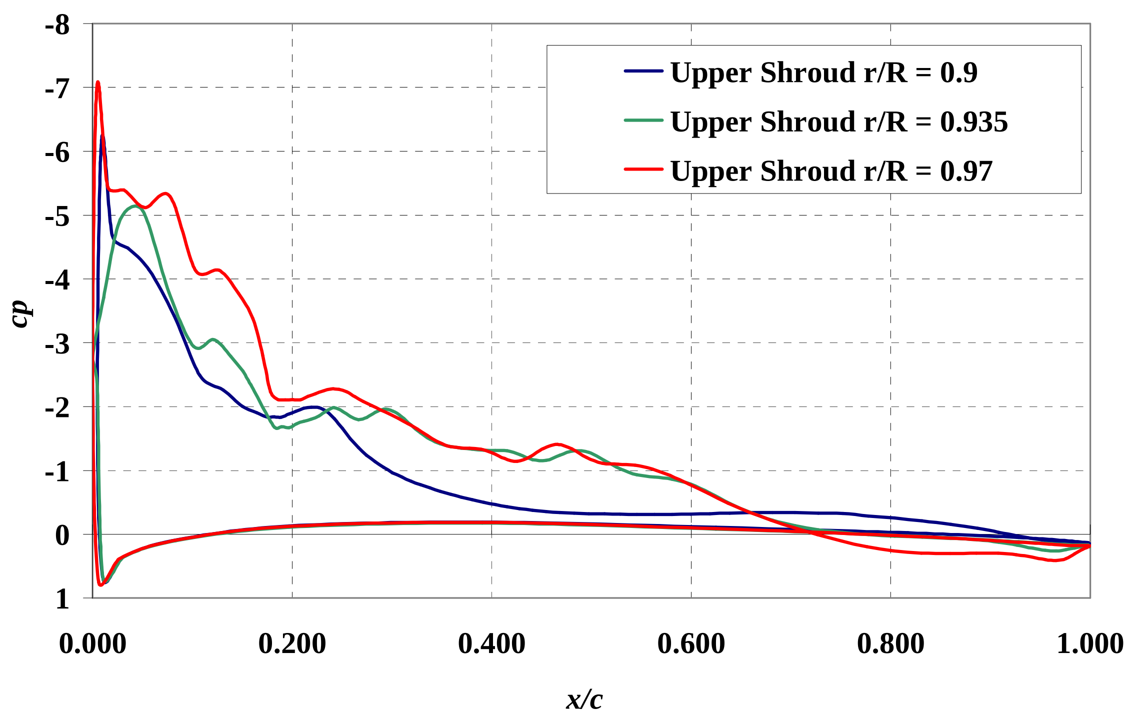

Figure 62: Upper Shroud Chord-wise Pressure Distributions

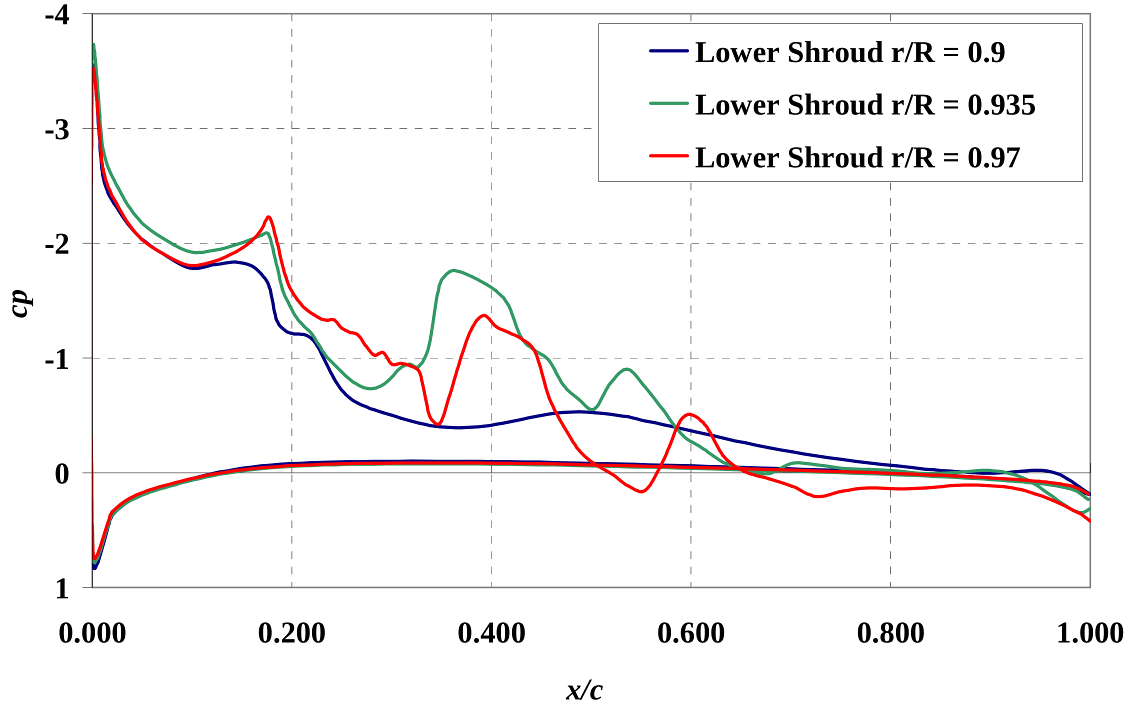

Figure 63: Lower Shroud Chord-wise Pressure Distributions

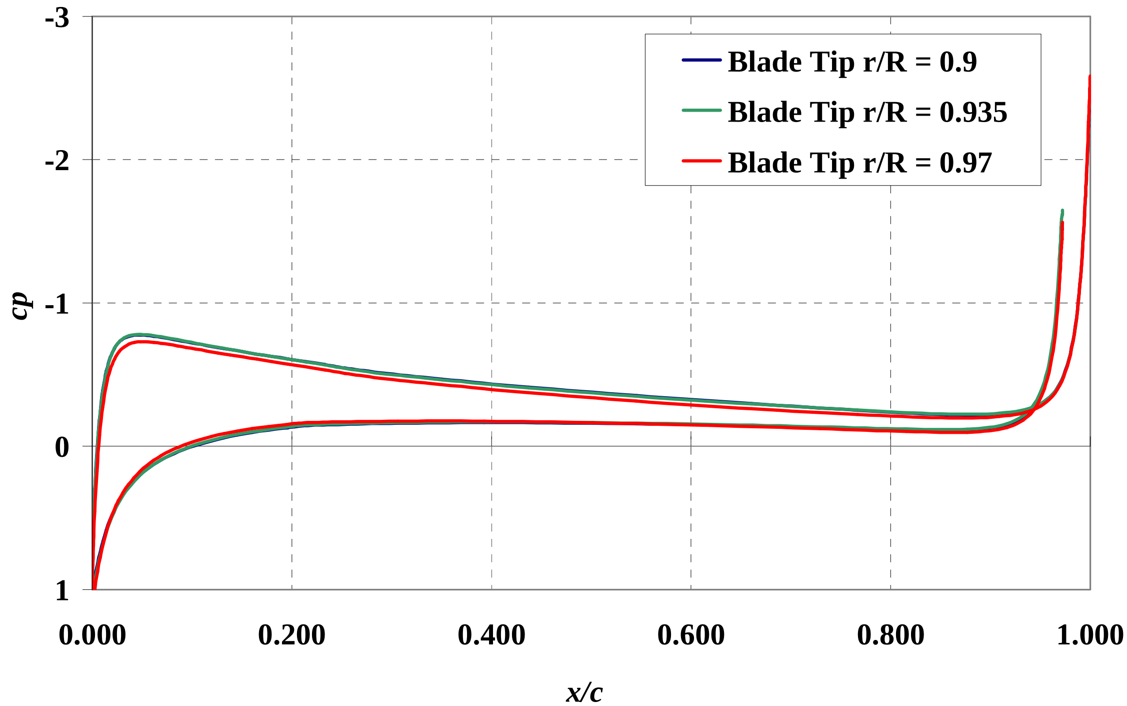

Figure 64: Blade Tip Chord-wise Pressure Distributions

There is also a decrease in the positive pressure, or upload, between nondimensional radial distances 0.935 and 0.97 of the blade tip section (Figure 64). This trend is expected near the blade tip region and is primarily due to tip loss effects. There is almost no difference in the chord-wise pressure distributions of the blade tip section (Figure 64) between nondimensional radial distances 0.9 and 0.935. Therefore, the reduction in the radial lift distribution, shown in Figure 60, between nondimensional radial distances 0.9 and 0.935 is attributed to the upper and lower ejector shrouds. The reduction in the radial lift distribution between nondimensional radial distances 0.935 and 0.97 is a combination of the download from the ejector shrouds and the tip loss effects at the blade tip.

The oscillations in Figure 62 and Figure 63 are due to flow separation along the inside surface of the ejector shrouds. This can be visualized in terms of contours of constant Mach number at each of the three nondimensional radial distances, shown in Figure 65 - Figure 67. Regions of separated flow are indicated by darker blue. It is clear from both the pressure data and the flow visualization that the lower shroud is shedding a vortex at the entrance to the mixing plane. This behavior was not present in the 2D models, most likely because they were run under the steady-state assumption.

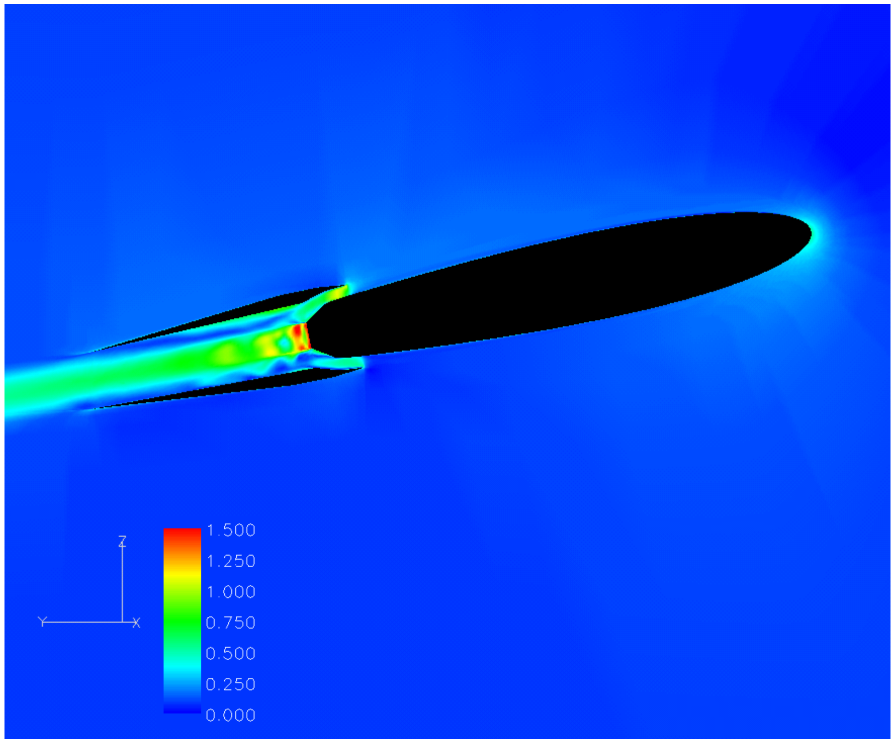

Figure 65: Ejector Section Contours of Constant Mach Number at r/R = 0.9

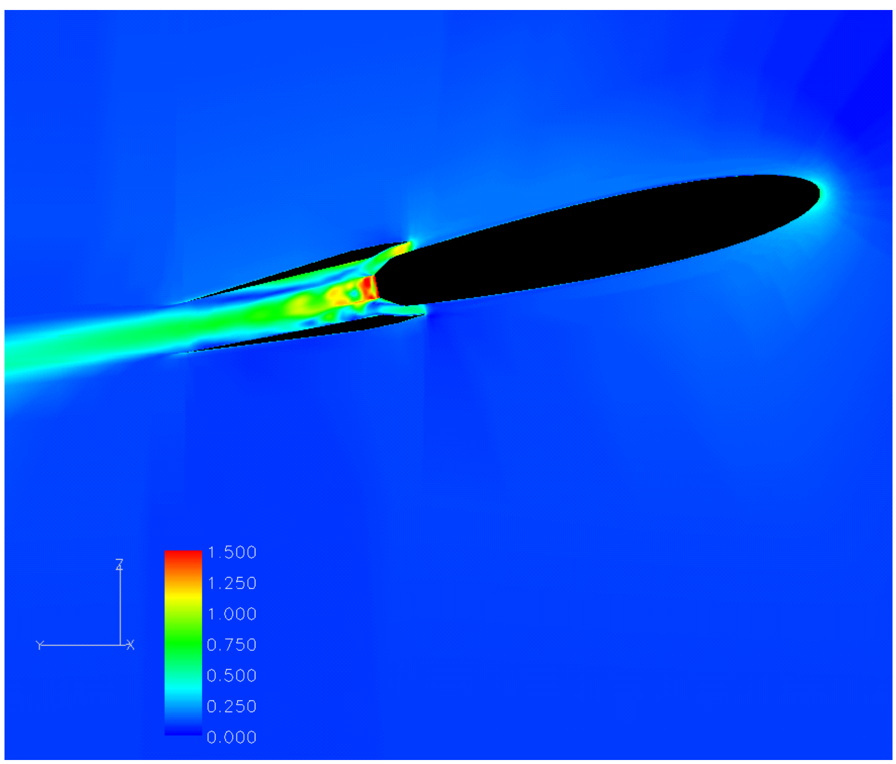

Figure 66: Ejector Section Contours of Constant Mach Number at r/R = 0.935

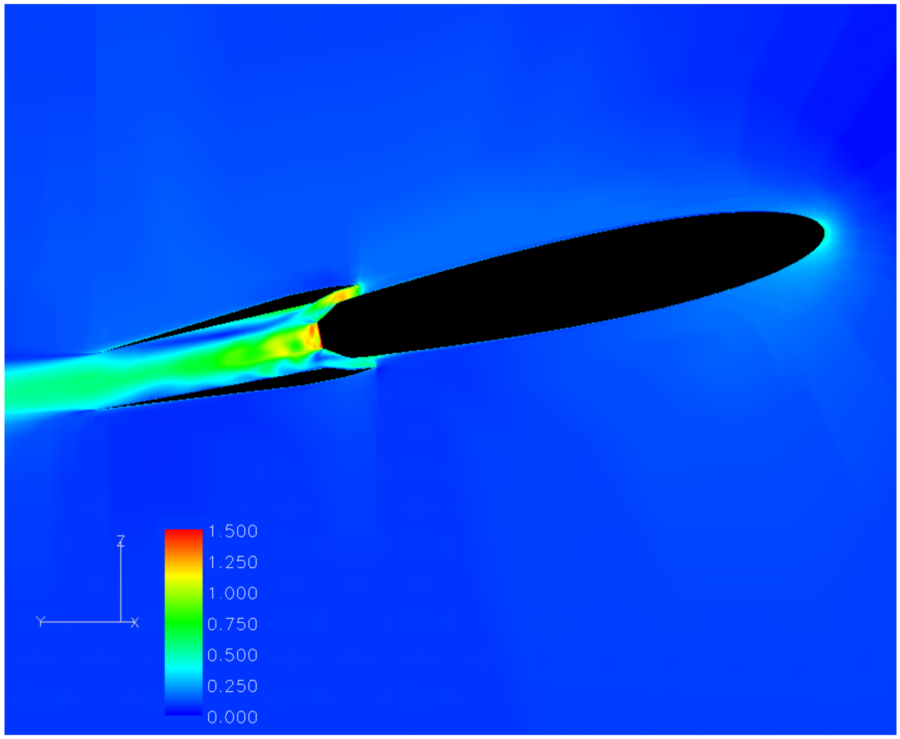

Figure 67: Ejector Section Contours of Constant Mach Number at r/R = 0.97

The overall predicted rotor performance of the rotary wing ejector resulting from the three-dimensional model is presented in Table 17. The rotor thrust and power are compared to the three-dimensional CFD clean rotor model presented in Chapter 4 and the two-dimensional CFD based rotary wing ejector model presented in Chapter 5. The reduction is rotor thrust when comparing the three and two-dimensional models shown in Table 17 is also evident in Figure 60. There is almost a 10% difference in rotor power between the models. There are two primary factors that are attributed to this difference evident from the data presented. The ejector nozzle sidewalls are not included in the two-dimensional CFD based model of the rotary wing ejector. The mass flow rate within the secondary inlets results in an increase in Mach number above the design target. This has the effect of increasing the skin friction over the inlet surfaces, thereby increasing drag.

Table 17: Rotary Wing Ejector Rotor Performance Comparison

	C_T	C_P
1. 3D Clean Rotor CFD	8.71E-03	1.19E-03
2. 2D Rotary Wing Ejector	6.87E-03	1.33E-03
3. 3D Rotary Wing Ejector	7.71E-03	1.46E-03
Difference 1 - 3 (%)	-11.45%	22.63%
Difference 2 - 3 (%)	12.27%	9.72%

6.3 Chapter Summary

A three-dimensional CFD model of a rotary wing ejector is developed to study the aerodynamic effects in a hovering flight condition. The trim procedure implemented in this portion of the research shows the capability to match the required ejector nozzle thrust required to hover to the thrust produced by the ejector nozzle for a given collective pitch angle. The resulting trim solution showed an increased mass flow rate within the secondary inlets when compared to the two-dimensional CFD model. The presence of the ejector nozzle resulted in a decrease in lift along the coincident blade span as the result of an increase in download contribution from the ejector shrouds, in addition to the blade tip loss effects. The overall predicted performance of the three-dimensional model of the rotary wing ejector shows an increase in both rotor thrust and power compared to the two-dimensional CFD based model presented in Chapter 5.

CHAPTER 7

CONCLUSIONS AND RECOMMENDATIONS

The reaction drive rotor is a challenging engineering problem, added to the already complex rotor system. Integrating an ejector nozzle adds to both the design and system complexity. The research develops a coupled, multi-disciplinary, analytical method to address sizing and performance of a rotary wing ejector. Aerodynamic and thermodynamic aspects are analytically investigated and integrated, providing the basis for higher fidelity aerodynamic modeling. A three-dimensional computational fluid dynamic model is incorporated into an ejector nozzle thrust balancing procedure, providing a trim solution for a higher fidelity model of a hovering rotary wing ejector.

7.1 Contributions

The application of an ejector nozzle with a reaction drive rotor further increases system complexity with respect to design and analysis. The rotary wing ejector sizing methodology developed in this research addresses the problem of determining the ejector geometries to produce the required thrust for a given flight condition. A lower fidelity rotary wing ejector model is developed to rapidly generate ejector geometry critical for higher fidelity analysis and design based on vehicle and rotor parameters. In addition to sizing the ejector geometry, the model allows for design tradeoffs to be performed for this rotor configuration by linking model components to standard rotor and ejector design variables.

The rotary wing ejector sizing methodology is extended to capture basic rotor and ejector performance trends. The lower fidelity rotary wing ejector model is reformulated to determine ejector flow parameters based on predetermined ejector geometry. A range of rotor thrust conditions are studied, showing the effects of the ejector nozzle on the rotor power and efficiency. The ejector exit velocity is compared to the primary nozzle velocity, giving good indication of the upper and lower bounds for potential noise reduction over a range of rotor thrusts.

A three-dimensional CFD model of the rotary wing ejector is developed to further study aerodynamic effects. An ejector nozzle thrust trim procedure is introduced to balance the required ejector nozzle thrust to hover to the thrust produced by the ejector nozzle. Differences in the predicted mass flow rates between the two- and three-dimensional models are identified. The effect the ejector shroud has on the coincident blade loading is characterized. Finally, the overall rotor performance of the rotary wing ejector is compared to the reduced computational model and a conventional rotor in hover.

7.2 Lessons Learned

The experience gained from the two-dimensional ejector flow CFD validation model lead to a substantiated selection of the appropriate ejector grid density and turbulence model, both critical to the rotary wing ejector sizing procedure. Experience gained from the three-dimensional CFD model of a hovering rotor aided in the grid generation and model execution of the more complex 3D rotary wing ejector model. This work built up confidence that a CFD model of the rotary wing ejector is possible with the tools available.

It was discovered during the development and testing of the rotary wing ejector nozzle sizing procedure that no feasible solution could be found when the ejector thermodynamic algorithm was activated following the reaction drive thermodynamic algorithm. After careful consideration of the problem, the most logical approach was to increase the energy output from the reaction drive nozzle by increasing the amount of fuel burned compared to what is required when the reaction drive was operating alone.

The two-dimensional CFD modeling performed during the rotary wing ejector sizing and performance procedures required a large number of individual input and output files. During the early execution of these procedures, data transferred to and from the CFD models was handled manually. It became clear that this would become a very involved process, requiring significant effort by the user. Two programs were subsequently developed to transfer the data between the thermodynamic models and CFD models. This allowed for a more automated procedure, and enabled running large numbers of CFD models simultaneously.

Pre- and post-processing programs were developed to reduce the total modeling time associated with the three-dimensional CFD models. The pre-processor was developed to generate the model input files after it was discovered that the CFL3D’s block splitting program had difficulties with the grid topology. The post-processing program extracted surface pressure data from the model field data output file. Additionally, data for both walls and flow-through planes was extracted from control surface output files.

7.3 Improvements

The computational grid generation for both the two and three-dimensional CFD models required a significant amount of time. For the two-dimensional modeling, the time was spent regenerating essentially the same grid over and over with small modifications in geometry. This process would benefit from an input file driven grid generator as opposed to a graphical user interface, allowing full integration of the grid generation and CFD modeling into both the sizing and performance procedures. In addition to reducing the user effort during the execution of the model, both procedures could be included in system optimization.

The solver within the thermodynamic model uses Newton's method for a system of equations to iteratively solve for the unknowns. Newton's method requires reasonable initial guess values for the unknowns to reach the solution. The engineer may not have the experience necessary to input guess values that will result in convergence. This may also become problematic if the rotary wing ejector sizing procedure is wrapped inside a higher level optimizer. At the very minimum, logic should be added to the thermodynamic model such that geometric and flow parameters stay within acceptable ranges.

7.4 Future Work

The analytical methods presented in this document provide a foundation for future study of an ejector nozzle integrated with a reaction drive rotor. These methods are largely scale independent and therefore can be applied to a full sized rotorcraft implementing this type of rotor configuration. Furthermore, they can be readily coupled to an aeroacoustic model of the ejector nozzle to predict the jet noise for the given flight condition. While the hovering flight condition is the primary focus of this research, forward flight may be studied by simply replacing the rotor aerodynamic model with a model that has forward flight capabilities. This enhancement would enable the prediction of the effective perceived noise level (EPNL) during the take off or landing of this type of rotorcraft.

The forced mixing of the high speed flow exiting the tip jet nozzle and the lower speed secondary flow by the lobed mixer nozzle within in the ejector is addressed empirically for the rotary wing ejector sizing and performance methods. The two and three-dimensional CFD models presented in this document do not address the forced mixing of the two flows. A forced mixing nozzle would typically be incorporated on most ejector nozzle configurations as they have shown enhanced mixing resulting in a more compact design. A study of the aerodynamic and acoustic effects of adding a forced mixing nozzle to the rotary wing ejector would complement this research.

There is still gap between the capabilities of the current comprehensive codes (RCAS/CAMRAD) and what is required for a reaction drive rotor configuration. The rotor aerodynamics is based on empirical or CFD generated lift, drag, and moment coefficients. The development of a coupling scheme between the comprehensive rotorcraft code and the blade tip aerodynamics and thermodynamics opens the door for a more complete investigation of the flight envelope.

The control volume showed poor correlation with the two-dimensional and three-dimensional CFD models with respect to the control volume boundary flow conditions. This is due, in part, to the dimensional reduction of the flow properties during the ejector sizing procedure through mass averaging. Mass averaging provides a rapid conversion of the CFD flow profile data into one-dimensional values. The mass averaged pressure, temperature, and velocity are then used to compute continuity, momentum, and energy in the one-dimensional control volume model. However, these values do not match the integrated mass, momentum, and total energy from the two- and three-dimensional CFD models. To address this issue, an iterative procedure could be applied to determine the pressure, temperature, and velocity that satisfy the integrated continuity, momentum, and energy from the CFD results. These values then represent the one-dimensional flow parameters that are then used in the control volume analysis. The primary disadvantage to this procedure is that the entropy is not balanced between the CFD and one-dimensional representations of the flow properties.

Finally, the ejector presented in this research is simplified in terms of its geometry and placement. Optimization of the ejector geometric configuration, focused on minimizing the overall rotor power required, is the next logical extension of the methodology presented in this research. Secondary inlets, ejector shroud, and ejector nozzle vector angle represent the primary elements of the rotary wing ejector system that are available for optimization. The placement of the secondary inlets with respect to the rotor blade cross section should be selected such that the operation of the ejector is relatively insensitive to the local angle of the free stream flow. The shape of the ejector shroud should minimize drag and maximize ejector performance, which may be conflicting requirements. The angle at which the nozzle flow is exhausted should be considered to determine the best lift-to-drag ratio of the ejector nozzle section and thereby, the lowest rotor power requirement.

REFERENCES

Addy, A.L., Dutton, J.C., Mikkelson, C. D., Supersonic Ejector-Diffuser Theory and Experiments. Report UILU-ENG-82-4001, Department of Mechanical Engineering, University of Illinois at Urbana-Champaign, Urbana, Illinois, 1981.

Alperin, M., Wu, J., Recent Development of a Jet-Diffuser Ejector. Journal of Aircraft, Volume 18, Number 12, Pages 1011-1018, December 1981.

Alperin, M., Wu, J., Thrust Augmenting Ejectors, Part I. AIAA Journal, Volume 21, Number 10, Pages 1428-1436, October 1983a.

Alperin, M., Wu, J., Thrust Augmenting Ejectors, Part II. AIAA Journal, Volume 21, Number 12, Pages 1698-1706, December 1983b.

Anderson, J.D., Jr, *Computational Fluid Dynamics: The Basics with Applications*, McGraw-Hill, Inc, 1995.

Arbel, A., Shklyar, A. Hershgal, D. Barak, M. Sokolov, M., Ejector Irreversibility Characteristics. Journal of Fluids Engineering, January 2003.

Bachmann, B.A., Power Available Calculations Procedure and Operational Aspects of a Tip jet-Propelled Rotor System. 26th Annual National Forum of the American Helicopter Society, Washington D.C., June 1970.

Barber, T.J., Anderson, O.L., An Analytical Study of a Supersonic Mixer – Ejector Exhaust System. 29th Aerospace Sciences Meeting, AIAA Paper 91-0126, January 1991.

Barber, T.J., Anderson, O.L., Computational Study of a Supersonic Mixer-Ejector Exhaust System. Journal of Propulsion and Power, Volume 8, Number 5, Pages 927-934, October 1992.

Bevilaqua, P.M., Lifting Surface Theory for Thrust Augmenting Ejectors. AIAA Journal 0001-1452, Volume 16, Number 5, Pages 475-481, May 1978.

Bevilaqua, P.M., Advances in Ejector Thrust Augmentation. AIAA/AHS/ASEE Aircraft Design Systems and operations Meeting, AIAA Paper 84-2425, November 1984.

Bradshaw, P., Cebeci, T., and Whitelaw, J.H., *Engineering calculations methods for turbulent flow*, Academic Press, London, 1981.

Bogdanoff, D.W., Compressibility Effects in Turbulent Shear Layers. AIAA Journal, Volume 21, Number 6, Pages 926-927, November 1982.

Caradonna, F.X., Tung, C., Experimental and Analytical Studies of a Model Helicopter Rotor in Hover. NASA TM 81232, September 1981.

Catalano, G.D., Wright, H.E., Stephens, D.G., Nagaraja, K.S., Walterick, R.E., Turbulence Measurements in an Ejector Wing Flowfield. AIAA Journal, Volume 19, Number 7, Pages 603-605, July 1982.

Cengel, Y.A., Boles, M.A., *Thermodynamics: an Engineering Approach*, McGraw-Hill Companies, Inc., New York, 1998.

Clark, R.L., Ejector Blown Lift/Cruise Flap Wind Tunnel Investigation. Air Force Flight Dynamics Laboratory, Wright-Patterson Air Force Base, Ohio, AD-777-181, November 1973.

Clark, L., Application of Compound Flow Analysis to Supersonic Ejector-Mixer Performance Prediction. 33rd Aerospace Sciences Meeting and Exhibit, AIAA Paper 95-0645, January 1995.

Charyulu, B. V.N., Kurian, J., Venugopalan, P., Sriramulu, V., Experimental Study on Mixing Enhancement in Two Dimensional Supersonic Flow, Experiments in Fluids, Volume 24, Number 4, Pages 340-346, April 1998.

Chow, W.L., Addy, A.L., Interaction between Primary and Secondary Streams of Supersonic Ejector Systems and Their Performance Characteristics. AIAA Journal, Volume 2, Number 4 Pages 686-695, April 1964.

Crossley, W.A., Rutherford, J.W., Sizing Methodology for Reaction-Driven, Stopped-Rotor Vertical Takeoff and Landing Concepts. Journal of Aircraft, Vol. 32, No. 6, November – December 1995.

Dadone, L.U., U.S. Helicopter Design Datcom Volume I – Airfoils. Report No. D210-11097-1, Boeing Vertol Company, Philadelphia, Pa, May 1976.

DalBello, T., Steffen Jr., C.J., Parametric Study of a Mixer/Ejector Nozzle with Mixing Enhancement Devices. 40th AIAA Aerospace Sciences Meeting and Exhibit, AIAA Paper 2002-0667, January 2002.

DeBonis, J.R., Full Navier-Stokes Analysis of a Two-Dimensional Mixer/Ejector Nozzle for Noise Suppression, AIAA/SAE/ASEE 28th Joint Propulsion Conference and Exhibit, AIAA Paper 92-3570, July 1992.

De Chant, L.J., Combined Numerical/Analytical Perturbation Solutions of the Navier-Stokes Equations for Aerodynamic Ejector/Mixer Nozzle Flows. NASA CR-1998-207406, April 1998.

DeJoode, A.D., Patankar, S.V., Prediction of Three-Dimensional Turbulent Mixing in an Ejector. AIAA Journal, Volume 16, Number 2, Pages 145-150, February 1978.

Desevaux, P., Lanzetta, F., Computational Fluid Dynamic Modeling of Pseudo shock Inside a Zero-Secondary Flow Ejector. AIAA Journal, Volume 42, Number 7, Pages 1480-1483, July 2004.

Dippold, III, V.F., Numerical Assessment of the Performance of Jet-Wing Distributed Propulsion on Blended-Wing-Body Aircraft. Masters Thesis, Virginia Polytechnic Institute and State University, July, 2003.

Dolling, D.S., Fournier, E., Shau, Y.R., Effects of Vortex Generators on the Growth of a Compressible Shear Layer. Journal of Propulsion and Power, Volume 8, Number 5, Pages 1049-1056, October 1992.

Dong, T.Z., Mankbadi, R.R., Simulation of Unsteady Flow in Nozzle-Ejector Mixer. Journal of Propulsion and Power, Volume 15, Number 4, Pages 539-543, August 1999.

Dutton, J.C., Mikkelsen, C.D., Addy, A.L., A Theoretical and Experimental Investigation of the Constant Area, Supersonic-Supersonic Ejector. AIAA Journal, Volume 20, Number 10, Pages 1392-1400, October 1982.

Dutton, J.C., Carroll, B.F., Optimal Supersonic Ejector Designs. Journal of Fluids Engineering, Volume 108, Pages 414-420, December 1986.

Elliot, G.S., Samimy, M., Compressibility Effects in Free Shear Layers. Physics of Fluids A: Fluid Dynamics, Volume 2, Issue 7, Pages 1231-1246, July 1990.

Elliott, J.K., Manning, T.A., Qiu, Y.J., Computational and Experimental Studies of Flow in Multi-Lobed Forced Mixers. AIAA/SAE/ASME/ASEE 28th Joint Propulsion Conference and Exhibit, AIAA Paper 92-3568, July 1992.

Emanuel, G., Optimum Performance for a Single-Stage Gaseous Ejector. AIAA Journal, Volume 14, Number 9, Pages 1292-1296, September 1976.

Evans, W.T., McCloud, J.L., Analytical Investigation of a Helicopter Rotor Driven and Controlled by Jet Flaps. NASA TN-D-3028, NASA Ames Research Center, Moffett Field, CA, September 1965.

Fabri, J., Paulon, J., Theory and Experiments on Supersonic Air-to-Air Ejectors. NACA Technical Memorandum 1410, Washington D. C., September 1958.

Fernando, E.M., Menon, S., Mixing Enhancement in Compressible Mixing Layers: An Experimental Study, AIAA Journal, Volume 31, Number 2, February 1993.

Fiorini, V., Study of a Jet Propelled Helicopter Rotor with Jet Flaps. Journal of the American Helicopter Society, Vol. 6, No. 1, January 1961.

Fox, R.W., McDonald, A.T., Introduction to Fluid Mechanics Fifth Edition. John Wiley & Sons, Inc., New York, 1998.

Gessow, A., Meyers, G.C., Aerodynamics of the Helicopter, Fredrick Ungar Publishing, 1952.

Gilbert, G.B., Hill, P., Analysis and testing of Two-Dimensional Slot Nozzle Ejectors with Variable Area Mixing Sections. NASA CR-2251, May 1973.

Gutmark, E., Schadow, K.C., Wilson, K.J., Effect of Convective Mach Number on Mixing of Coaxial Circular and Rectangular Jets. Physics of Fluids A: Fluid Dynamics, Volume 3 Issue 1, Pages 29-36, January 1991.

Goebel, S.G., Dutton, J.C., Experimental Study of Compressible Turbulent Mixing Layers. AIAA Journal, Volume 29, Number 4, Pages 538-546, April 1991.

Hall, D.W., A Compact Methodology for Estimating Duct Losses in Subsonic Inlets, Contract Report Prepared for NASA Ames Research Center, Moffett Field, CA, January 1995.

Han, S., Peddieson Jr., J., One-Dimensional Numerical Study of Compressible Flow Ejector. AIAA Journal, Volume 40, Number 7, Pages 1469-1472, April 2002.

Harned, M.S., Amer, K.B., Sullivan, R.J., Hot Cycle Rotor/Wing for High Speed City Transportation. AIAA 4th Annual Meeting and Technical Display, AIAA Paper 67-770, October 1967.

Hedges, K.R., Hill, P.G., Compressible Flow Ejectors. Part I – Development of a Finite-Difference Flow Model. Transactions of the ASME, Journal of Fluids Engineering, Pages 272-281, September 1974.

Hedges, K.R., Hill, P.G., Compressible Flow Ejectors. Part II-Flow Field Measurements and Analysis. Transactions of the ASME, Journal of Fluids Engineering, Pages 282-288, September 1974.

Henry, J.R., One Dimensional, Compressible, Viscous Flow Relations Applicable to Flow in a Ducted Helicopter Blade. NACA TN 3089, October 1953.

Hickman, K.E., Gilbert, G.B., Carey, J.H., Analytical and Experimental Investigation of High Entrainment Jet Pumps. NASA CR-1602, July 1970.

Hickman, K.E., Hill, P.G., Gilbert, G.B., Analysis and Testing of High Entrainment Single-Nozzle Jet Pumps with Variable-Area Mixing Tubes. NASA CR-2067, June 1972.

Hunt, D.L., May, N.E., Practical use of Transport Turbulence Models in Aerospace, CFD Implementation and Applications. AIAA Paper 99-3137, 1999.

Ives, D.C., Melnik, R.E., Numerical Calculation of the Compressible Flow over an Airfoil with a Jet Flap. 7th AIAA Fluid and Plasma Dynamics Conference, AIAA Paper 74-542, June 1974.

Johnson, W., Helicopter Theory, Dover Publications Inc., New York, New York, 1994.

Keenan, J.H., Neumann, E.P., Lustwerk, F., An Investigation of Ejector Design by Analysis and Experiment. Journal of Applied Mechanics, Volume 17, Pages 299-309, September 1950.

Krejsa, E.A., Cooper, B.A., Hall, D.G., Khanaran, A., "Noise Measurements from an Ejector Suppressor Nozzle in the NASA Lewis 9- by 15-Foot Low Speed Wind Tunnel," AIAA 13th Aeroacoustics Conference," AIAA Paper 90-3983, October 1990.

Kremar, J., Peddieson, J., Ham, S., A control Volume Model of Multiple Gas/Multiple Ejector Systems. 39th AIAA/ASME/SAE/ASEE Joint Propulsion Conference and Exhibit, AIAA Paper 2003-5229, July 2003.

Krist, S.L., Biedron, R.T., Rumsey, C.L., CFL3D User's Manual, National Aeronautics and Space Administration, TM-1998-208444, Washington, DC, 1998.

Kuhne, C.M., Uenishi, K., Leon, R.M., Abdol-Hamid, K.S., CFD Based 3D Aero Analysis System for High-Speed Mixer-Ejector Exhaust Nozzles. 30th AIAA/ASME/SAE/ASEE Joint Propulsion Conference, AIAA Paper 94-2941, June 1994.

Landgrebe, A.J., An Analytical and Experimental Investigation of Helicopter Rotor Performance and Wake Geometry Characteristics. USAAMRDL TR 71-24, 1971.

Landgrebe, A.J., The Wake Geometry of a Hovering Rotor and Its Influence on Rotor Performance. Journal of the American Helicopter Society, 17 (4), pp. 2-15, 1972.

Leishman, G.J., Principles of Helicopter Aerodynamics. Cambridge University Press, New York, 2000.

Lighthill, M.J., On Sound Generated Aerodynamically: I. General Theory. Proc. Royal Soc. London, ser. A, Volume 211, Number 1107, Pages 564-587, March 1952.

Loka, M., Robichaud, M., Bartolomeo, W.D., Loe, D., Sowers, D., Aerodynamic Optimization of the Exhaust-Ejector on the Tiltrotor Using Navier-Stokes Analysis. 38th Aerospace Sciences Meeting and Exhibit, AIAA Paper 2000-0986, January 2000.

Lord, W.K., Jones, C.W., Stern, A.M., Mixer Ejector Nozzle for Jet Noise Suppression. AIAA/SAE/ASME/ASEE 26th Joint Propulsion Conference, AIAA Paper 90-1909, July 1990.

Luffy, R.J., Hamed, A., A Study on the Impact of Shroud Geometry on Ejector Pumping Performance. AIAA/SAE/ASME/ASEE 28th Joint Propulsion Conference, AIAA Paper 92-3260, July 1992.

Maroti, L.A., Hill, P.G., Armstrong, R.L., Haines, D.M., Analysis and Testing of Two-Dimensional Vented Coanda Ejectors with Asymmetric Variable Area Mixing Sections. NASA CR-2721, October 1976.

Masud, J., Javed, A., Modification of Standard k-Epsilon Turbulence Model for Analysis and Design Refinement of Fuel Ejector Pump. 45th AIAA Aerospace Sciences Meeting and Exhibit, AIAA Paper 2007-530, January 2007.

McFarlan, J.D., McMurry, C.B., Scaggs, W.F., Computational Investigation of Two-Dimensional Ejector Nozzle Flow Fields. AIAA/SAE/ASME/ASEE 26th Joint Propulsion Conference, AIAA Paper 90-2148, July 1990.

Middleton, D., Theoretical and Experimental Investigations into the Acoustic Output from Ejector Flows. Journal of Sound and Vibration, Volume 11, Number 4, Pages 447-473, 1970.

Moody, L.F., Friction Factors for Pipe Flow, Transactions of the ASME, 66, 8, pp. 671-684, November 1944.

Naumowicz, T., Smith, B.E., Hover Performance Validation of an Ejector Configured STOVL Fighter Aircraft. AIAA Aircraft Design Systems Meeting, AIAA Paper 92-4255, August 1992.

Nichols, J.B., The Pressure-Jet Helicopter Propulsion System. Hughes Tool Company, Aircraft Division, Repot 70-81, 1970.

Nordstrom, K.E., Marsh, A.H., Sargisson, D.F., Conceptual Design of Advance Acoustic-Composite Nacelles. NASA CR-132703, July 1975.

Pai, S.I., On Supersonic Flow of a Two-Dimensional Jet in Uniform Stream. Journal of the Aeronautical Sciences, January 1952.

Paterson, R.W., Turbofan Mixer Nozzle Flow Field-A Benchmark Experimental Study. Journal of Engineering for Gas Turbines and Power, Volume 106, Pages 692-698, July 1984.

Papamoschou, D.A., Roshko, A., The Compressible Turbulent Shear Layer: An Experimental Study. Journal of Fluid Mechanics, Volume 197, Pages 453-477, 1988.

Papamoschou, D., Analysis of Partially Mixed Supersonic Ejector. Journal of Propulsion and Power, Volume 12, Number 4, Pages 736-741, August 1996.

Poppen, W.A., Smith, B.E. Lye, J.D., Propulsion-Induced Aerodynamics of an Ejector-Configured STOVL Fighter Aircraft. AIAA Paper 91-0765, January 1991.

Porter, J.L., Squyers, R.A., A Summary/Overview of Ejector Augmenter Theory and Performance. ATC Report Number R-91100/9CR-47A, Vought Corporation Advanced Technology Center, Dallas, Texas, 1979.

Presz, W. Jr., Gousy, R., Forced Mixer Lobes in Ejector Designs. AIAA/SAE/ASME/ASEE 22nd Joint Propulsion Conference, AIAA Paper 86-1614, Huntsville, AL, June 1986.

Presz, W. Jr., Blinn, R.F., Short Efficient Ejector Systems. AIAA/SAE/ASME/ASEE 23rd Joint Propulsion Conference, AIAA Paper 87-1837, July 1987.

Presz, W. Jr., Reynolds, G., Hunter, C., Thrust Augmentation with Mixer/Ejector Systems. 40th AIAA Aerospace Sciences Meeting and Exhibit, AIAA Paper 2002-0230, January 2002.

Presz, Jr., W.M., Werle, M., Multi-Stage Mixer/Ejector Systems. AIAA/SAE/ASME/ASEE 38th Joint Propulsion Conference, AIAA Paper 2002-4064, July 2002.

Prouty, R.W., Helicopter Performance, Stability, and Control. Kreiger Publishing Company, Inc., Florida, 1986.

Quinn, B., Compact Ejector Thrust Augmentation. Journal of Aircraft, Volume 10, Number 8, August 1973.

Richardson, L.F., The approximate arithmetical solution by finite differences of physical problems including differential equations, with an application to the stresses in a masonry dam. Philosophical Transactions of the Royal Society of London, Series A 210: 307–357, 1910.

Roache, P.J., Verification and Validation in Computational Science and Engineering, Hermosa Publishers, Albuquerque, New Mexico, 1998.

Skebe, S.A., McCormick, D.C., Presz Jr., W.M., Parameter Effects on Mixer-Ejector Pumping Performance. AIAA 26th Aerospace Sciences Meeting, AIAA Paper 88-0188, January 1988.

Smith, B.E., Garland, D.B., Poppen, W.A., Aerodynamic Performance of a Full-Scale Lifting Ejector System in a STOVL Fighter Aircraft. AIAA/SAE/ASME/ASEE 28th Joint Propulsion Conference, AIAA Paper 92-3094, July 1992.

Smith, M.J.T., Lowrie, B.W., Brooks, J.R., Bushell, K.W., "Future Supersonic Transport Noise – Lessons from the Past," AIAA/SAE/ASME/ASEE 24th Joint Propulsion Conference, AIAA Paper 88-2989, July 1988.

Spence, D.A., The Lift Coefficient of a Thin, Jet-Flapped Wing. Proceedings of the Royal Society of London, Series A, Mathematical and Physical Sciences, Volume 238, Issue 112, December, 1956, pp. 46-68.

Stepan, A., The Pressure Jet Helicopter. Journal of the Royal Aeronautical Society, Volume 62, February 1958.

Stepniewski, W.Z. and Keys, C.N., *Rotary-Wing Aerodynamics*, Dover Publications, Inc., New York, 1984.

Stone, J.R., Clark, B.J., Krejsa, E.A., "Multiple-Source Semi-Empirical Model for 2D Mixer Ejector Noise Prediction," 9th AIAA/CEAS Aeroacoustics Conference and Exhibit, AIAA Paper 2003-3168, May 2003.

Stone, J.R., Krejsa, E.A., Halliwell, I., Clark, B.J., "Noise Suppression Nozzles for a Supersonic Business Jet," 36th AIAA/ASME/SAE/ASEE Joint Propulsion Conference, AIAA Paper 2000-3194, July 2000.

Sun, D.W., Eames, I.W., Recent Developments in the Design Theories and Applications of Ejectors – A Review. Journal of the Institute of Energy, Volume 68, Pages 65-79, June 1995.

Tillman, T.G., Patrick, W.P., Paterson, R.W., Enhanced Mixing of Supersonic Jets. AIAA/SAE/ASME/ASEE 24th Joint Propulsion Conference, AIAA Paper 88-3002, July 1988.

Tai, Jimmy C.M., A Multidisciplinary Design Approach to Size Stopped Rotor/wing Configurations Using Reaction Drive and Circulation Control. Ph.D. Thesis, Georgia Institute of Technology, Atlanta, GA, August 1998.

Tannehill, J. C., Anderson, D.A., Pletcher, R.H., *Computational fluid mechanics and heat transfer*, 2nd edition, Taylor & Francis, Philadelphia, 1997.

Thayer, E.B., Gamble, E.J., Guthrie, A.R., Kehret, D.F., Barber, T.J., Hendricks, G.J., Nagaraja, K.S., Minardi, J.E., Generation 1.5 High Speed Civil Transport (HSCT) Exhaust Nozzle Program. NASA CR 2004-213131, November 2004.

Tung, C., Pucci, S.L., Caradonna,F.X., Morse, H.A., The Structure of Trailing Vortices Generated by Model Rotor Blades. NASA TM 81316, August 1981.

von Karman, T., Mechanische Aehnlichkeit und Turbulenz. Nachrichten von der Gesellschaft der Wissenschaften zu Gottingen, 1930 (English Translation, NACA TM 611).

Vinokur, M., Conservation Equations of Gasdynamics in Curvilinear Coordinate Systems, Journal of Computational Physics, Vol. 14, 1974, pp. 105-125

White, R.P., Jr., An Investigation of the Vibratory and Acoustic Benefits Obtainable by the Elimination of the Blade Tip Vortex. Journal of the American Helicopter Society, Vol. 18, No. 4, October 1973, pp. 35-44.

Wilcox, D.C., Turbulence Modeling for CFD. DCW Industries, Inc., La Canada, CA, 1994.

Woolard, H.W., Thin-Airfoil Theory of an Ejector-Flapped Wing Section. Journal of Aircraft, Volume 12, Number 1, Pages 26-33, January 1975.

Yang, T., Ntone, F., Jiang, T., Pitts, D.R., An investigation of High Performance, Short Thrust Augmenting Ejectors. Journal of Fluids Engineering, Volume 107, Pages 23-30, March 1985.

Yoder, D.A., Georgiadis, N.J., Wolter, J.D., Quadrant CFD Analysis of a Mixer-Ejector Nozzle for HSCT Applications. NASA TM-2005-213602, April 2005.